Mechanistic Understanding of CO_2 Corrosion Inhibition at Elevated Temperatures

A dissertation presented to

the faculty of

the Russ College of Engineering and Technology of Ohio University

In partial fulfillment

of the requirements for the degree

Doctor of Philosophy

Yuan Ding

May 2019

This dissertation titled

Mechanistic Understanding of CO_2 Corrosion Inhibition at Elevated Temperatures

by

YUAN DING

has been approved for

the Department of Chemical and Biomolecular Engineering

and the Russ College of Engineering and Technology by

Marc Singer

Associate Professor of Chemical and Biomolecular Engineering

Dennis Irwin

Dean, Russ College of Engineering and Technology

ABSTRACT

DING, YUAN, Ph.D., May 2019, Chemical Engineering

Mechanistic Understanding of CO_2 Corrosion Inhibition at Elevated Temperatures

Director of Dissertation: Marc Singer

The mechanisms of corrosion inhibition of mild steel in high temperature and high pressure (HTHP) environments have been historically poorly understood. Due to its limited understanding, effective corrosion inhibition in HTHP wells is still very challenging. The purpose of this dissertation is to investigate the inhibition mechanisms of mild steel in the presence of two commonly used inhibitors (an imidazoline-type and a quaternary ammonium type (quat-type) inhibitor) at elevated temperatures. This comprehensive and systematic study provides insights on the selection of successful inhibition strategies at elevated temperatures.

A series of experiments were first performed in a standard 2L glass cell at low to medium temperature (25°C, 50°C and 80°C) to characterize adsorption kinetics over this temperature range, using the two selected inhibitors. These experiments included general corrosion inhibition tests using linear polarization resistance (LPR) measurements and direct determination of adsorption behavior using a quartz crystal microbalance (QCM). Both test methods yielded similar trends for the two inhibitors tested. This suggested that the loss of inhibition efficiency as temperature increased was a result of desorption being favored at higher temperatures. Novel high temperature corrosion inhibition tests were performed in a 4L autoclave specially designed to enable the injection of inhibitor under pressure, at elevated temperatures of 120°C and 150°C. In addition, the experimental

setup and procedure were incrementally improved to minimize the formation of corrosion products and help identify the true effect of the inhibitors. For the imidazoline-type inhibitor, the inhibition efficiency continued to decrease with increasing temperature up to 120°C and was completely masked by the rapid formation of Fe_3O_4 at 150°C. The presence of Fe_3O_4 played a significant role on the corrosion inhibition at this temperature. The quat-type inhibitor completely lost its inhibition ability at temperatures above 80°C. The formation of corrosion product controlled the corrosion rates at 120°C and 150°C, and the presence of inhibitor had little effect. Both inhibitors showed some degree of degradation at high temperature, although this could not explain, by itself, the observed decrease in performance.

The results of this research highlighted the importance of considering the formation of corrosion products when developing inhibition strategy at elevated temperatures. The work also enabled the development of appropriate experimental setups and procedures to evaluate accurately inhibitor performances at high temperatures. This brought in a significant improvement in the understanding of corrosion inhibition at elevated temperatures, elucidating some aspects of inhibition performance that had been overlooked, and allowing better corrosion management strategies for high temperature applications.

DEDICATION

To

My parents, Guian Ding, Xinqun Bai

My love, Yongjun Zhang

And all other family members

ACKNOWLEDGMENTS

I would like to express my sincere appreciation to my Ph.D. advisor, Dr. Marc Singer, for his support and guidance for this project. You supported me greatly and were always willing to provide help, no matter in academic research or personal life. These valuable experiences will always be in the bottom of my heart and guide me into a better future. I want to thank you for your excellent cooperation.

I would like to take the opportunity to thank Dr. Bruce Brown, the project leader of CC-JIP, for his excellent management and advice for my research. He was always willing to provide necessary aid, from funding approval to equipment maintenance. I also thank Dr. Srdjan Nesic for his insights and profound knowledge, which enabled me to progress in the right direction. Special thanks go to Dr. David Young for his involvement and discussion in the spectroscopic analysis part, which I learned a lot from him.

I felt thankful to my committee members, Professor Sumit Sharma, Professor Katherine Cimatu and Dr. Klaus Himmeldirk, for serving as my committee members and their valuable comments and discussion for the dissertation

I would also like to recognize Becky Gill for her administrative work, your optimistic personality made my experience in the US more colorful. Many thanks to technicians, Mr. Alexis Barxias and Mr. Cody Shafer, for their technical assistance. Thanks go to all the fellow students, post-docs, staff and visiting scholars at ICMT, for being the best friends and partners in my life journey.

TABLE OF CONTENTS

LIST OF TABLES

LIST OF FIGURES

CHAPTER 1: INTRODUCTION

Modern production and transportation of oil and gas implies ever higher requirements, in terms of efficiency, environmental protection, and personnel safety. Those concerns have driven researchers to continually investigate what factors can affect the integrity of pipelines. Much effort has been made to understand the role of CO_2 in internal corrosion, due to the ubiquitous presence of this corrosive gas in wells and geologic formations [1–13]. Consequently, the understanding of CO_2 corrosion has progressed significantly over the past thirty years and is, today, relatively well established. Many models have been formulated to predict CO_2 corrosion [6,8,14]. They show good agreement with laboratory and field measurements and provide important insights for industrial operations, either helping pipeline design or with failure analysis. However, researchers have mostly focused their efforts on understanding phenomena associated with CO_2 corrosion at low temperatures and pressures (<100°C, <70psi) for two reasons: firstly, the conditions have historically corresponded to most production wells [15,16]; secondly, high temperature, high pressure (HTHP) testing holds many challenges related to experimental methods and environment control.

In recent years, the depletion of reservoirs in relatively shallow geologic environments has compelled the petroleum industry to search for and extract oil and gas from deeper geologic formations [16–18]. Accordingly, an increasing number of HTHP wells (>100°C, >70psi) have been put into operation. In these conditions, the knowledge developed at lower temperature and pressure is insufficient and cannot be easily extended

to more severe environments, although recently some efforts have been reported to address this gap; at least for temperature up to 250°C [19–22].

To mitigate internal CO_2 corrosion, many strategies have been developed and brought into operations associated with production. In the oil and gas industry, expensive corrosion resistant alloys (CRA) have been used as an alternative to carbon steels [23,24], which are cheaper materials but are much more prone to corrosion. However, carbon steel is still by far the most widely used fabrication material, mainly due to its low cost and wide availability. The mitigation of CO_2 corrosion of carbon is naturally a major operational issue that can have tremendous financial consequences. Among many methods used to mitigate pipeline degradation, the use of corrosion inhibitors is the most popular in the industry; primarily due to its reasonable price and excellent performance. Much research effort has been devoted to studying the performance of corrosion inhibitors and their inhibition mechanisms [25–33], although significantly more progress needs to be achieved.

As for its CO_2 corrosion counterpart, the understanding of corrosion inhibition at elevated temperatures is even more limited. In addition, most of the research effort, even at low temperature, has been focused on 'pass-fail' testing of new corrosion inhibitors as candidates for use [34–40] instead of on mechanistic studies. Although some of these efforts have been valuable in developing solutions for high temperature corrosion mitigation issues [35,39], they have failed to identify the controlling mechanisms necessary for effective inhibitor design and selection. Indeed, awareness of corrosion inhibition mechanisms is essential to design strategies for corrosion protection at higher

temperatures. This is especially true considering that CO_2 corrosion behaves quite differently at high temperatures compared to low temperatures. The differences are mainly related to enhanced reaction kinetics (higher corrosion rate) as well as the formation of a somehow unexpected corrosion products, namely, Fe_3O_4. This, in turn, very likely affects the performance of corrosion inhibitors. However, only a handful of research works have focused on understanding inhibition mechanisms at elevated temperatures [39].

The research described in this dissertation is an attempt to address this gap by conducting a series of novel experiments and investigating inhibition mechanisms over a wide range of temperatures (25°C to 150°C) in CO_2 saturated environments. Two corrosion inhibitors, widely used at low temperatures, were chosen: an imidazoline-type inhibitor and quaternary ammonium type inhibitor. While the two inhibitors are not expected to perform perfectly at high temperature, the investigation of their modes of failure could clarify what makes a corrosion inhibitor successful or not at elevated temperatures. The loss of inhibition at high temperature has been commonly attributed to two main factors: adsorption/desorption kinetics and/or inhibitor degradation. Consequently, the adsorption behavior and inhibition performance of the two candidate inhibitors were investigated at the tested temperatures. In addition, the effect of the thermal stability of these inhibitors was also examined and discussed.

CHAPTER 2: LITERATURE REVIEW

2.1 CO_2 Corrosion Mechanisms

CO_2 corrosion represents a significant problem for the oil and gas industry. The ubiquitous presence of corrosive gases such as CO_2 in produced fluids represents a real threat to pipeline integrity. CO_2 corrosion has been studied in depth over the last few decades [1–4,6–9,11–13] and the understanding of the mechanisms involved has greatly improved. Three main phenomena can be used to describe CO_2 corrosion: water chemistry, electrochemical reactions at the metal surfaces and the development of corrosion products. This section represents a summary of these three main topics.

2.1.1 Water Chemistry

CO_2 only becomes corrosive when it dissolves in water and when the water comes in contact with a pipeline surface. In oil and gas production, an aqueous phase (brine) is always present in the produced fluids, together with hydrocarbon products. While the aqueous phase may not always be present at a large enough content to wet the pipe (this depends on water cut and flow rates), it still holds a corrosive potential. Therefore, a comprehensive understanding of water chemistry is essential in determining CO_2 corrosion mechanisms. Many efforts have been dedicated to clarifying the main aspects of water chemistry in a CO_2-containing environment [1,3,7]. The main reactions involved in H_2O/CO_2 systems are given below.

Gaseous CO_2 first dissolves in water.

CO_2 dissolution
$$CO_{2(g)} \rightleftharpoons CO_{2(aq)} \tag{1}$$
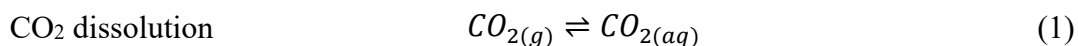
Aqueous CO_2 then reacts with water and forms carbonic acid.

CO₂ hydration $$CO_{2(aq)} + H_2O_{(l)} \rightleftharpoons H_2CO_{3(aq)} \qquad (2)$$
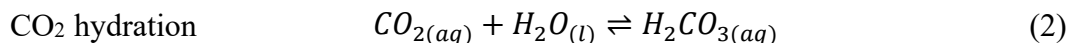
Carbonic acid is a weak acid and partially dissociates into hydrogen ions and bicarbonate ions.

Carbonic acid dissociation $$H_2CO_{3(aq)} \rightleftharpoons H^+_{(aq)} + HCO^-_{3(aq)} \qquad (3)$$
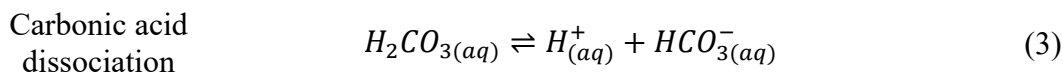
Bicarbonate ions further dissociate into hydrogen ions and carbonate ions.

Bicarbonate ion dissociation $$HCO^-_{3(aq)} \rightleftharpoons H^+_{(aq)} + CO^{2-}_{3(aq)} \qquad (4)$$
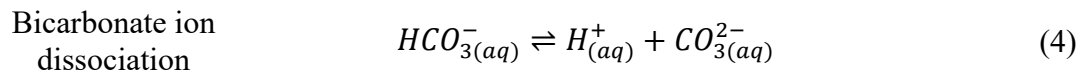
In addition, water molecules can dissociate into hydrogen and hydroxide ions.

H₂O dissociation $$H_2O_{(l)} \rightleftharpoons H^+_{(aq)} + OH^-_{(aq)} \qquad (5)$$
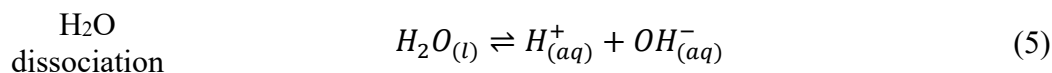
The equilibrium constants with reported empirical expressions for those reactions are listed in Table 1.

To establish a water chemistry model in a CO₂-containing solution, one more equation is needed considering the six unknown species (assuming the partial pressure of CO₂ (pCO₂) is known). This additional equation is usually related to mass conservation. For example, in an open system (with continuous sparging of invariable partial pressure of gaseous CO₂), the additional equation is based on the charge neutrality, as shown in Equation (11).

Table 1. Equilibrium constants and their empirical expressions in H_2O/CO_2 system.

Equilibrium constant		
CO_2 dissolution constant	$K_{sol} = \frac{14.5}{1.00258} \times 10^{-(2.27+5.65\times10^{-3}T_f-8.06\times10^{-6}T_f^2+0.075\times I)}$ molar/bar	(6)[41]
CO_2 hydration constant	$K_{hy} = 2.58 \times 10^{-3}$	(7)[42]
Carbonic acid dissociation constant	$K_{ca} = 387.6 \times 10^{-(6.41-1.594\times10^{-3}T_f+8.52\times10^{-6}T_f^2-3.07\times10^{-5}p-0.4772\times I^{\frac{1}{2}}+0.1180\times I)}$ molar	(8)[41]
Bicarbonate ion dissociation constant	$K_{bi} = 10^{-(10.61-4.97\times10^{-3}T_f+1.331\times10^{-5}T_f^2-2.624\times10^{-5}p-1.166\times I^{\frac{1}{2}}+0.3466\times I)}$ molar	(9)[41]
H_2O dissociation constant	$K_{wa} = 10^{-(29.3868-0.0737549\times T_K+7.47881\times10^{-5}\times T_K^2)}$ molar^2	(10)[43]

Note: T_f means temperature in Fahrenheit degrees, T_K is temperature in Kelvin. I is ionic strength in mol·l^{-1}, and p is the pressure in psi.

$$c_{H^+} = c_{HCO_3^-} + 2c_{CO_3^{2-}} + c_{OH^-} \tag{11}$$

Where, c is the concentration of species in mol·L^{-1}.

Similarly, the rule of mass conservation still applies for a closed system. In a closed system, the partial pressure of CO_2 is not constant due to its dissolution in water and the series of dissociation reactions shown in Reactions (1) to (4). However, the total carbon in all the carbon containing species (CO_2, H_2CO_3, HCO_3^-, CO_3^{2-}) is constant in the closed system. The mass balance is illustrated in Equation (12).

$$M_{CO_{2(g)}} + M_{CO_{2(aq)}} + M_{H_2CO_3} + M_{HCO_3^-} + M_{CO_3^{2-}} = constant \tag{12}$$

M is the total amount of species in moles.

With equation (11) or (12), the water chemistry can be accurately predicted in either an open system or a closed system. However, as corrosion progresses, Fe^{2+} is

released in the CO_2 containing solution and can react with carbonate ions and precipitate to form $FeCO_3$. More details concerning this phenomenon are introduced in detail in section 2.1.3 which discusses the formation of corrosion products.

2.1.2 Surface Electrochemical Reactions

Corrosion is a phenomenon which involves a combination of electrochemical reactions occurring at the steel surface. The overall reaction describing aqueous CO_2 corrosion is summarized in Reaction (13). If $FeCO_3$ forms, as is discussed in section 2.1.3, the overall reaction evolves to Reaction (14).

$$Fe_{(s)} + CO_{2(g)} + H_2O_{(l)} \rightarrow Fe^{2+}_{(aq)} + CO^{2-}_{3(aq)} + H_{2(g)} \qquad (13)$$

$$Fe_{(s)} + CO_{2(g)} + H_2O_{(l)} \rightarrow FeCO_{3(s)} + H_{2(g)} \qquad (14)$$
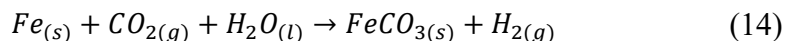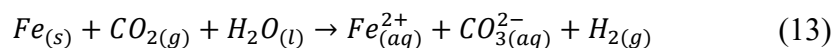
Although the overall reaction of CO_2 corrosion is fairly straightforward, it is comprised of a set of half reactions which includes anodic (oxidization) and cathodic (reduction) reactions.

Anodic reactions

The main anodic reaction is the electrochemical dissolution of iron in aqueous solution:

$$Fe_{(s)} \rightarrow Fe^{2+}_{(aq)} + 2e^- \qquad (15)$$
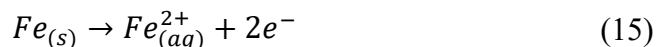
This reaction is in fact a multi-step reaction. The rate-determining step (RDS) is related to the concentration of OH^-. However, the relationship between the concentration

of OH^- and rate of anodic reaction is complicated. Nesic, *et al.,* [8] investigated the anodic reaction and summarized its rate expression as:

$$i_a = k(c_{OH^-})^{a_1}(pCO_2)^{a_2}10^{\frac{E}{b_a}}$$ (16)

i_a is the anodic current density ($A \cdot m^{-2}$), E is the over potential (V), b_a is the Tafel slope (mV/decade), a_1, a_2 and k are constants.

From this equation, it can be seen that the rate of the reaction is a function of pH and CO_2 partial pressure. In addition, pH also affects the value of a_1. When pH is lower than 4, pH has a notable effect on the dissolution rate (a_1=2). However, when pH>5, the role of pH is no longer significant, and hence a_1=0. Similarly, the effect of pCO_2 is also not straightforward. The effect of pCO_2 only matters when pCO_2<0.1 bar (a_2=1), and its effect fades when pCO_2 is higher than 0.1 bar, and hence a_2=0. Moreover, the kinetics of the anodic reaction is also dependent on the materials involved.

Cathodic reactions

Generally, the major three cathodic reactions in the CO_2 saturated environment are:

Hydrogen reduction	$2H^+_{(aq)} + 2e^- \rightarrow H_{2(g)}$	(17)
Carbonic acid reduction	$2H_2CO_{3(aq)} + 2e^- \rightarrow H_{2(g)} + 2HCO^-_{3(aq)}$	(18)
Water reduction	$2H_2O_{(l)} + 2e^- \rightarrow H_{2(g)} + 2OH^-_{(aq)}$	(19)
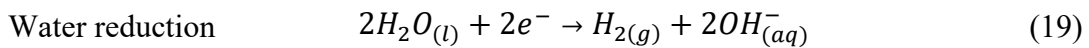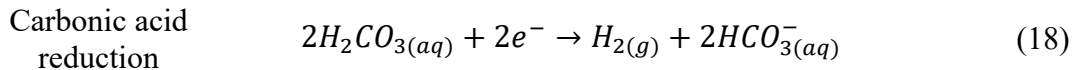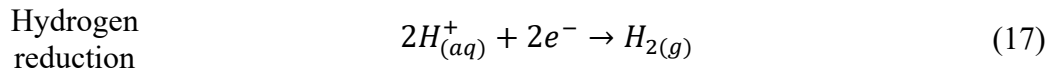
The reduction of carbonic acid has been the focus of more recent research efforts. De Waard and Milliams [1] investigated the corrosion of steel in two aqueous environments: one containing only a strong acid and the other saturated with CO_2. The authors found that at the same pH, the CO_2-saturated solution was more corrosive than the strong acid solution. They explained this behavior by the existence of an additional reduction reaction, as shown in Reaction (18), and labeled it as "direct reduction of carbonic acid". The direct reduction of carbonic acid was also postulated by other researchers [2–4,6]. Gray, *et al.,* [2,3] conceived that hydration of dissolved CO_2 was the rate determining step. Later on, Nesic, *et al.,* [8] further incorporated the diffusion of H^+ ions and carbonic acid in the overall corrosion mechanism.

However, Remita, *et al.,* [11] rejected the existence of direct reduction of H_2CO_3. Instead, they showed that the experimental results did not require an additional reduction reaction and could, in fact, be explained by considering carbonic acid as a provider of hydrogen ions (buffering effect). However, the contribution of hydrogen ions and carbonic acid to the overall current could not be clearly differentiated in the tested conditions as the corrosion process was never entirely under charge transfer controlled. Nevertheless, the authors were the first to develop a model entirely based on the H_2CO_3 buffering effect, ignoring the direct reduction of H_2CO_3. They found that the measurements still agreed well with the model without consideration of H_2CO_3 direct reduction. Linter and Burstein [44] also mentioned that the reduction of H_2CO_3 was thermodynamically unfavorable compared to the reduction of hydrogen ions.

More recently, Tran, *et al.,* [45] and Kahyarian, *et al.,* [12,13] extended this work by considering different substrate materials (316L stainless steel) and different experimental conditions specifically chosen to highlight the charge transfer part of the reduction reactions, hence showing clearly if H_2CO_3 could have an effect on the overall reduction kinetics. The authors found no sign of H_2CO_3 direct reduction in any conditions tested and could explain all the results by only considering the hydrogen ion reduction. However, the anodic reaction seemed to be affected by the presence of CO_2 although the underlying multistep mechanisms remained somehow elusive.

In conclusion, although much progress has been made in identifying and characterizing the cathodic and anodic reactions involved in the corrosion mechanisms, efforts are still ongoing to clarify some basic aspects of the electrochemical process.

2.1.3 Formation of Protective Corrosion Product Layers

As mentioned in the previous two sections, the formation of corrosion product layers usually happens when the concentration of Fe^{2+} ions, produced by the dissolution of iron, and the concentration of CO_3^{2-} ions, generated when CO_2 dissolves in the water (Reactions (2)-(4)), exceed the solubility of iron carbonate, as shown in Reaction (20). To simplify this concept, saturation of the iron carbonate is introduced and defined in Equation (21) ($K_{spFeCO3}$ is the solubility of iron carbonate). The formation of the corrosion product consequently creates a diffusion barrier for the corrosive species such as hydrogen ions. Due to the protective nature of iron carbonate, its formation is also a topic of great interest in CO_2 corrosion research [9,28,46].

$$Fe^{2+}_{(aq)} + CO^{2-}_{3(aq)} \leftrightarrow FeCO_{3(s)} \qquad (20)$$
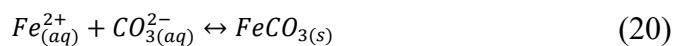
$$S_{FeCO_3} = \frac{c_{Fe^{2+}} c_{CO_3^{2-}}}{K_{spFeCO_3}}$$ (21)

Another important concept which is used to describe the protectiveness of the iron carbonate layer [47] is scaling tendency (ST), which is given in Equation (22). In this equation, PR stands for the precipitation rate and CR the corrosion rate, which are both expressed in $mm \cdot y^{-1}$. ST, representing the protectiveness of the corrosion product layer, is higher when the precipitation rate is high and the corrosion rate is low. If the corrosion rate is too high, the metal substrate underneath the layer can be easily dissolved away and makes it difficult for the corrosion product to bond with the metal effectively and physically. This is called the undermining effect. A dense and protective layer only forms when the precipitation rate is fast enough to balance the undermining effect.

$$ST = \frac{PR}{CR}$$ (22)

CO_2 corrosion is a relatively complex phenomenon that is influenced by many parameters. The next sections present a review of the main effects of common operating parameters on CO_2 corrosion.

2.1.4 Influential Factors

As discussed in 2.1.1 to 2.1.3, CO_2 corrosion involves a number of physical and chemical phenomena that interact with each other in a complex way. The change of water chemistry alters the reactant concentrations and hence the rates of surface electrochemical reactions. The overall electrochemical process in CO_2 corrosion of steel generates ferrous ions and consumes H^+, which in turn, changes the water chemistry. In addition, if the concentration of Fe^{2+} ions, produced by surface electrochemical reactions,

and the CO_3^{2-} ions, generated by the dissolution and dissociation of carbonic species in water, reaches a critical concentration, the precipitation of corrosion products can occur. This would reduce the rate of electrochemical reactions, by creating a diffusion barrier, and change, in turn, the water chemistry. In the following sections, the effect of the main operating parameters on CO_2 corrosion is introduced.

Effect of pH

Generally, corrosion rate increases with decreasing pH. The H^+ ion is an important oxidant in the corrosion of mild steel in CO_2 environments. At a lower pH, the concentration of H^+ ions is higher in the electrolyte and the rate of reaction (17) increases. Secondly, pH also influences the formation of corrosion products. The equilibrium constant of reaction (20) is a function of pH, with the solubility of $FeCO_3$ increasing as pH decreases, creating a less favorable environment for the formation of $FeCO_3$. This, in turn, also influences the corrosion rate.

Effect of CO_2 Pressure

CO_2 partial pressure is another important parameter playing a central role in the corrosivity of the CO_2-containing environment. CO_2 is an acid gas which can be hydrated into a weak acid, H_2CO_3. This weak acid generates additional H^+ ions through reaction (1) to reaction (4). The reduction of H^+ and H_2CO_3 are the main cathodic reactions in CO_2 corrosion. Therefore, the corrosion rate generally increases with the CO_2 partial pressure until operating conditions favor the formation of $FeCO_3$ (high pH, high Fe^{2+} and CO_3^{2-} concentrations).

Effect of Temperature

The temperature dependence of corrosion rate is also complicated. On one hand, the electrochemical reaction rates increase with increasing temperature. On the other hand, a higher temperature also facilitates the formation of iron carbonate by increasing its precipitation rate and by decreasing its solubility through reaction (20). Therefore, the corrosion rate does not change unitarily with temperature. Due to these balancing effects, the corrosion rate of steel in an aqueous environment subjected to 1 bar CO_2 has been reported to increase with temperature below 80°C and then decrease at temperature above 80°C due to the formation of protective $FeCO_3$ layer [1].

The role of high temperature (>80°C) should be especially examined, since it is a central concern of this research topic. Generally, high temperature affects CO_2 corrosion not only kinetically but also thermodynamically. Tanupabrungsun, *et. al..,* [19] found that at temperatures above 120°C, the formation of another corrosion product, Fe_3O_4 (magnetite), is thermodynamically favored. The presence of Fe_3O_4 was later confirmed in experiments at 150°C in the presence of CO_2 [22]. Potter and Mann [48] reported that the kinetics of formation of Fe_3O_4 takes the form of a parabolic law. In the presence of a magnetite layer, the corrosion rate was found to be governed by the slow diffusion of soluble iron ions through the magnetite layer, which is usually the rate controlling step. Therefore, the thickness of the magnetite layer is one of the key factors influencing the corrosion rate at elevated temperatures. However, the current understanding of the effect of magnetite on CO_2 corrosion is still relatively limited due to the complexity of high

temperature testing methods. Its potential effect on corrosion inhibition, which is the topic of this work, remains largely unknown.

Effect of Flow

The effect of the flow is mainly seen through the enhancement of mass transport of the reactants to as well as away from the metal surface. H^+ ions, which are transported more readily to the metal surface, increase cathodic reaction rates. At the same time, Fe^{2+} ions easily diffuse away from the metal surface rendering the precipitation of corrosion products less likely. Therefore, with more reactant available, the corrosion rate usually increases with higher flow [8,10,14]. However, this effect is considerably minimized in the presence of corrosion product precipitates, since mass transfer limitation through a dense layer becomes the controlling step and is not as readily affected by bulk flow conditions. In addition, some researchers [49–51] believed that high flow velocity can cause the failure of protective corrosion product layers. Li, *et. al.,* [52] disproved the likelihood of mechanical removal of corrosion products ($FeCO_3$) through direct measurement of wall shear stress. They found that shear stresses in typical multiphase flow environments are only of the order of 10^3Pa, which is much less than the mechanical stresses needed to remove the corrosion product layers (50-100MPa).

2.2   Corrosion Inhibitors in the Oil and Gas Industry

2.2.1 Introduction

As discussed earlier, costs associated with corrosion in the oil and gas industry are considerable. Although CRAs are available, low alloy carbon steels are still the primary construction materials in the industry due to economic reasons. Although those materials

possess suitable mechanical properties, they are susceptible to corrosion during

production and processing operations. The corrosion of those materials can lead to loss of

integrity, leakages in casing, tubing and other related facilities, which could create

serious issues such as loss of life and environmental pollutions. The economic impact of

corrosion can be enormous; Tems and Al-Zahrani, *et al.,* [53] presented that the

economic costs related to CO_2 corrosion and oil refining plants can add up to 10% to 30%

of the maintenance budget.

Traditional corrosion mitigation methods include cathodic protection, coatings

and the use of corrosion inhibitors [54,55]. However, cathodic protection is only

applicable to external corrosion and where the structure to be protected is readily

accessible. Coatings are also mainly used against external corrosion as their application

requires routine maintenance. They can indeed be used on the internal surface of

pipelines but are damaged during the process of welding/joining pipe sections [56].

Inspections and repairs are challenging if not impossible and small undetected damaged

areas can lead to major failure, requiring facilities shut down and major economic losses.

In comparison, the use of corrosion inhibitor presents many advantages for

internal corrosion. First, inhibitors can be directly injected in the flow without affecting

production and their use is relatively versatile as injection rates can be adjusted easily

[57]. Secondly and most importantly, its associated costs are low compared to other

mitigation techniques. This being said, many challenges also exist with the use of

corrosion inhibitors. The selection of the appropriate chemical and dosage is a necessary

and complicated step which requires comprehensive evaluation in simulated laboratory

environments. From an operational standpoint, it requires constant attention: discontinued inhibitor injection or injection at the wrong dosage are unfortunately too common. Issues related to partitioning (the inhibitor may have a tendency to accumulate in the oil phase) and with degradation (after exposure to harsh environments) also need to be taken into consideration. Proper monitoring of inhibitor concentration is possible but field reality often prioritizes production continuity over corrosion mitigation requirements [58]. Nevertheless, corrosion inhibitors have been used very effectively and extensively in oil and gas fields. In fact, the application of corrosion inhibitor as a mitigation method is not limited to the oil and gas industry – they are very common in packaging, automotive industry, chemical processing, etc. The presents review focuses on inhibitor formulations and experiences related to oil and gas production.

2.2.2 Adsorption Mechanisms

Since the basic working principle of most inhibitors is related to adsorption on metal surfaces, the study of the adsorption behavior of inhibitors is very important [59–62]. Adsorption mechanisms of inhibitors can be classified as physisorption and chemisorption. Physisorption occurs by electrostatic attraction between inhibitor ions or intramolecular dipoles and a charged metal surface, whereas chemisorption involves the formation of primary bonds between an iron surface and the adsorbed molecules [55]. Although it is known that the inhibition performance of inhibitors is directly related to their adsorption behavior, how inhibitor adsorption occurs is often poorly understood.

Physisorption

Physisorption involves an interaction between an adsorbent and an adsorbate, typically being governed by opposite charges being present. When a metal is placed in an electrolyte, its surface acquires a charge due to the adsorption and orientation of water molecules forming into a double layer [63]. Inhibitor molecules can also be charged (anions or cations) and have polar groups capable of forming an induced dipole. For example, the N atom in imidazoline molecules, or structural moieties, can be easily protonated [64]. The molecular polarity, charge, and ability to bond to the metal surface depends on the presence of lone pairs of electrons, π-electron clouds (aromatic ring systems), and functional groups. When both metal surface and inhibitors molecules are oppositely charged, Coulombic forces facilitate inhibitor adsorption onto the surface. Here, it is very important to introduce the concept of potential of zero charge (PZC), the potential of the electrode (*vs.* a given reference electrode) when the surface charge on the electrode is zero [65]. Amin, *et al.*, [66] found the steel surface was positively charged *vs.* the PZC. Chloride ions (Cl^-) in solution are then naturally attracted to the surface. The adsorption of Cl^- also facilities the subsequent physisorption of cationic inhibitors, by acting as linkage between the positively charge surface and the positively charged cationic inhibitor molecule. Oguzie, *et al.,* [67] found that introduction of iodide ions (I^-) improved corrosion inhibition efficiency of methionine (MTI). They believed that the iodide ions were directly adsorbed on the mild steel surface and serve as adsorption sites for protonated MTI molecules (cationic inhibitors), which were drawn onto the surface.

Chemisporption

Chemisorption is related to the formation of chemical bonds between the metal and the inhibitor molecules that contains unsaturated π bonds. Moretti, *et al.,* [68] hypothesized that tryptamine (TA), which has high electron density, chemisorbed on the iron surface. In addition, they found that its adsorption Gibbs energy increased with temperature, which suggested that a complexation-type surface reaction occurred between iron and inhibitor molecules. This phenomenon can be categorized into chemisorption as well. Tedeschi, *et al.,* [69] illustrated the basic working mechanism of chemisorption for an acetylenic corrosion inhibitor. They hypothesized that the inhibitor adsorbed on the surface through charge transfer from the π bond of the acetylenic group to the iron surface to form a coordinate type of bond.

The most recognized method to evaluate whether an inhibitor was physisorbed or chemisorbed on metal surfaces is based on its adsorption Gibbs energy (ΔG°_{ads}) calculated from inhibition efficiency. It was proposed that an inhibitor with a value of ΔG°_{ads} around $-20 kJ \cdot mol^{-1}$ is physisorbed on metal surface while ΔG°_{ads} around $-40 kJ \cdot mol^{-1}$ is chemisorbed inhibitor [70–72]. However, this classification might not be reliable due to the lack of a sound theoretical basis. The Gibbs energy only reflects the spontaneity of a reaction and is not directly related to the binding energy, which is a key difference between physisorbed and chemisorbed corrosion inhibitor. In addition, there is much evidence against this simple classification. Souza, *et al.,* [73] found that a caffeic acid has ΔG°_{ads} of $-27.3 kJ \cdot mol^{-1}$, which is likely a physisorbed corrosion inhibitor according to the category. However, by using Raman spectroscopy, it was found that the

structure of the inhibitor was different when it was in a 'pure compound' form compared to when it was adsorbed on the electrode surface, indicating a possible chemisorption mechanism. Therefore, it can be seen that the classification of the adsorption mechanisms based on the value of ΔG°_{ads} is not completely valid. This method requires further investigation and evaluation.

2.2.3 Types of Corrosion Inhibitors

Corrosion inhibitors used in the oil and gas industry are usually molecules containing one or more functional groups that have one or more heteroatoms (N, O, S, P). These atoms, directly or indirectly, play the role of anchoring the inhibitor onto the metal surfaces. This is important since the first stage of the inhibition in the corrosive media is by adsorption of inhibitors on metal surfaces. Many different types of chemical compounds or packages of chemical compounds are used in the industry to mitigate CO_2 corrosion. Here, the most widely used inhibitors are introduced and listed by different functional groups.

Imidazoline-Based Inhibitor

One of the most extensively used inhibitors is the imidazoline-type inhibitor. This inhibitor usually consists of three parts (as shown in Figure 1): a 5-member imidazoline head ring, a pendant chain and a long hydrocarbon chain of various carbon numbers. The imidazoline ring has two nitrogen atoms which work commonly as the adsorption sites; the side chain is considered as an anchor to the molecules [32,74] (-R_2 group); the long hydrocarbon chain (-R_1 group), usually hydrophobic, can drive the molecule towards the interface and also act as a barrier against water molecules and other corrosive species.
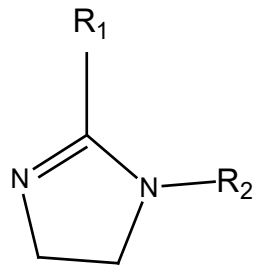
Figure 1. Schematic of a general imidazoline-type inhibitor

Quat-Type Inhibitor

Quat-type inhibitor, as indicated in its name, mainly consists of a quaternary ammonium group (see Figure 2). In the molecule, the nitrogen atom is the main adsorption site. In addition, it is likely that it involves only electrostatic-type interactions with surface (physisorption) attraction as there is no lone-pair or π-electrons present within its molecular structure. The R1, R2, R3 usually are short chain alkyl groups. R4 is a long hydrocarbon chain, which also acts as a repellent to water molecules and corrosive species, as for the imidazoline-type inhibitor.
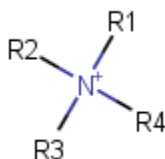
Figure 2. Schematic of a general quat-type inhibitor

Other Typical Inhibitors in Oil and Gas Industry

The imidazoline-type and quat-type inhibitors are the most extensively used inhibitors in the oil and gas industry. However, other inhibitors are also used for different purposes. Acetylenic type inhibitor, which contains an ethynyl group, has a significant role in high temperature inhibition. Although it is reported to be very effective against high temperature corrosion, its effectiveness is critically dependent on the pH (usually <1) and mainly used against corrosion during pickling and acid cleaning during oil and gas production [75,76]. However, the pH in CO_2-saturated environments, which are of interest in the present study, is usually only between 4 and 7. In addition, high doses of acetylenic-type inhibitor are required to be effective (10 wt.% and above), which makes it neither practical nor cost-effective. Therefore, the acetylenic type inhibitor is not a good candidate for inhibiting high temperature corrosion for internal pipeline applications.

Another widely used inhibitor is phosphate-type inhibitor. This inhibitors has a similar structure compared to quat-type inhibitor except for a P atom which plays the role of adsorption site instead of the nitrogen atom. This inhibitor is also a good scaling inhibitor, which can be used against the formation of scales ($CaCO_3$, $MgCO_3$, etc.) and therefore prevent the blockage of pipelines [77–79]. However, this type of inhibitor is also particularly dangerous for the environment. It can pollute the water sources and endanger the safety of wildlife and humans [55]. It is therefore not commonly used in corrosion mitigation in pipelines in modern days.

In summary, the most commonly used inhibitors for oil and gas field applications are still the imidazoline-type and quat-type inhibitors. Therefore, those two inhibitors
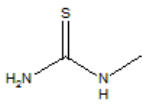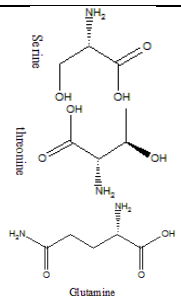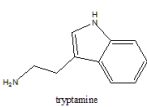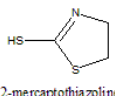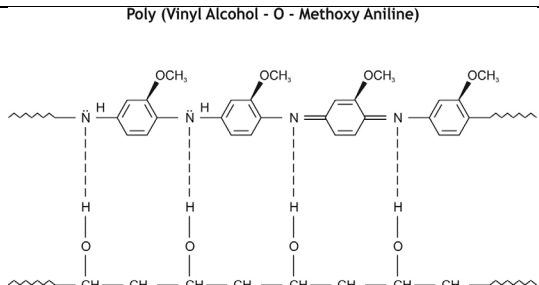
were investigated in the current research. One more important thing that needs to be pointed out is that these inhibitors are not usually used solely as it is but as a part of a package of chemical compounds [57]. This is because organic compounds themselves have many limitations such as low solubility in the aqueous phase, high viscosity, etc. These limitations make the operational use of inhibitors difficult. Therefore, a proper package containing solvents, co-solvents, intensifiers and other ingredients is often used in the field applications.

2.2.4 Effect of Temperature on Corrosion Inhibition

As introduced earlier, little has been reported on the high temperature corrosion inhibition and its mechanism. However, there is extensive literature regarding low temperature corrosion inhibition (15°C to 65°C). It seems rather natural that understanding the mechanisms of corrosion inhibition at low temperature should serve as a solid foundation for investigation at higher temperatures.

Available literature on the effect of temperature on the inhibition efficiency is rather confusing. The inhibition efficiency of particular inhibitors has been shown to decrease with temperature [32,66,80], whilst in other cases it increased with temperature [68,81]. Others have reported that the effect of temperature for a particular inhibitor is dependent on the temperature range under study [82]. Some examples of temperature effects on different inhibitors are shown in Table 2.

Table 2 Temperature effect on Inhibition Efficiency (IE) on various corrosion inhibitors

Inhibitor	Inhibitor Formula	Temperature Effect on IE of Mild Steel
Methylthiourea		IE decreased with temperature (30-50°C) [80]
Amino acids: Serine, Threonine, Glutamine		IE decreased with temperature (10-60°C) [83]
Tryptamine		IE increased with temperature (25-55°C) on ARMCO iron [84]
2-mercaptothiazoline		IE increased with temperature(25-55°C) [81]
Vinyl alcohol-o-methoxy aniline		IE first increased with temperature (30-50°C) then decreased with temperature (50-70°C) [82]

The understanding of the complex interactions between temperature and inhibition efficiency is quite limited. It was generally believed that the role of temperature on the inhibition performance is related to the adsorption mechanism of the inhibitor. Inhibitors whose efficiency decreases with temperature are frequently interpreted as being physisorptive inhibitors; the reverse effect, when the inhibition efficiency increases with temperature, suggests a chemisorption mechanism [84–90].

However, as far as the mechanisms behind these assertions are concerned, the understanding is still limited. Bentiss, *et al.,* [85] studied the role of a thiadiazole-type inhibitor on the corrosion behavior of mild steel in an acidic environment at different temperatures (30°C-60°C). They found that the efficiency of the inhibitor increased with temperature and attributed the temperature dependency as a sign of the chemical adsorption. However, there was no further discussion on what correlates the temperature-dependent behavior with the nature of chemisorption. Popova, *et al.,* [91] investigated the effect of temperature (20°C-60°C) on mild steel corrosion with and without derivatives of benzimidazole derivatives. The inhibitors' performance was found to generally decrease with an increase in temperature, which could be related to the physisorptive nature of these inhibitors. In addition, to prove the nature of physisorption, they also investigated the role of anions by the addition of potassium iodide (KI) and found a synergistic effect between KI and the inhibitors. Therefore, they concluded that the adsorption of the benzimidazole derivatives was likely through the electrostatic adsorption of the protonated form of the compounds. Although they confirmed the likelihood of the physical adsorption of the inhibitor, the authors provided no further explanation of how temperature affects adsorption behavior.

In addition, the effect of temperature can be not limited to adsorption behavior. Most inhibitor molecules are organic and their molecular structure is sensitive to temperature. Therefore, thermal stability could be another important consideration, especially at high temperatures (150°C-250°C). However, the thermal stability of corrosion inhibitors is usually neglected. This is expected because most inhibitors are

required to be thermally stable, which means that there should be no chemical degradation through hydrolysis, condensation, polymerization, etc. [92]. Therefore, the stability of inhibitors is usually pre-tested before application. Solmaz, *et al.,* [81] investigated the thermal stability of 2-mercaptothiazoline (2-MT) corrosion inhibitor using thermogravimetric analysis (TGA). They found that 2-MT exhibited a relatively good thermal stability. The TGA curve for pure 2-MT compound showed only one instant weight loss at 170°C (up to 440°C), which could be related to the loss of moisture and impurities. However, the working temperature of this inhibitor was only up to 90°C. Therefore, the inhibitor should still provide a high protective efficiency under the tested environments without considering the effect of its degradation. However, growing concerns have been paid to the role of the thermal stability of corrosion inhibitors. Zheng, *et.al.,* [93] investigated the durability of 2-mercaptobenzimidazole (MBI) in a post-combustion CO_2 capture system using long-term immersion corrosion tests. They found that the inhibitor degraded at pressure above 4.13×10^5 Pa and temperature above 108°C and the degradation led to the formation of a non-protective FeS layer on the metal surfaces. Therefore, it is suggested that the corrosion inhibitors with thiol group might not be a good candidate for high temperature environments.

On the other hand, some molecules, like acetylenic corrosion inhibitors, can react with each other at high temperature and form into polymerized multilayers [69],[94], hence increasing inhibition efficiency [75]. Consequently, the molecular degradation of corrosion inhibitors does not necessarily lead to a decrease in the performance of corrosion inhibitors. In conclusion, the high temperature effect on the thermal stability of

inhibitor molecules is complicated and needed to be investigated separately according to different inhibitors.

As far as the imidazoline-type inhibitor is concerned, there is still no consensus on how temperature affects its behavior. Okafor, *et al.,* [95] investigated the inhibition and adsorption behavior of 2-undecyl-1-ethylamino imidazoline (2UEI) in a CO_2-saturated 3 wt.% solution using various electrochemical methods. They found that the increase of temperature led to an increase in the inhibition efficiencies of this imidazoline-type inhibitor. They also measured the ΔG°_{ads} as $-48.18 kJ \cdot mol^{-1}$, and proposed the chemical adsorption mechanism of this inhibitor. Therefore, they attributed the increased performance of the corrosion inhibitor at higher temperatures as a result of its chemisorptive behavior. They also investigated the inhibition behavior of a rosin amide imidazoline (RAIM) inhibitor using similar electrochemical methods [96]. Again, they noticed the performance of this inhibitor increased over the tested temperature range and associated the increased efficiency with the chemisorptive nature of RAIM. Other researchers [97] also found that the inhibitive performance of the imidazoline-type inhibitors was enhanced by higher temperatures. However, not all the imidazoline-type inhibitors' performance seems to follow this temperature-dependency. Zhang, *et al.,* [98,99] examined the inhibition performance of three different halogen-substituted imidazoline derivatives (1-IM, 2-IM, 3-IM) for mild steel in a hydrochloric acid solution from 30°C-70°C. They noticed that the performance of the two inhibitors either decreased (1-IM, 3-IM) or only slightly changed (2-IM) at elevated temperatures. Therefore, the authors concluded that these three inhibitors are mainly physisorbed on the

metal surfaces. He, *et al.,* [100] studied the inhibition properties of 2-phenyl-2-imidazoline (2-PI) on AA5052 aluminum alloy in 1M HCl solution. A decrease in inhibition efficiency was also identified in their research. Quiraishi, *et al.,* [101] also investigated the performance of some imidazoline derivatives on the corrosion inhibition of aluminum in acid solutions at various temperatures (30°C-60°C). They found a decrease in inhibition efficiency with a rise in temperature for all the tested imidazoline derivatives. Therefore, it can be seen that the role of temperature on the performance of imidazoline-type inhibitor is still unclear.

In addition, the imidazoline-type inhibitor was reported to be unstable in aqueous solutions. The synthesis of imidazoline-type inhibitor goes through a 2-step dehydration reactions between diamines and carboxylic acids [102,103]. The first dehydration reaction forms into an amide precursor and the second yields the closed-ring final product imidazoline inhibitor. The synthesis reactions usually occur at elevated temperatures (above 150°C) in vacuum conditions [104]. Therefore, the inhibitor molecules are supposed to be stable at lower temperatures. However, Martin and Valone [102] investigated the actual chemical composition of commercially available imidazoline-type inhibitors using various spectroscopic methods (Fourier transform infrared (FTIR), carbon-13 nuclear magnetic resonance (^{13}C NMR), ultraviolet (UV) spectroscopy). They confirmed that the inhibitor formulation changed from imidazoline to its amide precursor with time. More importantly, they found the inhibition performance of the two formulations were not quite different. Other researchers [105] also found that the amide precursor showed a similar inhibition performance. However, Cruz, *et al.,* [106] found

that such an imidazoline-type inhibitor showed a much higher performance than its amide precursor using electrochemical impedance spectroscopy (EIS). Olivares-Xometl, *et al.,* [107] also studied the inhibitor films formed by imidazoline and its amide precursor using gravimetric (weight loss) and many electrochemical techniques. They found that the imidazoline appeared to be a more efficient inhibitor compared to its amide precursor. From the literature reviewed, it can be seen that the thermal stability and its role on the performance of imidazoline-type inhibitor are also not clear.

The temperature effect on the inhibition performance of the quaternary ammonium type inhibitor, the other inhibitor of the current research, is relatively straightforward compared to the imidazoline-type inhibitor. Soror and El-Ziady [108] investigated the performance of cetyl trimethyl ammonium bromide (CTAB) on the carbon steel corrosion in HCl and H_2SO_4 solution from 30°C to 60°C, using weight loss and other electrochemical methods. They discovered that the inhibition performance of CTAB generally decreased over the tested temperature. Deyab [109] studied the corrosion behavior of carbon steel in formation water with the presence of dodecyl dimethyl ammonium chloride (CS) from 30°C to 70°C. The author also found that the inhibition efficiency of CS decreased with increasing temperature. The rather simple pattern of temperature effect of the performance of the quat-type inhibitor might be related to its physisorptive nature. Typically, the quaternary ammonium type inhibitor is cationic and has no unpaired electrons in the molecules for coordinate bonds. Therefore, it can only be physisorbed through electrostatic attraction. Moreover, as far as the thermal stability of the quat-type inhibitor, little has been reported.

Last but not least, the corrosion behavior itself might have certain effects on the adsorption behavior at elevated temperatures. The dissolution of the steel substrate electrode during the corrosion process makes the surface unstable. As a result, the corrosion of electrodes can also affect the adsorptive behavior of inhibitor molecules. Drazic and his coworkers [110,111] suggested that the dissolution rate of metal can enhance the desorption of the inhibitor. Therefore, the inhibition performance might decrease with higher corrosion rates. Moreover, as discussed earlier, corrosion products ($FeCO_3$) can also form over time during the corrosion process and play an important role on the performance of corrosion inhibitors. However, the understanding related to this aspect is still limited [112–114]. In addition, at elevated temperatures, Fe_3O_4, a corrosion product otherwise not commonly encountered at low temperature in the CO_2-containing system, can form. However, the role of Fe_3O_4 on the inhibition performance has yet to be characterized.

In summary, the role of temperature on corrosion inhibition is complex and differs from inhibitor to inhibitor. The understanding of the effect of temperature on inhibitor adsorption behavior is also limited. In addition, most research efforts on temperature effects have only focused on lower temperatures (below 80°C) and the thermal stability of these organic inhibitor molecules are not often discussed. Therefore, it is necessary to investigate the temperature effect on the inhibitors from a mechanistic point of view along with the thermal stability of corrosion inhibitors.

2.2.5 Testing Techniques

Many techniques have been applied to explore the various characteristics of the inhibitor. These techniques can be categorized according to their purposes. Some techniques are mainly used for evaluating inhibition efficiency; some techniques are used for determining the adsorption behavior of the corrosion inhibitor; some are for the characterization of corrosion inhibitors themselves. In this section, these testing methods are introduced separately.

Techniques Used for the Determination of Inhibition Efficiency

Inhibition efficiency is of great concern in corrosion inhibitor research. It is the most important indication of the performance of corrosion inhibitor. Many methods have been used for evaluating the inhibition efficiency. These methods include linear polarization resistance (LPR), polarization sweeps, electrochemical impedance spectroscopy (EIS), and weight loss measurement [115,116].

The evaluation of efficiency of a corrosion inhibitor is usually through the following equation:

$$Inhibition\ efficiency(\eta) = \left(1 - \frac{CR_{inh}}{CR_{uni}}\right) \times 100\% \qquad (23)$$

where, CR_{uni} is the corrosion rate without the addition of corrosion inhibitor, CR_{inh} is the inhibited corrosion rate. LPR, EIS, polarization sweep, and weight loss method can all provide values of CR_{uni} and CR_{inh}. Among these methods, LPR is the most convenient method for determination of η. However, it requires some knowledge of the corrosion mechanisms for calibration and can be therefore less accurate than the weight loss method, especially in solution with a low conductivity [115]. The weight loss method is

the most reliable method to measure the corrosion rate and has a wide range of

applications in various environments even in hydrocarbon phases. Nevertheless, the

method only provides time averaged corrosion rates and cannot help determine the

corrosion trends over time [115,117].

EIS is also a convenient method for the on-line measurement of corrosion rates

[118]. Similarly to LPR, it has limited applications in poorly conductive solutions

because the high solution resistance might compromise the measured polarization

resistance. In addition, this technique is more complicated than LPR and the

interpretation of the data requires some level of expertise that typically limits its

systematic use [57,115].

Techniques Used for Characterizing the Adsorption Behavior of Inhibitor

The inhibition efficiency of an inhibitor is closely related to its adsorption

behavior. Most researchers have assumed that inhibition efficiency ($\boldsymbol{\eta}$) is the same as the

degree of surface coverage by the inhibitor molecule (θ) [29,31,119,120]. This simple

model which assumes that part of the metal surface is fully covered by the adsorbed

inhibitor molecules and part of the surface is completely free goes against recent findings

[121,122]. While the adsorption of inhibitor might lead to a decrease in the corrosion

rate, the degree of the inhibition efficiency is dependent on many factors such as the size

of the inhibitor molecule, the nature of the active sites, the material tested, the solution

chemistry, etc. In addition, the inhibition efficiency, as measured by LPR for example,

cannot provide any in-depth information about the properties of the inhibitor films, such

as the persistence (adhesion force), the viscoelasticity of the films, the structures of the

adsorbed films (number of layers, orientations of the adsorbed inhibitor molecules), etc. Therefore, more efforts are necessary to investigate the adsorption behavior of inhibitors.

Quartz crystal microbalance (QCM) has been primarily used for the studies of thin films on an electrode. The operation of QCM is built on the converse piezoelectric effect of quartz. Jacques and Pierre Curie [123] discovered the piezoelectric effect when they found that when there was mechanical stress applied on the crystal surfaces, an electrical potential was generated across the surface corresponding and proportional to the applied forces. Vice versa, the applied electrical potential can induce mechanical stress on the surfaces. Gunter Sauerbrey [124] used the piezoelectric effect for micro-gravimetric applications. He developed the relationship between the mass changes, due to adsorption or precipitation of molecules/compounds on a substrate, and the frequency change of quartz crystals where the substrate is deposited, as Sauerbrey equation:

$$\Delta f = -2 f_0^2 (\mu_q \rho_q)^{-1/2} \frac{\Delta m}{A} \tag{24}$$

or simply:

$$\Delta f = -C_f \cdot \Delta m \tag{25}$$

where Δf is the measured resonant frequency shift (Hz), f_0 is the original resonant frequency of the quartz crystal without mass loaded (Hz), μ_q and ρ_q are the density and the shear modulus of the quartz, in g cm^{-1}·s^{-2} and g cm^{-3}, respectively. A is the piezoelectrically active area (cm^{-2}), C_f is the sensitivity factor for the crystal, and the negative sign is an indication that the mass increase results in a frequency decrease.

A QCM with a resonant frequency of 5 MHz can detect mass changes as small as several nanograms. Therefore, QCM appears to be an ideal tool study the adsorption of corrosion inhibitors.

Knag, *et al.,* [125] studied the adsorption behavior of CTAB on a gold-coated crystal with the presence of short-chain alcohols using the QCM technique. They found that the addition of short alcohols can reduce the adsorption of CTAB. The addition of the alcohols led to the change of the inhibitor's molecular packing ratio, from spherical aggregates to a bilayer film that is similar to a lamellar crystalline phase. Gutig, *et al.,* [126] measured the adsorption of CTAB (cationic) and $CH_3(CH_2)_{11}(OCH_2CH_2)_6OH$ ($C_{12}E_6$) from aqueous solutions onto the gold and silica surfaces using QCM. Their results indicated that $C_{12}E_6$ formed a monolayer-like structure and CTAB developed a double layer-like structure on both surfaces when the concentration in the solutions exceeds the critical micelle concentration (CMC). Obviously, the use of QCM did improve the understanding of the adsorption behavior and hence the structures of the inhibitor films. However, QCM has a number of limitations. For example, although Gutig, *et al.,* [126] detected the formation of monolayer/bilayer-like structures, they could not determine the accurate structure of the adsorbed films, whether it belongs to monolayers, hemi-cylinders or hemispheres nor between bilayers, cylinders, or spheres. As a result, they always used the term 'monolayer/bilayer-like'. Moreover, many researchers had reported that the QCM measurement might overestimate the adsorption of the adsorbate [127,128]. Hook, *et al.,* [127] investigated the adsorption behavior of a mussel adhesive protein (Mefp-1) on a gold surface using three techniques, specifically QCM,

ellipsometry, surface plasmon resonance (SPR), separately. They found that a much

larger mass uptake was measured by QCM compared to SPR and ellipsometry. With

further experiments using D_2O as the supporting electrolyte, the authors concluded that

the overestimation was because that the adsorption of Mefp-1 happened with a large

portion of trapped water, which formed into a hydrogel-like protein film. Macakova, *et

al.,* [128] studied the adsorption of didodecyltrimethylammonium bromide $(C_{12})_2$-DAB

(DDAB), the single-chained hexadecyltrimethylammonium bromide $C_{16}TAB$ (CTAB),

and dodecyltrimethylammonium bromide $C_{12}TAB$ (DTAB) on silica surfaces using QCM

together with atomic force microscopy (AFM). They also noticed a mass increase

associated with water trapped in the adsorbed films. However, Gutig, *et al.,* [126]

attributed this mass gain as a result of surface roughness, instead of trapped water. In

conclusion, the use of QCM to study the adsorptive behavior of inhibitor, while

promising, can also generate misleading results.

Atomic force microscopy (AFM) is another advanced technique to study the

surfaces with adsorbed molecules. It uses a physical probe to scan the surface at the

atomic level. AFM does not require any surface pretreatment and or the use of a vacuum

environment. Therefore, it has a wide applicability in both gas and liquid environment

and makes an excellent technique for studying the adsorption of inhibitors. Atkin, *et al.,*

[129] stated that the use of *in situ* AFM imaging is perhaps the greatest advance in the

investigation of the adsorption of surfactants at the solid-liquid interfaces in the last

decade. However, the use of AFM in the research of corrosion inhibitor adsorption is still

mostly limited to surface imaging. Solmaz, *et al.,* [81] investigated the surfaces of mild

steel exposed to HCl solution in the presence and absence of 2-MT using AFM

topography. They found that the addition of inhibitor formed a protective film on a mild

steel surface. Karlsson, *et al.,* [130] investigated the aluminium oxide surfaces with the

presence of two different inhibitors, sodium dodecyl sulfate (SDS) and sodium dodecyl

phosphate (SDP), using AFM imaging. They found that the adsorption of SDP was strong

while no apparent adsorption was noticed for SDS. It can be seen that AFM imaging only

provided a direct analytical support for the adsorption of inhibitors. More recently, Xiong,

et al., [131] investigated the films of a tall oil fatty acid (TOFA) imidazoline-type

inhibitor using an *in situ* AFM. The structure of the adsorbed inhibitor film was found to

be bilayer when the concentration was above the CMC. More importantly, they could

measure the normal force required to damage the film and pointed out that the shear

stress levels typically encountered in oil and gas applications were not likely responsible

for the removal of corrosion inhibitor films.

Although more attention has been paid to investigate the adsorption behavior of

inhibitors, plenty of unanswered questions remain. One of them is how to relate the

inhibition properties with its adsorption behavior. It is widely accepted that the inhibition

performance of inhibitor is closely related to the adsorption behavior, however, the

intrinsic connections are still not clear. The most significant example is whether it is

acceptable to simply equate coverage (θ) to inhibition efficiency (η).

Techniques Used for Inhibitor Characterization and Evaluation

As stated above, inhibitors are usually organic species and their structures are

temperature-sensitive. As a result, their molecular structure might change at elevated

temperatures and, hence, affect their performance as inhibitors. Moreover, in the application of corrosion inhibitors, reactions between inhibitor molecules and other chemical species in the system, their adsorption onto solid surfaces (parasitic consumption), and solubility changes could all affect inhibitor concentration. To maintain the facility integrity and operational safety, it is necessary to add more inhibitor when its concentration is depleted/low. Therefore, many techniques have been developed to accurately determine residual inhibitor concentrations, thus enabling their adjustment to appropriate, predefined values [58].

Current techniques used for evaluating corrosion inhibitors are mostly based on spectroscopic methods. Ultraviolet and visible (UV-vis) spectroscopy has the advantages of ease to operate and inexpensiveness. The robustness of this technique makes it routinely used in many laboratories. However, to strengthen the signals, the use of UV-vis usually requires the addition of dyes, most of which are toxic; this brings in safety concerns for the analyst [58]. Spectroscopic techniques have been used for analyzing the inhibitors of interest in the research reported in this dissertation. Martin and Valone [102] compared the UV spectra of a pure imidazoline-type inhibitor, a commercial amide (imidazoline precursor), an imidazoline-formulated inhibitor and an aged imidazoline-formulated inhibitor. They found that the imidazoline-formulated inhibitor consisted of both characteristic peaks of amide and imidazoline, suggesting the inhibitor contained both molecules.

Fourier transform infrared (FTIR) spectroscopy is also a rapid and precise technique that can be used to determine the composition of inhibitors. However, its

operation is usually for hydrocarbon phases and is less applicable to aqueous samples. Therefore, its usage is usually limited to quality control in the manufacture of imidazolines and amides. Martin and Valone also investigated the FTIR spectra of pure imidazoline, precursor amide, and commercial imidazoline relating to the inhibitor molecules. Again, the results confirmed that the commercial imidazoline-type inhibitor was a mixture of imidazoline and amide species.

Mass spectroscopy (MS) is a sensitive analytical tool capable of detecting molecules in the water phase. The use of MS is usually coupled with other techniques, such as liquid chromatography (LC) and electrospray ionization (ES). The sophisticated MS instrument usually requires advanced training for operation and spectral interpretation [58]. Gough and Langley [132] analyzed the quaternary ammonium and imidazoline corrosion inhibitor using electrospray mass spectroscopy (ES-MS) coupled with high-performance chromatography (HPLC). They found that the technique had the potential of quantifying both inhibitor residual concentrations in complicated production fluids.

NMR is also a powerful tool in determining the structures of the organic species. In Martin and Valone's work, they also studied the hydrolysis of imidazoline to amide using ^{13}C NMR. It was found that the molar ratio of imidazoline/amide decreased more than 20-fold in 20 days.

CHAPTER 3: OBJECTIVES AND HYPOTHESES

3.1 Research Objectives

According to the literature review, the performance of corrosion inhibitors can be affected by temperature in two ways: either by influencing the equilibrium of adsorption/desorption of inhibitor according to their specific adsorption mechanisms or by modifying ('degrading') the inhibitor molecular structures. It is also impossible to investigate the behavior of every single surface active molecule. Rather, a few candidate inhibitors (imidazoline-type and quat-type inhibitors) are selected based on their commonality and proven performance at low temperature.

Based on these considerations, two hypotheses are proposed:

- 1st hypothesis: As temperature increases, the desorption of the inhibitor is favored and the inhibitor efficiency is lost as long as the dominant adsorption mechanism is physisorption. In the case of chemisorption, the opposite behavior is expected.

- 2nd hypothesis: Inhibitor structure alterations due to thermal degradation are directly linked to the loss or gain of efficiency.

Based on these two different hypotheses, the main objectives of my research can be distilled down to two parts:

- 1st objective: Investigate the temperature effect on the adsorption/desorption behavior of the candidate inhibitors based on their adsorption mechanisms.

- 2nd objective: Study the effect of thermal stability of candidate inhibitors on their corrosion inhibition efficiency.

3.2   Research Strategy

The scope of work not only involves the investigation of adsorption behavior and corrosion inhibition performance of selected corrosion inhibitors, but also tackles the issue of their thermal stability in a wide range of temperature conditions from low (25°C) to high (150°C). The complex systematic study requires an explicit strategy. Therefore, a three-step research plan was established to address the objectives of the study:

- Step #1: The adsorption characteristics and inhibition performance of corrosion inhibitors at low temperatures will be established using QCM and electrochemical methods, at 25°C-80°C.

- Step #2: Inhibitors will be directly tested at higher temperature (80°C-150°C), without any pre-heat treatment. Their performance will be evaluated using electrochemical methods. Corrosion inhibition performance will be established and understood.

- Step #3: Corrosion inhibitor concentrations will be determined at different temperatures before and after experiments using spectroscopic methods. By checking if the structure of the inhibitor changed after experiments, the relationship between the thermal stability and the inhibition performance will be established.

The dissertation is organized in the same procedure. The adsorption behavior and inhibition properties of imidazoline-type inhibitor at 25°C-80°C are introduced in Chapter 4, followed by the high temperature (120°C-150°C) inhibition performance of the imidazoline-type inhibitor in Chapter 5. The role of the thermal stability of the

imidazoline-type inhibitor is discussed in Chapter 6. Similarly, the inhibition properties of the quat-type inhibitor at low temperatures and high temperatures are discussed in Chapter 4 and Chapter 5, respectively. The role of thermal stability of the quat-type inhibitor is described in Chapter 9.

3.3   Experimental Strategy

3.3.1 Summary of Techniques Used in This Study

Adsorption/desorption mechanisms are studied either by directly measuring mass change with the QCM techniques or interpreting LPR measurements. The kinetics and thermodynamics of the adsorption were evaluated. In addition, issues in QCM results interpretation were identified during the experimental campaign and are discussed in the next section. The inhibitor efficiency is assessed by performing corrosion tests in glass cell and autoclave experiments and measuring uninhibited and inhibited corrosion rates with LPR. Finally, inhibitor degradation is investigated by measuring the inhibitor concentration by UV-vis and the inhibitor composition by LC-MS and NMR. The experimental setups and methodologies are described in detail in each related chapter.

3.3.2 Significance of QCM Interpretation

Section 3.3.1 presented a brief summary of the QCM technique and how it has been used to measure adsorption of organic compounds. However, several issues arose during experimentation which made the interpretation of the results problematic. This section presents an effort to discuss the meaning of QCM measurements and justify how the results are presented.

The use of QCM to interpret the adsorptive behavior of inhibitors plays an important role in this project. Although it has shown promising use in the research of adsorption studies presented in the literature review, its interpretation can be problematic.

The most popular quartz crystal cut is the AT-cut (sliced at an angle of 35°15′ with respect to the x-axis) [133]. There are many advantages of the AT-cut crystal: firstly, it is capable of vibrating at a relatively high frequency, which ensures its ability to detect micro mass changes (nanogram level); secondly, it exhibits excellent stability in terms of frequency *vs.* temperature [134] (-25°C to 110°C in aqueous solution). This is also crucial for the current research which focuses on temperature effect. Last but not least, it can be obtained rather economically [133]. Therefore, the crystals used in the present research are all AT-cut crystals. For these crystals, the sensitivity factor in the Sauerbrey equation (Equation (25)), C_f, for a 5MHz crystal can be determined as:

$$C_f = 56.6 Hz \cdot \mu g^{-1} \cdot cm^2 \qquad (26)$$

As mentioned earlier, the Sauerbrey equation is used to convert the change in frequency of the crystals, directly measured with the QCM, into mass change (*i.e.*, mass adsorbed). However, the validity of the Sauerbrey equation is based on the assumption that the adsorbed film is rigid, evenly distributed, and thin [127]. Some of these assumptions might not be verified when applied to adsorption of inhibitor films in aqueous environments. As introduced earlier, Hook, *et al.,* [127] found that the adsorption mass of Mefp-1 measured by QCM was not 'real' mass, which was largely overestimated as a result of water molecules trapped in the adsorbed film. The damp adsorbed layers (hydrogel-like film) can cause a considerable energy dissipation, which

invalidates the use of the Sauerbrey equation for the conversion of frequency changes into mass adsorbed. Similarly, the mass changes measured in the current research, using the Sauerbery equation, clearly yielded inaccurate results. As an example, the adsorbed mass of imidazoline-type inhibitor calculated from the Sauerbrey equation was usually 4-6$\mu g \cdot cm^{-1}$. However, the mass of a single layer of imidazoline-type inhibitor, evaluated through the estimate molecule footprint, is around 0.22$\mu g \cdot cm^{-1}$, suggesting that there were 20-30 layers of corrosion inhibitor molecules adsorbed. The extremely high number of layers is most likely incorrect. The literature [105,135] indicates that the adsorption of imidazoline-type inhibitor is most likely through a bilayer-structure. In addition, the adsorption kinetics was found to follow the Langmuir adsorption model, which excludes the possibility of multi-layer development. Therefore, the adsorbed mass (Δm) of imidazoline-type inhibitor was most likely overestimated when calculated directly from the Sauerbrey equation.

Although the conversion from frequency change to mass adsorbed was found to be misleading, the use of frequency change (Δf) itself can still provide important kinetic information. Consequently, all QCM results presented in this dissertation are shown in terms of frequency change (Δf), instead of mass change (Δm).

CHAPTER 4: THE EFFECT OF TEMPERATURE ON THE ADSORPTION
BEHAVIOR AND INHIBITION PERFORMANCE OF AN IMIDAZOLINE-TYPE
INHIBITOR AT LOWER TEMPERATURES (25°C TO 80°C)

4.1   Introduction

Understanding the role of high temperature on the inhibition performance is a
complex task. First, many aspects of the tested system are affected by an increase in
temperatures and each of them must be taken into account. More importantly, any
attempt to investigate the role of high temperature also needs to be built upon existing
knowledge developed at lower temperature ranges.

In this chapter, the adsorption behavior of an imidazoline-type inhibitor was
investigated using a quartz crystal microbalance (QCM) at various temperatures (25°C,
50°C, and 80°C). The inhibition performance of the inhibitor was also evaluated using
electrochemical methods (LPR) in the same environments. In addition, a comparison
between the adsorption behavior and the inhibition performance was made to establish a
relationship between them.

4.2   Experimental

4.2.1 Equipment and Procedure

QCM Measurement

The adsorption behavior of the selected imidazoline-type inhibitor was studied
using a Stanford Research System (SRS) quartz crystal microbalance (Series No.
QCM200). The system consists of a controller, a crystal oscillator, a crystal holder, and a
gold-coated quartz crystal (total surface area of 4 cm^2, AT-cut, 5 MHz). The QCM
measurements were carried out in a glass cell, as shown in Figure 3. The electrolyte

generally consisted of 1 wt.% NaCl aqueous solution. CO_2 gas was sparged continuously

during the test to remove oxygen and maintain a constant CO_2 partial pressure. The

solution was stirred with a stir bar at a speed of 200 rpm to make the solution well mixed.

A temperature probe was used to monitor the temperature of the solution during these

tests. The solution pH was continuously recorded with a pH probe immersed in the

electrolyte. Once the solution had been purged for more than two hours and the desired

temperature had been achieved, the pH of the solution was adjusted to 4.0 by adding

deoxygenated diluted HCl or $NaHCO_3$ solution. The QCM holder was then immersed

into the test electrolyte and the mass recording was started. After each experiment, the

crystal was cleaned in isopropanol with ultra-sounding for 3 minutes.

QCM in glass cell	
1	Sample holder
2	Thermocouple
3	pH probe
4	Gas in
5	Gas out
6	Gold crystal
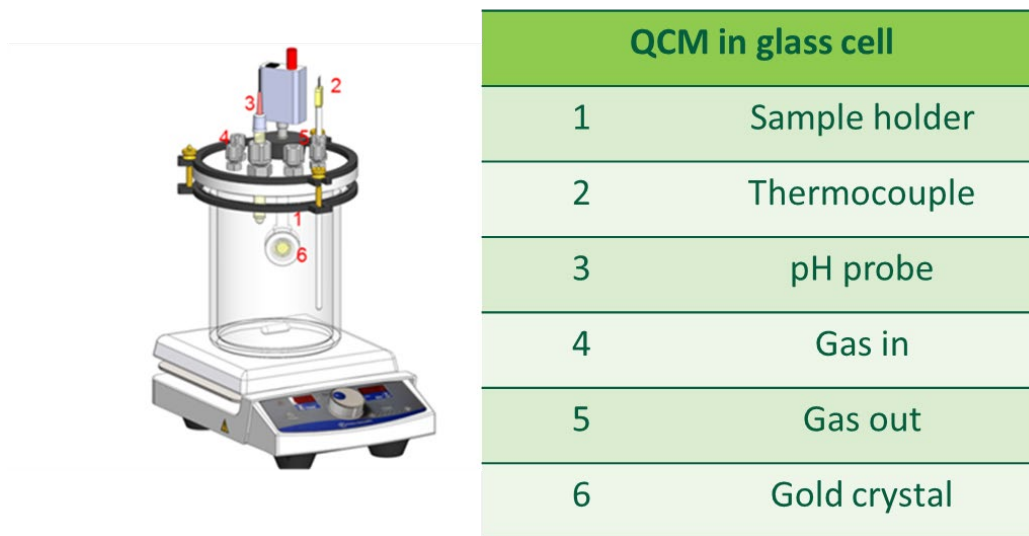
Figure 3. Configuration of a QCM in a glass cell (Courtesy of Cody Shafer)

Corrosion Measurement

The corrosion behavior of an API 5L X65 pipeline steel in the presence of different concentrations of inhibitors was investigated using electrochemical methods and surface analysis. The chemical composition of the API 5L X65 used in the present study is given in Table 3. The steel displayed a quenched and tempered microstructure. A typical three-electrode glass cell was used to study the inhibition performance of the corrosion inhibitor, as shown in Figure 4. The working electrode (WE) was a cylindrical electrode, 1.2 cm diameter by 1.4 cm in height. A platinum mesh was used as a counter electrode (CE). In addition, an external saturated silver/silver chloride (Ag/AgCl) electrode was used as a reference electrode (RE) via a Luggin capillary. The solution was also mixed using a stir bar at 200 rpm.

The electrolyte selected for the corrosion experiments was also a 1 wt.% NaCl aqueous solution, as for the QCM measurements. The test solution was continuously sparged with CO_2 to remove oxygen and maintain the partial pressure of CO_2 during the experiments. When the desired temperature was achieved, the pH of the solution was adjusted to 4.0 using diluted deoxygenated HCl or $NaHCO_3$. Before being inserted in the solution, the WE specimen was polished with 200 grit, 400 grit and 600 grit sandpaper, rinsed with alcohol and dried with N_2 as a routine procedure. In addition, two square specimens ($1.27 \times 1.27 \times 0.2$ cm) were used in each test for additional information, such as mass balance. The same procedure was applied to the specimens selected as the working electrode. Those specimens were immersed in the solution at the same time when the WE were immersed. During the tests, a deoxygenated and diluted HCl solution

was injected to maintain the solution pH which tended to increase, due to the ongoing corrosion process and release of corrosion products. The corrosion rate was monitored using linear polarization resistance. Polarization resistance measurements were performed from -5mV from the open-circuit potential (OCP) to +5mV from OCP at a scanning rate of 0.125mV/s. The B value for the corrosion rate determination is 23mV/decade. Initially, the corrosion rate before the injection of corrosion inhibitor was recorded as a baseline. Following inhibitor injection, the corrosion rate was monitored until it stabilized for more than 5 hours.

Table 3. Chemical composition (wt. %) of the API 5L X65

C	Mn	Si	Al	Cr	V	Mo	Ni	Fe
0.045	1.2	0.17	0.028	0.25	0.042	0.092	0.29	Balance

3 electrodes glass cell	
1	Working electrode
2	Counter electrode
3	Reference electrode
4	Gas bubbler
5	Thermocouple
6	Condensor

Figure 4. Configuration of the 3-electrode glass cell (figure courtesy of Cody Shafer)

4.2.2 Tested Inhibitor

The tested corrosion inhibitor was an imidazoline-type inhibitor. The effective ingredient is a tall oil fatty acid/dietheltriamine (TOFA/DETA) imidazoline. Its general structure is given in Figure 5. Here, it is worthy to note that the inhibitor is actually in its protonated form. That is because the imidazoline molecule has a strong tendency for protonation into imidazolinium in an acidic environment. Therefore, for the reason of accuracy, the inhibitor is named as 'imidazoline-type inhibitor'. In addition, the inhibitor itself has a limited water solubility and a high viscosity which make its use as a pure molecule rather impractical. Instead, it is introduced in a package of chemicals developed to increase its solubility in water and facilitate its transport to the metal substrate. The detailed information on the inhibitor package is given in Table 4.
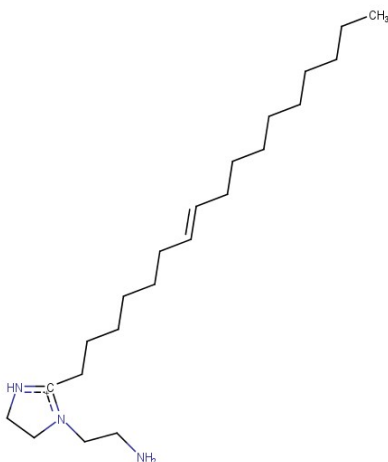
Figure 5. General structure of the TOFA/DETA imidazolinium

Table 4. Package information of imidazoline-type inhibitor

	TOFA/DETA imidazoline	Acetic acid	2-butoxyethanol	water
Percentage	24%	10%	13%	53%

4.2.3 Test Matrices

Experiments were carried out at various temperatures and concentrations. The test matrices of QCM measurements and corrosion measurements are given in Table 5 and Figure 6.

Table 5. Test matrix for QCM experiments of the imidazoline-type inhibitor

Description	Parameters		
Temperature/°C	25	50	80
Electrolyte	1 wt.% NaCl solution saturated with CO_2		
Inhibitor	Talloil fatty acid diethyltriamine imidazoline		
Inhibitor concentration/ppm	11/22/44/88		
Material	5MHz polished gold-coated crystal		
pH	4		
Stirring bar speed/rpm	200		

Table 6. Test matrix for corrosion measurements of the imidazoline-type inhibitor

Description	Parameters		
Temperature/°C	25	50	80
Electrolyte	1 wt.% NaCl solution saturated with CO_2		
Inhibitor	Talloil fatty acid diethyltriamine imidazoline		
Inhibitor concentration/ppm∗	22/44/88		
Material	API 5L X65		
pH	4		
Stirring bar speed/rpm	200		
Techniques applied	Linear polarization resistance(LPR), open circuit potential(OCP)		

∗*Here, if there is no special statement, the ppm is by volume for the rest of the document.*

4.3   Results and Discussion

4.3.1 Effect of Inhibitor Concentration on the Adsorption Behavior of the Imidazoline-Type Inhibitor

The adsorption behavior of the imidazoline-type inhibitor is shown in Figure 6. The frequency change is shown as $-\Delta f$ since it is negatively related to the mass uptake. It can be seen that without any inhibitor, the frequency change quickly stabilized after a few minutes of exposure – this curve is used as a baseline in the following. However, with the addition of inhibitor, the frequency started to decrease immediately and kept decreasing until a plateau was reached. The plateau suggests that the adsorption equilibrium was achieved. A significant observation in each dataset was the time required to attain this stable frequency. It is noteworthy that with a successive doubling of the concentration of inhibitor (11 ppm $\rightarrow$ 22 ppm $\rightarrow$ 44 ppm $\rightarrow$ 88 ppm), the time for reaching the adsorption equilibrium was approximately halved (85 min $\rightarrow$ 43 min $\rightarrow$ 25 min $\rightarrow$ 20 min). This observation indicates that adsorption rate was related to the concentration of corrosion inhibitor.
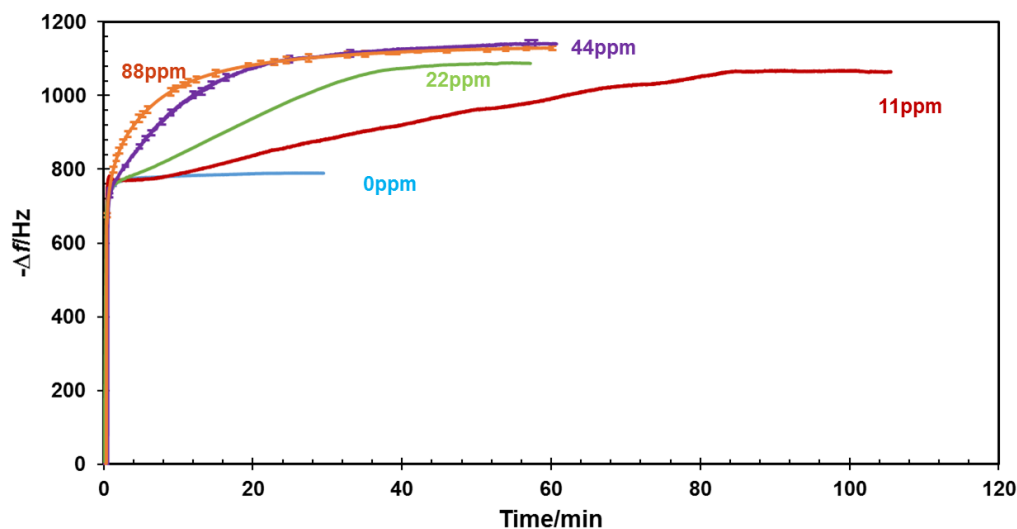
Figure 6. Adsorption of the imidazoline-type inhibitor at 25°C with the presence of different amount of inhibitor. (1wt.% NaCl, pH=4.0, p_{CO2}=0.97 bar; 200 rpm, 5 Mhz polished gold-coated crystal)

The trend in frequency change of the imidazoline-type inhibitor over time at 50°C is given in Figure 7. The adsorption rate increased with increasing concentration, similarly to what was observed at 25°C.

The frequency change of the imidazoline-type inhibitor over time at 80°C is given in Figure 8. Similar trends were observed at 80°C as at 25°C and 50°C. At 80°C, the results obtained with 11 ppm of inhibitor are not shown due to a failure of the quartz crystal during the test.

It is important to mention that all of these results were obtained using the same crystal. Attempts to repeat these results with a different crystal proved problematic as the adsorption behavior at the same condition was quite different in terms of frequency change value.
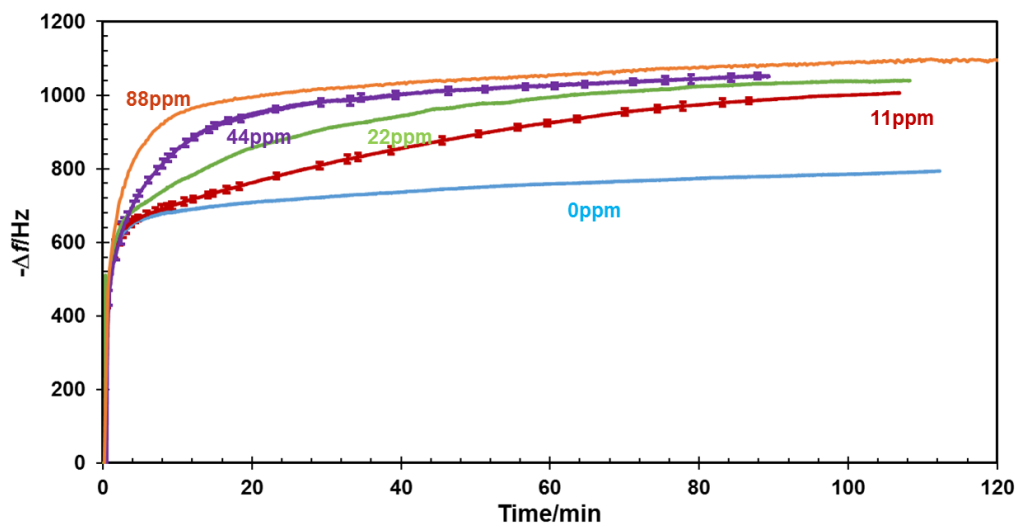
Figure 7. Adsorption of the imidazoline-type inhibitor at 50°C with the presence of different amount of inhibitor. (1wt.% NaCl, pH=4.0, p_{CO2}=0.97 bar; 200 rpm, 5 MHz polished gold-coated crystal)
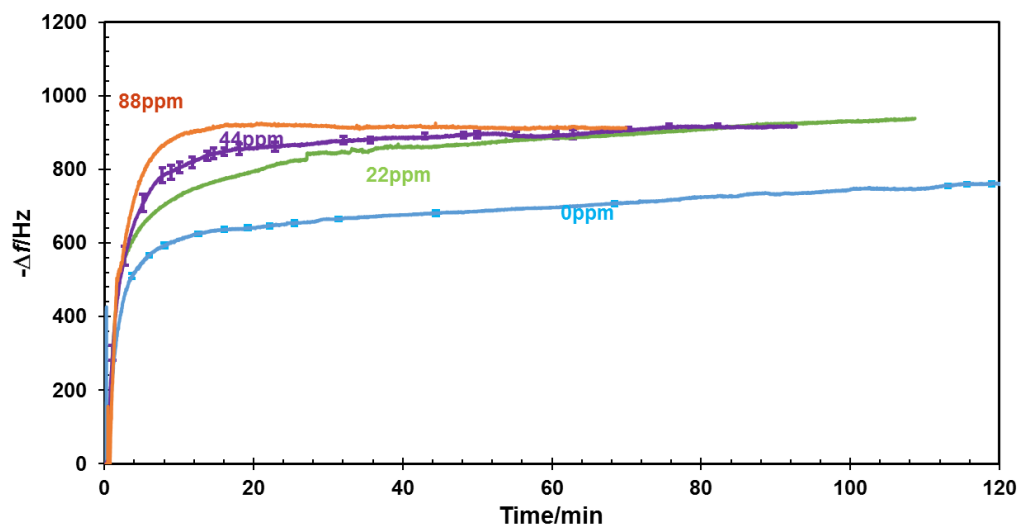
Figure 8. Adsorption of the imidazoline-type inhibitor at 80°C with the presence of different amount inhibitor. (1wt.% NaCl, pH=4.0, p_{CO2}=0.97 bar; 200 rpm, 5 MHz polished gold-coated crystal)

4.3.2 Effect of Temperature on Adsorption Thermodynamics and Kinetics

In this section, the role of temperature on adsorption thermodynamics and kinetics is discussed in more details. However, before introducing how temperature affects the adsorption behavior of the imidazoline-type inhibitor, it is necessary to find a way to quantify the adsorption kinetics and thermodynamics. Generally, an adsorption isotherm model is adapted to interpret the adsorption behavior. Several adsorption models have been described for the adsorption of corrosion inhibitors and can be found in Table 7.

Table 7. Adsorption models and their characteristics [65]

Isotherms	Description
Langmuir adsorption	Only considers fundamental adsorption/desorption steps
Frumkin adsorption	Considers the adsorption/desorption steps and the interactions among adsorbed inhibitor molecules
Temkin adsorption	Considers a heterogeneous surface
Flory-Huggins adsorption	Considers the substitution of adsorbed solvent by adsorbing molecules

In this work, the Langmuir adsorption model was chosen as a starting point as it is the simplest. Langmuir adsorption only considers fundamental adsorption steps and neglects other factors such as interactions between molecules. Key aspects of the Langmuir adsorption model can be described as follows [71,136].

The adsorption of the inhibitor consists of a reversible reaction;

Forward reaction:

$$inhibitor(bulk) \xrightarrow{adsorption} inhibitor(surface) \qquad (27)$$
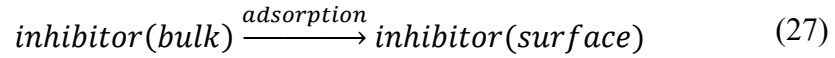
Forward reaction rate:

$$\vec{r} = k_a(1 - \theta)c \qquad (28)$$

Backward reaction:

$$inhibitor(surface) \xrightarrow{desorption} inhibitor(bulk) \qquad (29)$$
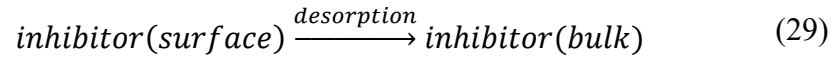
Backward reaction rate:

$$\overleftarrow{r} = k_d\theta \qquad (30)$$

Net reaction rate:

$$\frac{d\theta}{dt} = \vec{r} - \overleftarrow{r} = k_a(1 - \theta)c - k_d\theta \qquad (31)$$

where, θ is a parameter commonly defined as the surface coverage of the inhibitor

(unitless), k_a is the adsorption rate constant (h^{-1}), k_d is the desorption rate constant

(mol·L^{-1}·h^{-1}) and c is the inhibitor concentration (mol/L).

Equation (31) is a first order differential equation, which can be integrated into

$$\theta(t) = K_1[1 - \exp(-K_2 t)] \qquad (32)$$

Where:

$$K_1 = \frac{c}{(c + \frac{k_d}{k_a})}, K_2 = k_a c + k_d \qquad (33)$$

The kinetic form of Langmuir adsorption can be determined as Equation (32).

Therefore, if the relationship between coverage (θ) and time (t) is known, kinetic

parameters such as k_a and k_d can be determined.

On the other hand, the thermodynamic side of the Langmuir adsorption model can be expressed as follows:

When at equilibrium, $d\theta/dt = 0$,

$$\theta = \frac{k_a c}{k_a c + k_d} \tag{34}$$

In another form:

$$\frac{k_a}{k_d} = \frac{\theta}{1 - \theta} c = K_{eq} \tag{35}$$

From the basics of reaction thermodynamics:

$$\Delta G_{ads} = -RT_k \ln K_{eq} \tag{36}$$

where, K_{eq} is equilibrium constant (mol·L^{-1}), and ΔG_{ads} is adsorption Gibbs energy (kJ·mol^{-1}), which indicates the spontaneity of the adsorption reaction. Equation (36) shows a critical relationship between temperature and adsorption behavior. As for any reversible reaction, the equilibrium shifts as temperature changes.

These kinetic and thermodynamic parameters presented in the Langmuir model can be obtained by fitting of experimental results. However, the coverage (θ) needs to be determined before any fitting exercise is performed. The determination of coverage is rather critical in the simulation of adsorption models. θ is the factor that connects the whole kinetic and thermodynamic aspects of Langmuir adsorption model, as it can be found in Equations (28), (30), (31), (32), (34), (35).

To determine the coverage, the notion of frequency at equilibrium (-$\Delta f_{equilibrium}$) is needed and discussed in this section. -$\Delta f_{equilibrium}$ is the frequency change generated by the adsorption of inhibitor at equilibrium on the gold-coated quartz crystal. Since the mass

measured by QCM includes both inhibitor and water baseline, the equilibrium frequency

can be calculated from the difference between the frequency at equilibrium and the

baseline mass (frequency when no inhibitor is present, 780Hz). Figure 9 shows that the -

$\Delta f_{equilibrium}$ generally increases with increasing concentration of inhibitor. For example, at

50°C, the frequency change (-$\Delta f_{equilibrium}$) increased from 198Hz with the presence of 11

ppm corrosion inhibitor to 283Hz with 88 ppm inhibitor. This agrees with the adsorption

thermodynamics. According to Equation (35), when the inhibitor concentration increases,

K_{eq} does not change because k_a and k_d do not change at a fixed temperature. As a result,

the coverage θ is supposed to increase. In other words, more inhibitor is adsorbed at the

crystal surface at equilibrium. Another important finding is that with the same

concentration of inhibitor, the equilibrium frequency change decreases with temperatures.

This suggests that the equilibrium of adsorption/desorption favors desorption at elevated

temperatures. Here, it is important to point out that the repeatability of the set of

experiments is good. The errors between repeated experiments is usually less than ±5Hz.

Therefore, the error bars in each case are very small and the results of the experiments are

reliable.

However, at 25°C, when the inhibitor concentration doubled from 44 ppm to 88

ppm, -$\Delta f_{equilibrium}$ remained stable or only slightly decreased from 350Hz to 340Hz. The

phenomenon indicates that the crystal surface may have been already fully covered by the

imidazoline-type inhibitor molecules with the 44ppm corrosion inhibitor in solution at

25°C. Therefore, even when the inhibitor concentration was doubled, the frequency

change did not measurably increase. In conclusion, the maximum equilibrium frequency

$(-\Delta f_{\text{equilibrium, max}})$ caused by the adsorption of inhibitor $(-\Delta m_{\text{equilibrium, max}})$ on the gold-coated crystal was estimated to be at 350Hz (25°C, 44ppm imidazoline-type inhibitor). For a known frequency change, 'coverage' can be determined at any time as:

$$\theta^* = \frac{\Delta m}{\Delta m_{equilibrium,max}} = \frac{-C_f \cdot \Delta f}{-C_f \cdot \Delta f_{equilibrium,max}} = \frac{-\Delta f}{-\Delta f_{equilibrium,max}} \tag{37}$$

Here, Δm is the mass adsorbed at any tested time, Δf is the frequency change measure by QCM at any tested time. Note that the term 'coverage', although widely used in the literature, only refers to the ratio of the frequency change to maximum equilibrium frequency change of the crystal. However, the definition of coverage is that the ratio of the area covered by inhibitor and the total area. There are some subtle differences between the two definitions. For example, the frequency change could only indicate how much inhibitor is adsorbed, it cannot describe how the inhibitor molecules adsorbed. In fact, the molecules can exhibit a structure of single, double or multiple layers. Therefore, the increase in frequency change (*i.e.*, amount of inhibitor adsorbed) might not necessary lead to an increase in coverage if there are multiple layers. In summary, the 'coverage' defined by the ratio of frequency change (related to the adsorbed mass) and maximum equilibrium frequency change (related to the maximum equilibrium adsorbed mass) is not genuine coverage. However, it certainly is closely related to the coverage and therefore the symbol used here is 'θ^*'.
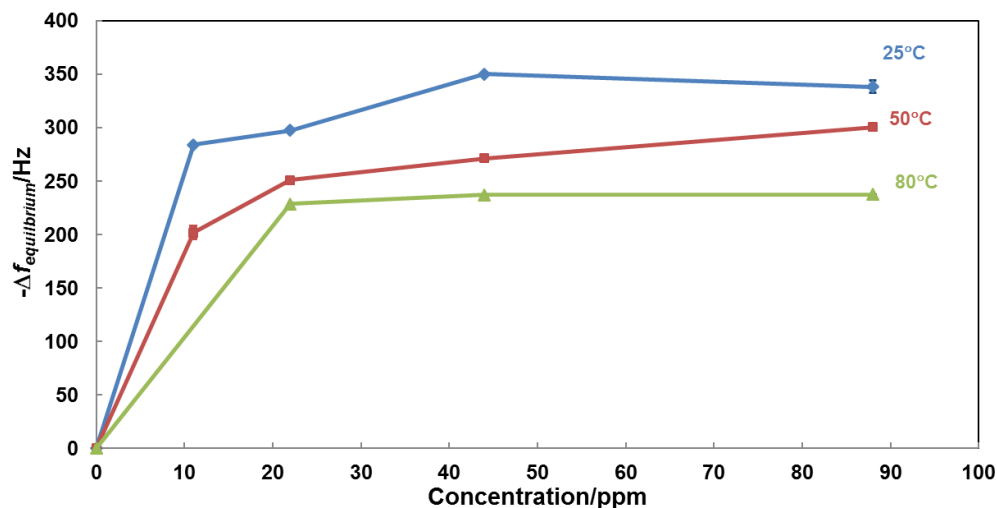
Figure 9. Equilibrium frequency *vs.* inhibitor concentration (1 wt.% NaCl, 200 rpm, p_{total}=1 bar; 5 MHz polished gold-coated crystal)

The determination of θ^* can help reveal important information about the kinetics of adsorption using Equation (32) and Equation (33). All experimental results were fitted with the Langmuir kinetic process using the least square method. The fitted results are listed in Table 8. The R^2 in the table is the statistical measurement of how close the data are to the fitted line: a good fit is obtained when the value of R^2 is close to 1. From the table, it can be seen that in most conditions, R^2 is higher than 0.95, which means that the experimental coverage *vs.* time curve shows good agreement with the Langmuir adsorption process. This also suggests that the adsorption of the imidazoline-type inhibitor generally follows the Langmuir model.

Table 8. Fitting results of Langmuir adsorption model using QCM measurements

Temperature/°C	Inhibitor concentration/ppm	K_1	K_2	R^2
25	22	0.9	2.54	0.9
	44	1	4.61	0.99
	88	0.94	7.5	0.99
50	22	0.73	2.45	0.99
	44	0.76	6.07	0.99
	88	0.83	12.31	0.99
80	22	0.64	4.81	0.98
	44	0.66	14.37	0.98
	88	0.84	18.27	0.95

Here, the excellent agreement with Langmuir adsorption model also inferes that non-specific adsorption should not affect significantly the measured frequency. Non-specific adsorption is the adsorption that occurs in the long-range (contrary to the specific adsorption that happens in the inner layer or directly with the surface) [127]. Some researchers assumed that the measured mass with QCM might be over-estimated because it can include non-specific adsorption [125, 126]. However, it is not likely it played a role in the adsorption of the imidazoline-type inhibitor. Assuming that non-specific adsorption took place, the adsorption kinetics should include not only the specific adsorption of molecules but also the non-specific process. Owing to the different interacting forces, the specific and the non-specific adsorption kinetics should undergo different kinetics. However, the high R^2 value in Table 8 suggests that the simple Langmuir adsorption model, which is only used for description of specific adsorption [65], is enough to

represent the adsorption process. Therefore, non-specific adsorption is presumably not occurring significantly in the measured mass with QCM. In addition, kinetic parameters can be calculated using Equation (33) from the obtained K_1 and K_2 values in Table 8. Corresponding calculated k_a and k_d values are listed in Table 9.

Table 9. Calculated adsorption rate constants of the adsorption of the imidazoline-type inhibitor

Temperature/°C	Inhibitor concentration/ppm	Adsorption rate constant k_a/ $10^5 \cdot h^{-1}$	Adsorption rate constant k_d/ $mol \cdot L^{-1} \cdot h^{-1}$
	22	-	-
25	44	4.37	0
	88	3.34	0.42
	22	3.37	0.67
50	44	4.38	1.44
	88	4.86	2.03
	22	5.87	1.72
80	44	8.99	4.87
	88	7.28	2.89

To further illustrate the change of adsorption parameters, the logarithmic change of the change of k_a and k_d with temperature is plotted in Figure 10. It is clear that both reaction rate constants increase with temperature. The fundamental equation of reaction kinetics can be expressed as:

$$k = A exp(-\frac{E_{(activation)}}{RT_k}) \qquad\qquad (38)$$

where, k is reaction rate constant, E_a is reaction activation energy in kJ·mol^{-1}, T_k is

temperature in Kelvin, R is the gas constant (8.314 J·mol^{-1}) and A is a pre-exponential

constant. According to this equation, a linear relationship should be obtained between

$\ln(k)$ and $1/T_k$ because of the logarithmic relationship between k and T_k. This linear

relationship is shown in Figure 10, as indicated by the black trend line. It can further be

used to determine the activation energies of the adsorption and desorption reactions.

Therefore, E_a (adsorption reaction activation energy) and E_d (desorption reaction

activation energy) were calculated as 10.25 kJ·mol^{-1} and 21.4 kJ·mol^{-1} based on Equation

(12). Error bars are taken from k_a and k_d measured with different concentrations of

inhibitors at the same temperatures.
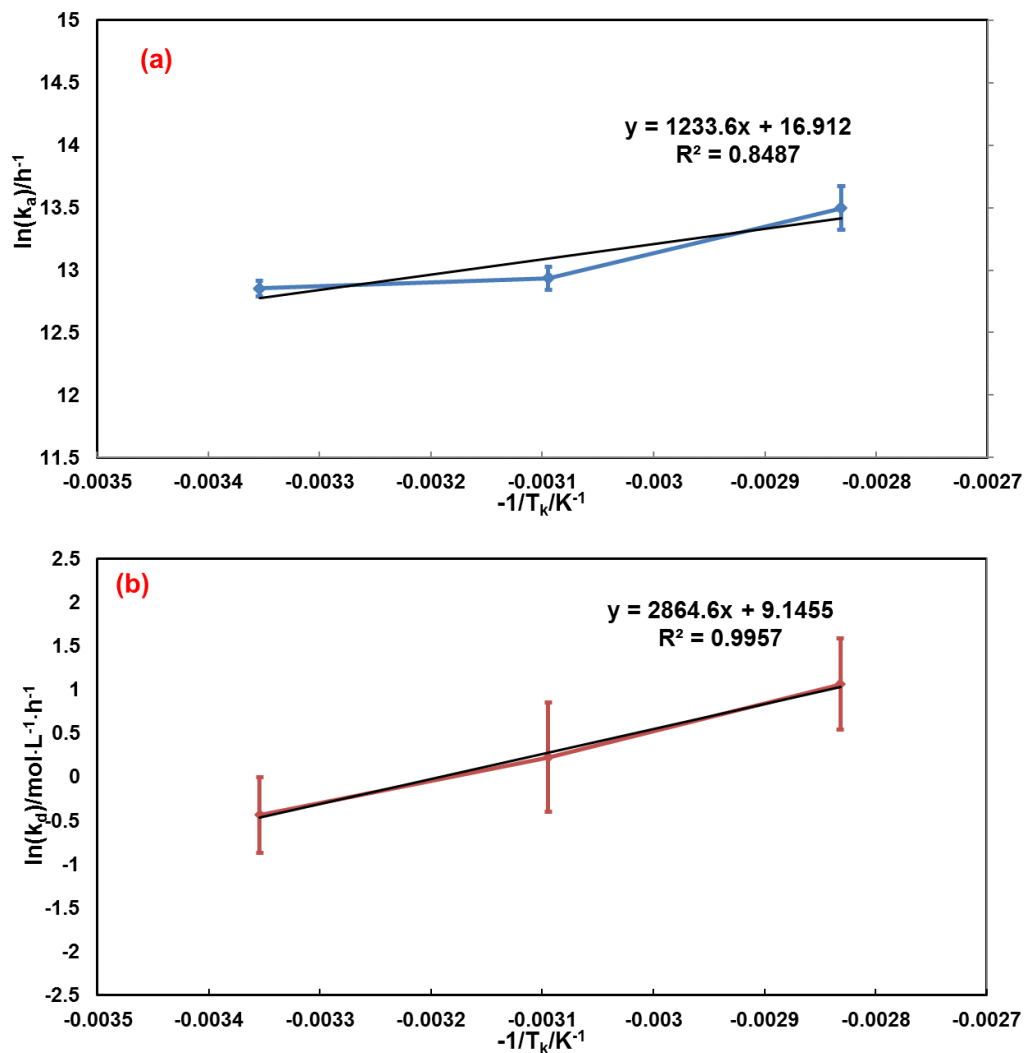
Figure 10. Temperature dependence of rate constant k_a and k_d of the imidazoline-type inhibitor adsorption. (a). $\ln(k_a)$ vs. $-1/T_k$ (b). $\ln(k_d)$ vs. $-1/T_k$

Error bars are taken from ka and kd measured with different concentrations of inhibitors at the same temperatures, as shown in Table 9.

Although it is found that both k_a and k_d increase with temperature, their dependence on temperature is not the same. As shown in Figure 11, the ratio of k_d/k_a increases with temperature, which suggests that k_d increases faster than k_a with

temperature. This in turn yields a reduction in surface coverage when equilibrium is reached. In addition, Gibbs energy of adsorption can be calculated since both kinetic rate constants are obtained. The standard Gibbs energy ΔG°_{ads} is then calculated as $-33.7 kJ \cdot mol^{-1}$.
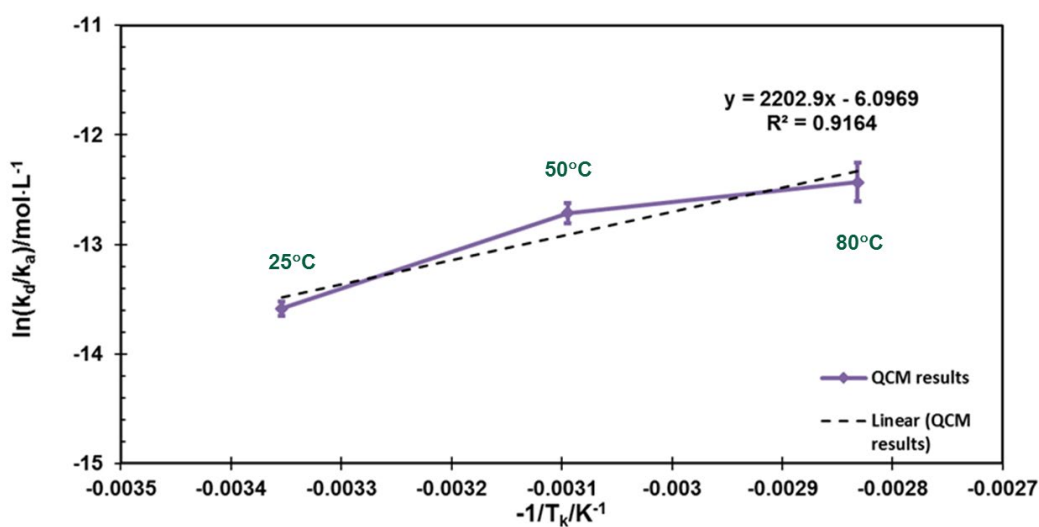
Figure 11. Temperature dependence of k_d/k_a

Error bars represents the k_a/k_d calculated from different concentration at the same temperatures.

4.3.3 Effect of Inhibitor Concentration on the Corrosion Inhibition Performance

In the last section, it is concluded that desorption of inhibitor seemed to be favored at higher temperatures. The effect of temperature on the corrosion inhibition performance is examined in this section. It is widely accepted that the adsorption of inhibitor is critical to its inhibition performance, however, how these two concepts actually relate to each other is not quite clear. Therefore, additional experiments were performed considering corroding samples at different temperatures. These could

theoretically be performed using a QCM equipped with iron-coated crystals. However, this technique would not be appropriate in this study since mass gain due to inhibitor adsorption would occur simultaneously with mass loss due to corrosion. For example, the adsorbed inhibitor mass is typically of the order of the $\mu g \cdot cm^{-2}$ level, however, the mass loss due to iron dissolution could easily be up to $mg \cdot cm^{-2}$. Therefore, the adsorption information can be easily compromised due to the corroding of iron. Instead, the experiments were performed in a typical electrochemical cell with the cylindrical X65 working electrode as the corroding surface.

In general, the corrosion rate started at a fairly high value and decreased quickly with time with the injection of inhibitor. It usually reached a steady-state value within 3 to 4 hours, depending on temperature. In comparison, QCM results clearly showed a similar behavior but the steady state was achieved within only one hour. This discrepancy can be attributed to the effect of corrosion on the substrate metal which undermines the adsorption phenomenon.

At 25°C, the corrosion rates dropped from 2 to 0.12, 0.11, and 0.10 mm/y with the addition of 22 ppm, 44 ppm and 88 ppm inhibitor, respectively (Figure 12). The low corrosion rate is an indication of successful corrosion inhibition. However, at 50°C (Figure 13), with the presence of 22 ppm imidazoline-type inhibitor, corrosion rates were still high (2.5 mm/y compared to a baseline of 4 mm/y). Nevertheless, with higher amounts of inhibitor, the corrosion rate dropped to 0.6 (44ppm) and 0.4 mm/y (88ppm). Clearly, higher concentrations of inhibitor are needed to provide adequate protection against corrosion at higher temperatures.
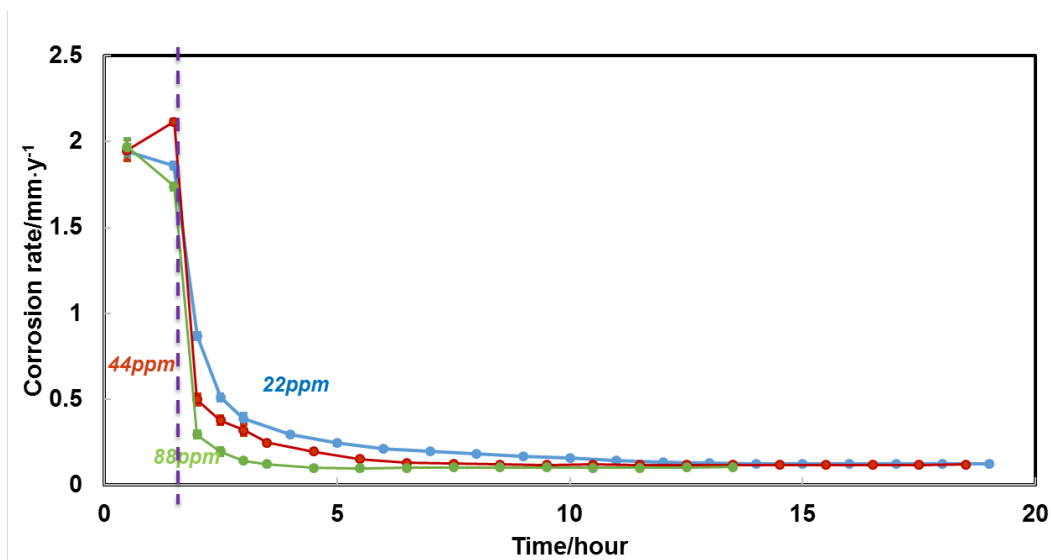
Figure 12. Corrosion rate at 25°C with the addition of different concentrations of the imidazoline-type inhibitor (1 wt.% NaCl, p_{CO_2} (partial pressure of CO_2) is 0.97bar, pH=4.0;200 rpm). Purple line indicates when the inhibitor was injected.
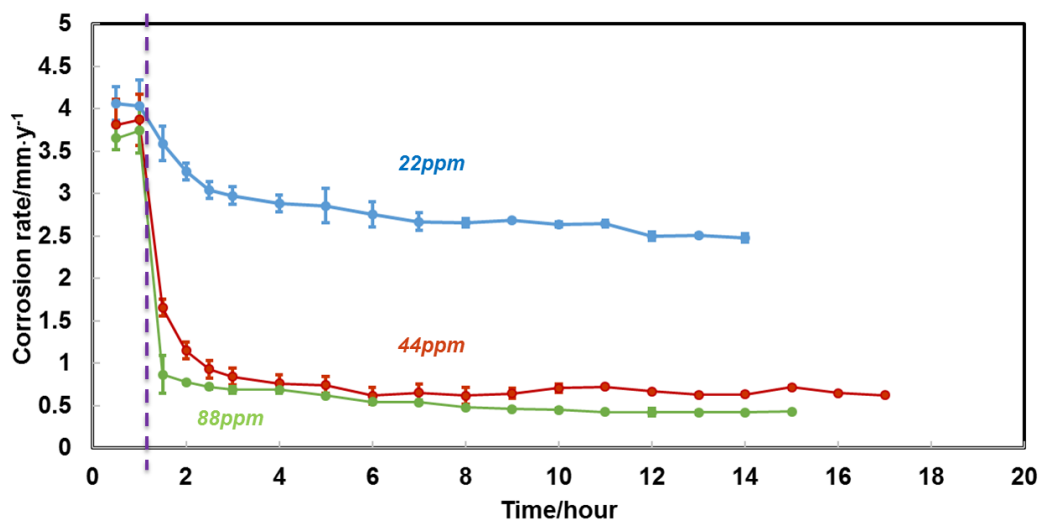
Figure 13. Corrosion rate at 50°C with the addition of different concentrations of the imidazoline-type inhibitor (1 wt.% NaCl, p_{CO_2} is 0.8bar, pH=4.0;200 rpm). Purple line indicates when the inhibitor was injected.

It was more difficult to obtain a stable corrosion rate at 80°C (Figure 14).

Corrosion rate even increased to 7 mm/y with 22 ppm corrosion inhibitor. An 'inhibited'

corrosion rate of 2 mm/y was obtained at the end of the experiment with 44 ppm of

inhibitor, which was still high and not considered to be successful inhibition. Moreover,

unexpected results were observed with 88 ppm corrosion inhibitor. At first, the corrosion

rate seemed to decrease to as low as 0.2mm/y after 24 hours. However, significant

localized corrosion areas were observed on the corroded sample surface after examining

the weight loss specimen used in this experiment. To confirm the occurrence of localized

corrosion, another square specimen was tested in the same conditions. Again, a large

localized corrosion area was identified and characterized using a profilometer as shown

in Figure 15. This localized corrosion feature had a flat bottom and covered a large part

of the specimen surface (6 mm long on a 12 x 12 mm specimen). In addition, the depth of

this attack was about 100 μm in 24 hours leading to a rate of 36.5 mm/y localized

corrosion, which was 7 to 8 times higher than the general corrosion rate (4.7 mm/y)

without corrosion inhibition. Obviously, the low corrosion rate obtained with LPR (0.2

mm/y) was not representative of the localized corrosion. Usually, the occurrence of

localized corrosion is a result of insufficient corrosion inhibition [113,114,137].

Therefore, a higher concentration of inhibitor was introduced to confirm whether it is

caused by lack of inhibitor. It was found that the localized corrosion was mitigated with a

higher concentration of corrosion inhibitor. In the experiment with 176 ppm corrosion

inhibitor in the solution, no localized corrosion was observed and the corrosion rate was

only 0.26 mm/y after 24 hours (Figure 14). From the discussion, it can be seen that the

inhibition performance was significantly limited by higher temperatures.
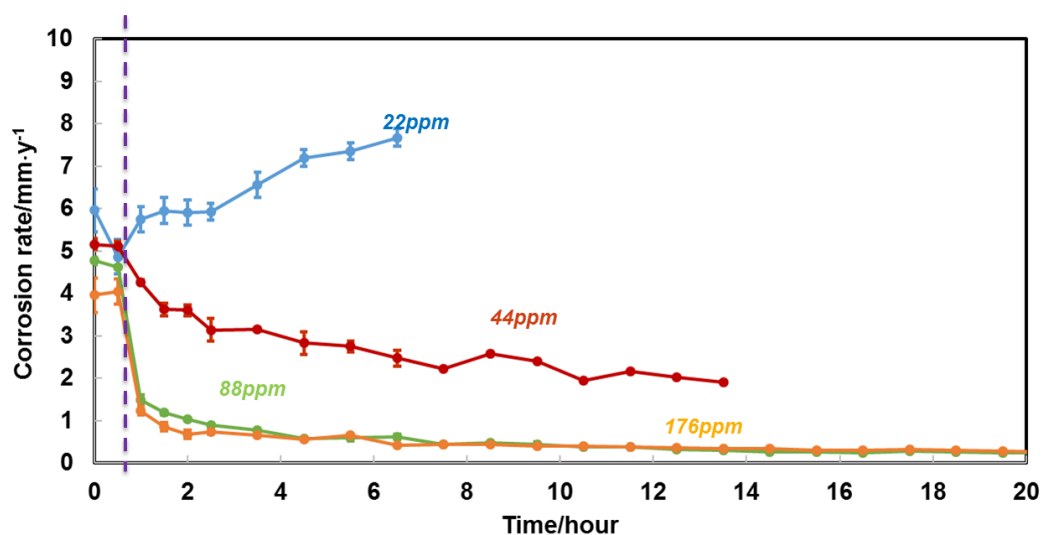
Figure 14. Corrosion rate at 80°C with the addition of different concentrations of the imidazoline-type inhibitor (1 wt.% NaCl, p_{CO2}=0.5bar, pH=4.0;200 rpm). Purple line indicates when the inhibitor was injected.

∗ Error bars in each cases represents the repeated experiment with the same conditions.
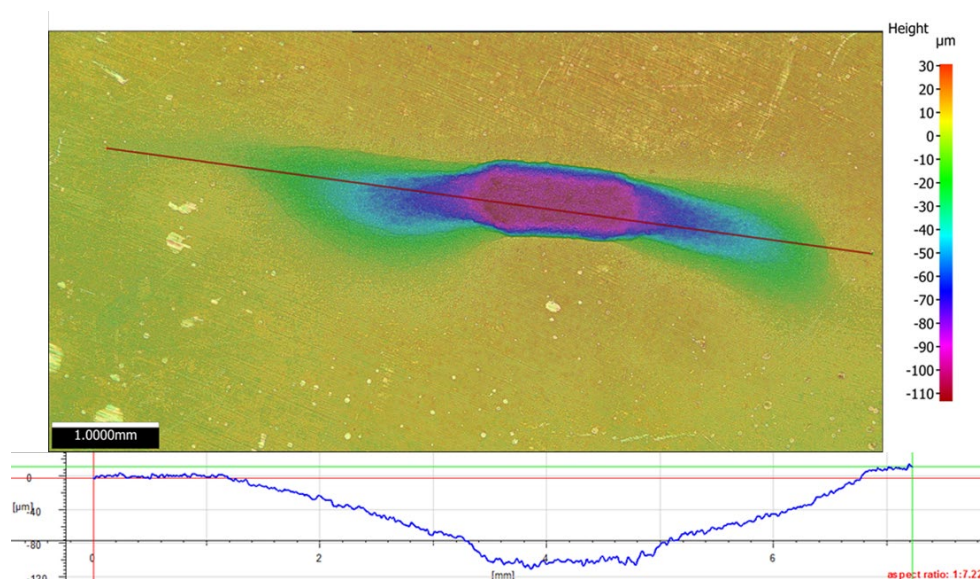
Figure 15. Surface profilometry of localized attack at 80°C (1 wt.% NaCl, p_{CO2}=0.5bar, pH=4.0;200 rpm, with 88ppm imidazoline-type inhibitor). Surface profilometry was obtained on a square sample. Test lasted for 24hours.

The measured inhibited corrosion efficiencies are summarized in Table 10. η represents the inhibition efficiency and is calculated through Equation (23). It can be seen that inhibition efficiency usually increases with increasing concentration of corrosion inhibitor at a constant temperature. For example, inhibition efficiency increased from 38%→82%→89% with 22 ppm, 44 ppm, 88 ppm corrosion inhibitor at 50°C, respectively. In addition, the inhibition efficiency decreases with temperature. Inhibition efficiency decreased from 95%→82%→60% with 44 ppm corrosion inhibitor at 25°C, 50°C and 80°C, respectively. The observed pattern is similar to that obtained for the adsorption study on an inert gold substrate. It was also observed that the θ*increases with inhibitor concentration at the same temperature and decreases with temperature at a fixed

inhibitor concentration. This similarity confirms that coverage obtained from corrosion inhibition efficiency is closely related to adsorption behavior.

Table 10. Inhibition test results of the imidazoline-type inhibitor from 25°C to 80°C

Temperature /°C	Inhibitor concentration/ppm	Initial corrosion rate/ mm·y^{-1}	Final corrosion rate/ mm·y^{-1}	Localized corrosion	Inhibition efficiency(η)
25	22	1.9	0.12	No	93%
	44	1.9	0.11	No	95%
	88	1.7	0.1	No	94%
50	22	4	2.5	No	38%
	44	3.9	0.6	No	82%
	88	4	0.4	No	89%
80	22	4.8	7.7	No	-
	44	4.9	2	No	60%
	88	4.7	0.2	Yes	-
	176	4.2	0.4	No	93%

Here, '-' suggests that the inhibition efficiency is not available. The reason could be there was no inhibited corrosion rate or LPR results did not represent localized corrosion.

4.3.4 Discussion on the Relationship between the Adsorption Behavior and Inhibition Performance of Corrosion Inhibitor

In the last section, a similarity was found between the adsorption behavior and the inhibition performance of the imidazoline-type inhibitor. In this section, the connection between the two different aspects of inhibitor is discussed in-depth. The analysis of the

QCM results showed that the adsorption of the imidazoline-type inhibitor generally follows the Langmuir adsorption process. Similarly, the $\boldsymbol{\eta}$ *vs.* time relationship obtained from the corrosion inhibition experiments can be fitted with Langmuir adsorption process to determine whether the corrosion efficiency follows a similar trend. In the QCM tests, θ^* was determined by the ratio of the steady-state frequency change (related to the mass absorbed) to the maximum steady state frequency change (maximum steady state mass absorbed) (Equation (37)). In most cases, the $\boldsymbol{\eta}$ *vs.* time relation showed acceptable fitting results ($R^2 > 0.98$) (see Table 11). Assuming that θ^* is closely related to the inhibition efficiency ($\boldsymbol{\eta}$) ($\theta \approx \boldsymbol{\eta}$), the thermodynamic parameter k_d/k_a can be first determined using steady-state inhibition efficiency *via* Equation (9). The obtained k_d/k_a can be then compared with the k_d/k_a value calculated from QCM results, as shown in Figure 16. Here, cases with poor R^2 were not used in this comparison – they corresponded to cases with localized corrosion. The obtained results from the two different sets of experiments, nevertheless, are almost the same. This observation shows that evaluating the surface coverage *via* ratio of frequency change (related to mass adsorbed) or *via* corrosion efficiency yields similar outcome in term of equilibrium adsorption constants at temperatures from 25°C to 80°C. Therefore, it can be concluded that the term 'inhibition efficiency' has a closely related relationship with the quantity of absorbed inhibitor, defined as 'coverage'. One more important fact is that the testing materials are completely different: QCM measurements were on gold-coated crystals and corrosion inhibition tests were performed with mild steel specimens. This might suggest that the substrate metal is not critical to the thermodynamics of adsorption of inhibitor, at least in

the conditions selected for this study. However, the effect of the substrate on the kinetics of adsorption maybe more pronounced – this is explored in the next section.

Table 11. Fitting results of Langmuir adsorption model using inhibition results

Temperature/°C	Inhibitor concentration/ppm	K_1	K_2	R^2
25	22	0.914	1.58	0.99
	44	0.93	3.24	0.98
	88	0.94	3.24	0.99
50	22	-	-	-
	44	0.83	2.12	0.99
	88	0.87	3.43	0.99
80	22	-	-	-
	44	-	-	-
	88	-	-	-
	176	0.91	2.89	0.99

Here, '-' suggests that the fitting results is not available. The reason could be there was no inhibited corrosion rate or LPR results did not represent localized corrosion.
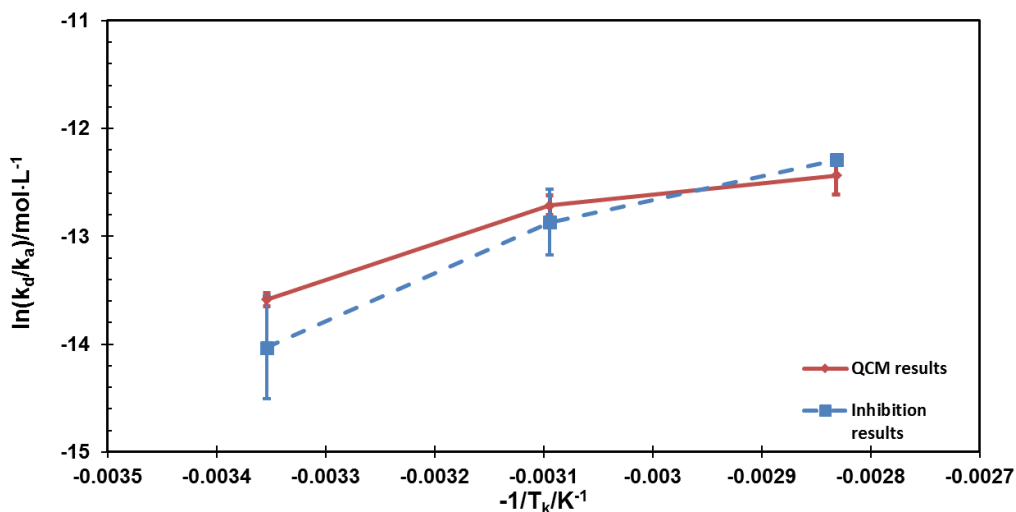
Figure 16. Comparison of temperature dependence of k_d/k_a obtained from QCM and inhibition tests.

Although the thermodynamic ratio k_a/k_d obtained either through corrosion inhibition or QCM tests is comparable, the actual values of kinetic constants were significantly different between the two test methods. One possible explanation for the differences in the kinetic aspect is that there is iron dissolution occurring at the same time of the adsorption of corrosion inhibitor. In Equation (31), the net adsorption rate consists only two parts: the adsorption reaction from bulk to surface and the desorption reaction from surface to bulk. This is valid for an inert surface such as gold or platinum. However, Drazic, *et al.*, [110] suggested that for a reactive surface, such as an iron surface, the absorbed inhibitor molecules might be mechanically removed due to the underlying dissolution of the substrate. As a result, the dissolution of the substrate iron can be considered as another component of the overall desorption reaction. It was named 'electromechanical' desorption by the authors [110]. This additional reaction must be

proportionally related to the rate of iron dissolution. By adding this extra component into

Equation (31), a more realistic Langmuir adsorption model can be proposed as:

$$\frac{d\theta}{dt} = \vec{r} - \overleftarrow{r_1} - \overleftarrow{r_2} = k_a(1-\theta)c - k_d\theta - k_3j\theta \qquad (39)$$

When reached at equilibrium, dθ/dt=0:

$$\theta = \frac{k_a c}{k_a c + k_d + k_3 j} \qquad (40)$$

where, k_3 could be considered as rate constant for the electrochemical desorption reaction

(no specific unit), j is corrosion current (A·cm^{-2}) without inhibition (or corrosion rate).

The use of this more comprehensive model can clarify some aspects of the

phenomena observed in the corrosion tests. On the one hand, it might answer the question

of why there is no 100% corrosion efficiency. The corrosion inhibition test results (Table

10) show that although higher concentration of inhibitor lead to higher efficiency, 100%

protection is never achieved. This is due obviously to the inhibitor desorption reaction

(expressed through k_d) but also to the iron dissolution or electrochemical desorption

reaction, expressed through k_d and k_3j, respectively, in Equation (40). On the other hand,

it points out that the iron dissolution rate is also very important to the corrosion inhibition

efficiency. Note that in Table 10, at higher temperatures (50°C and 80°C) where the

uninhibited corrosion rates are the highest, low concentrations of inhibitor cannot provide

sufficient protection; some cases (80°C, 22ppm imidazoline-type inhibitor) show no

protection at all. However, 22 ppm of inhibitor is enough to provide an inhibition

efficiency of 93% at 25°C. This is because when the corrosion rate is low, k_3j≈0,

Equation (40) can be again simplified into Equation (31) which is an ideal Langmuir

model. However, when the temperature increases, the corrosion rate also increases, and hence k_3j is no longer negligible. Therefore, at higher temperatures, the obtained corrosion efficiency usually show a larger deviation from the ideal Langmuir model, especially with lower concentrations of inhibitor.

In addition, inhibitor concentration is a key factor in the Langmuir model. Although at higher temperature, the role of corrosion rate becomes more important, the corrosion rate can be still mitigated by adding a higher concentration of inhibitor. This is because a higher concentration of inhibitor leads to a higher k_ac and thereby limits the impact of the electrochemical desorption term linked to the corrosion rate (k_3j). In conclusion, the influence of temperature is not only through affecting the kinetic parameters of adsorption but also on affecting the corrosion rate of mild steel.

4.3.5 The Role of Temperature on the CMC and Its Impact on the Inhibition Properties of Corrosion Inhibitor

Critical micelle (CMC) concentration plays an important part in the study of corrosion inhibitor. Organic inhibitors are usually ionic surfactants that can form into micelles above certain concentrations [138]. It has been stated that CMC value has a significant effect on an inhibitor's performance. It is believed that above the CMC, the adsorption of inhibitor is not significantly increased by the addition of inhibitor and thereby the efficiency does not increase significantly [139]. In the earlier research, it was noticed that the inhibition performance decreased with temperature. It is logical to question whether this decrease is a result of the change of CMC with temperature.

Therefore, in this part, the CMC values of the inhibitor were measured at 25°C, 50°C and 80°C and its effect on the adsorption behavior and inhibition efficiency was examined.

The determination of CMC is usually through measuring the surface tension considering different concentrations of inhibitor. This process is schematically described in Figure 17, considering a gas/water interface. As the concentration of a surfactant increases, more inhibitor molecules accumulate at the interface and therefore cause a drop in surface tension at the interface (stage 2). However, when the inhibitor concentration is above CMC, inhibitor molecules do not go to the interface anymore because the interface is almost fully occupied (stage 3). As a result, the surface tension does not increase, and the excess inhibitor molecules start to form into micelles (stage 4). By finding the cross point of stage 3 and stage 4, the CMC can be obtained. Note that the decrease of surface tension is usually a linear relationship with the logarithm of inhibitor concentration. This is because the surface tension is also linearly related to the logarithm of the adsorbed inhibitor concentration as shown in Equation (41)[140].

$$\Gamma = -\frac{1}{RT}(\frac{d\gamma}{d(\ln(c))})_T \qquad (41)$$

Where, Γ is the surface excess concentration ($mol \cdot m^{-2}$), γ is the surface tension ($mN \cdot m^{-1}$), c is the inhibitor concentration ($mol \cdot m^{-3}$). However, this linear relationship only lasts in stage 2.

The surface tension measurements were carried out with the KRÜSS K20 tension meter in a 1 wt.% NaCl solution. The CMC measurement at 25°C results is given in Figure 18. It can be seen that the surface tension initially drops with the addition of

inhibitor. However, past around 30 ppm, the surface tension did not noticeably change. By locating the cross point, the CMC of the imidazoline-type inhibitor can be determined as 25±2ppm.

Similarly, the surface tension was measured at 50°C and 80°C as given in Figure 19 and Figure 20. It was found that although the surface tension values at 50 and 80°C were different from at 25°C, the minimum value was still achieved around 30ppm. CMC were determined as 29±2, 28±2ppm for 50°C and 80°C, respectively. At this moment, it seems that temperature does not change the CMC value of the imidazoline-type inhibitor.

$$\Gamma = -\frac{1}{RT}(\frac{d\gamma}{dlnc})_T$$
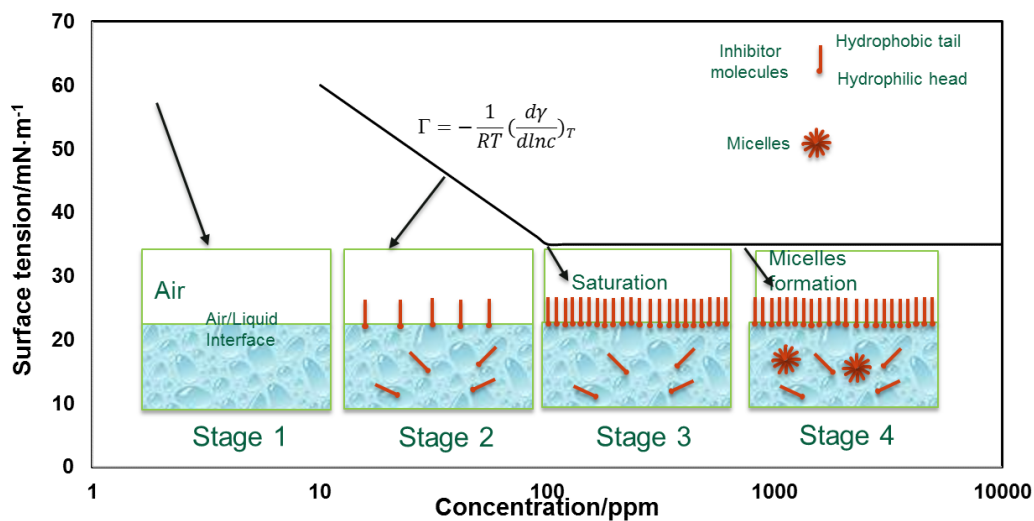
Figure 17. The schematic of the formation of micelles.
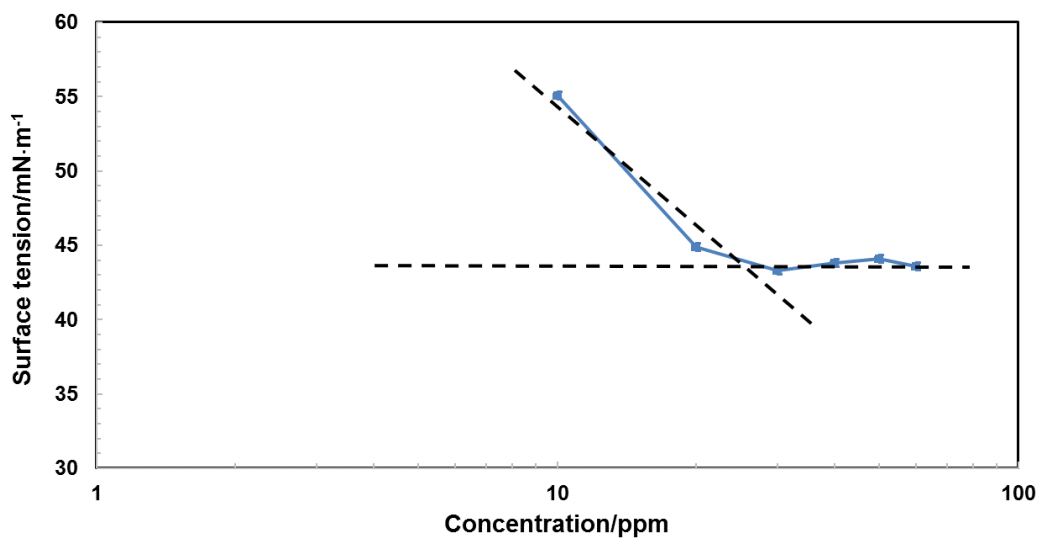
Figure 18. Surface tension *vs.* the imidazoline-type inhibitor concentration at 25°C in 1 wt.% NaCl
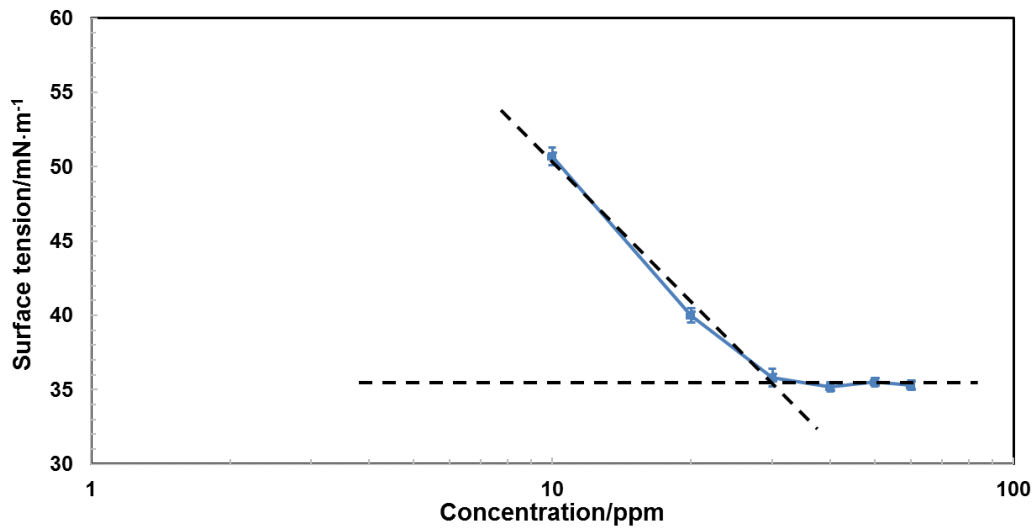
Figure 19. Surface tension *vs.* the imidazoline-type inhibitor concentration at 50°C in 1 wt.% NaCl
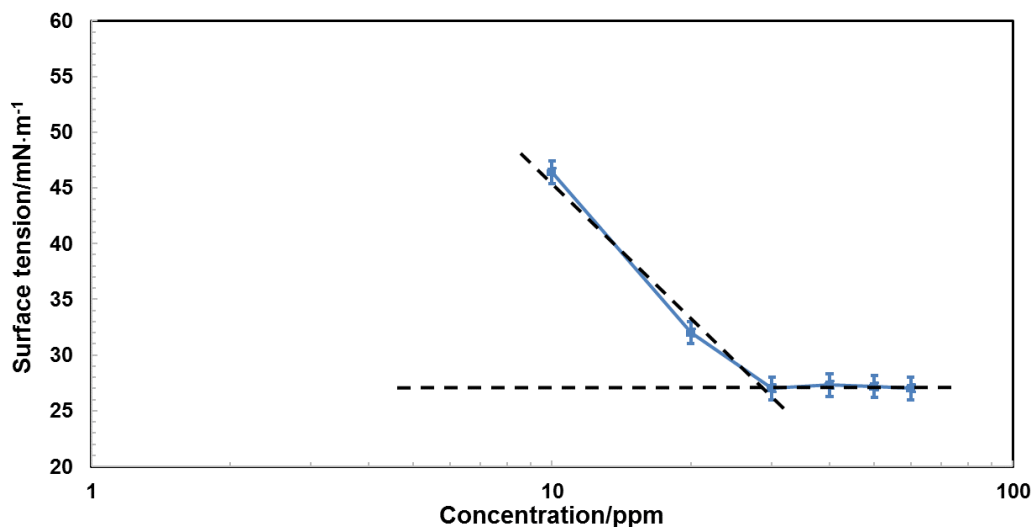
Figure 20. Surface tension *vs.* the imidazoline-type inhibitor concentration at 80°C in 1 wt.% NaCl

At 25°C, the CMC plays a critical role in the inhibition properties of the imidazoline-type inhibitor. First, the maximum adsorption mass was achieved at an inhibitor concentration closely matching the CMC. Figure 6 shows that the maximum frequency change (related to the adsorbed mass) only increased slightly from 22ppm (slightly lower than CMC) to 44ppm (higher that CMC). Moreover, the frequency change at equilibrium was almost not altered (even slightly dropped) from 44ppm to 88ppm, with both concentrations being higher than the CMC. This suggests that with inhibitor concentrations above the CMC, the inhibitor does not adsorb on the crystal surfaces anymore (similar to Figure 17 (stage 3)), suggesting that the CMC correlates with the necessary inhibitor concentration to saturate the surface. Secondly, the inhibition efficiency did not change with concentration when the concentration was above CMC. Figure 12 shows that the equilibrium inhibition efficiency η basically did not change with

the inhibitor concentrations above 22ppm. Therefore, at 25°C, the CMC plays a critical role in determining the inhibitor's maximum abilities both in terms of adsorption behavior and inhibition efficiency.

However, at higher temperature, the role of CMC becomes less significant. At 50°C, the maximum frequency change at equilibrium kept increasing with concentration up to 88ppm (Figure 7), despite the CMC being still around 29ppm. Correspondingly, the inhibition efficiency also increased with concentration up to 88ppm. Clearly, the CMC does not correlate anymore with optimal inhibitor concentration at 50°C. Similarly, at 80°C, 22ppm inhibitor cannot provide any protection against corrosion. Only a concentration of 176ppm inhibitor can inhibit the corrosion rate to 0.4mm·y^{-1} and not cause localized corrosion. The concept of correlation between CMC and optimal corrosion inhibitor concentration does not hold anymore at higher temperature.

There are two possible explanations for the limited role of CMC at elevated temperatures. First, when temperature increases, the adsorption/desorption equilibrium becomes the determining factor for the maximum equilibrium mass adsorbed. The equilibrium usually goes to desorption with the increase of temperature, which means that higher dosage of inhibitor is required to achieve the maximum adsorbing mass. Secondly, the rate of iron dissolution also plays a role on the impact of CMC. When the temperature increases, the surface of mild steel becomes less stable and the iron dissolution rate increases. As a result, the desorption of inhibitor caused by iron dissolution (k_3j) also increases. Therefore, it required higher concentration to achieve sufficient protection (Equation (40)).

4.4 Summary

The adsorption of TOFA/DETA imidazoline inhibitor on gold-coated quartz crystals generally followed the Langmuir adsorption model from 25°C to 80°C over the tested range of concentrations. The desorption of inhibitor was favored at higher temperature because the desorption rate constant k_d increased faster with temperature than the adsorption reaction rate k_a.

Corrosion inhibition tests on mild steel generally showed the same behavior as observed on the gold-coated crystal. At a constant inhibitor concentration, the inhibition efficiency/equilibrium coverage decreased with an increase in temperature.

Failure cases of corrosion inhibition were observed at higher temperatures or with low inhibitor concentrations. This led to either low inhibition efficiency or localized corrosion. However, a higher dose of inhibitor can mitigate the general as well as localized corrosion up to 80°C.

The CMC of the inhibitor has a significant role in the inhibition properties of the imidazoline-type inhibitor at 25°C but its correlation with optimal inhibitor concentration (to achieve maximum inhibition efficiency) does not hold anymore at higher temperature.

CHAPTER 5: INVESTIGATION OF THE PERFORMANCE OF THE IMIDAZOLINE-
TYPE INHIBITOR AT 120 AND 150°C

5.1   Introduction

In the previous chapter, the performance and the adsorption behavior of the

imidazoline-type inhibitor were examined at up to 80°C. It was found that the desorption

of the inhibitor was favored at higher temperatures and therefore the inhibition

performance was undermined. This chapter extends the study on the temperature effect

up to 150°C. As stated in Chapter 4, the main challenges in studying corrosion inhibition

at high temperature is the development of appropriate and representative testing methods.

Glass cell tests under atmospheric pressure are not suitable at temperatures above 100°C,

rendering the use of autoclaves necessary. Issues related to pre-corrosion and inhibitor

injection also need to be addressed. This chapter presents first the development of a new

testing setup which was built to investigate the performance of the imidazoline-type

inhibitor at elevated temperature. The experimental results are then presented in detail.

5.2   Experimental Autoclave Setup Development

Two autoclaves setups were developed to investigate corrosion inhibition at high

temperatures: the initial 'single autoclave' system and the improved 'two autoclaves'

system. While the 'two autoclaves' system ended up being more appropriate to perform

the study, information gathered with the 'single autoclave' system still provided a

number of relevant information. These experimental setups are described in details

below.

5.2.1 Single Autoclave System

The single autoclave system (maximum holding pressure and temperature are 5000psi and 300°C, respectively) consists of a 4-liter autoclave equipped with an inhibitor injector (300mL), as shown in Figure 21 (a). There are three electrodes mounted through the autoclave stainless steel lid, namely an Ag/AgCl reference probe, a Pt-coated Nb counter electrode, and the working electrode. The working electrode is made of API 5L X65 steel (chemical composition is given in Table 3). In addition, the pH is monitored using a ZrO_2-based pH probe that can operate in high temperature and high pressure environments; calibration is performed using standard solutions. Linear polarization resistance (LPR) and open circuit potential (OCP) measurements are performed using a Gamry Reference 600™ potentiostat. The temperature in the autoclave is continuously monitored and controlled using a digital reader. The test electrolyte is stirred using an impeller.
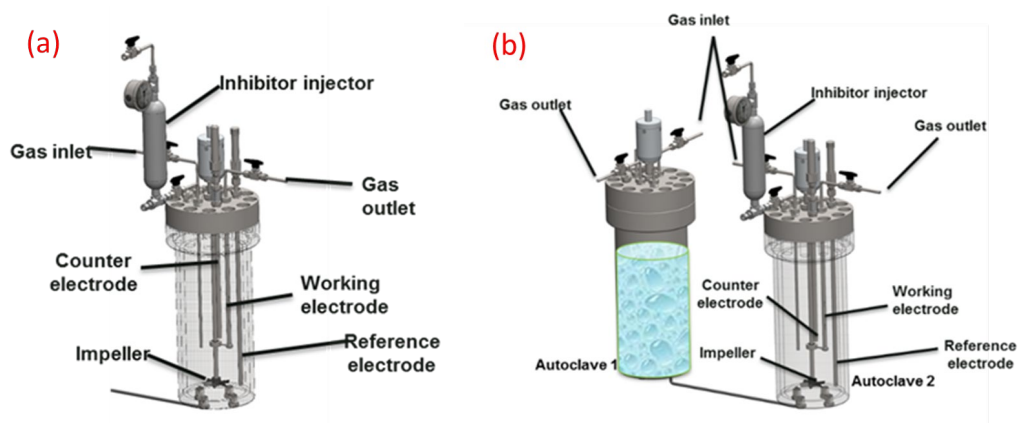
Figure 21. Configuration of the autoclave systems. (a) Single autoclave system, (b) 2-autoclave system (courtesy of Cody Shafer)

Each experiment was conducted in 3L of 1 wt.% NaCl solution. After the electrolyte was poured into the autoclave body, it was purged continuously with CO_2 for more than 2 hours at 80°C to remove O_2. After purging, the stainless steel lid, with pre-installed specimens, electrodes and probes, was attached to the autoclave body. The gas outlet and inlet valves were then closed and the temperature set to the desired value. When the desired temperature was achieved, the system was pressurized with CO_2 to apply an additional 2bar of pressure. Electrochemical measurements (LPR and OCP) were started after this pressurizing step, for use as a baseline condition. Polarization resistance (R_p) measurements were again run from −5mV from the OCP to +5mV from OCP at a scanning rate of 0.125mV/s. The B value for the corrosion rate determination is also 23mV/decade. Solution resistance (R_s) was measured by EIS and subtracted from the measured R_p. After the completion of baseline measurements, the inhibitor solution was injected into the system.

In the injection system, 200mL of 1 wt.% NaCl containing the desired molar amount of corrosion inhibitor was loaded into a pressure bomb; the electrolyte was purged beforehand with N_2 to minimize contamination with O_2. The injection bomb was connected to the autoclave lid using appropriate fittings. When it was the time for injection, the bomb was pressurized with N_2, so its internal pressure was always higher than in the autoclave. Upon the opening of the valve connecting the bomb and the autoclave, the pressure difference drove the inhibitor solution into the autoclave.

The corrosion rate was monitored using LPR for 24 hours. Measurements were carried out every 30 minutes over the first 2 hours and every hour for the remaining 22

hours. Bulk solution pH was measured at the third hour and the end of the experiments and samples of the solution were taken for Fe^{2+} concentration analysis at the end of experiments. The system was then cooled to around 80°C (usually took about 5-6 hours), depressurized, the lid detached, the hanging specimens removed and the solution was drained. This cooling down period can be as long as 8 hours, depending on the temperature tested. The retrieved specimens were stored in a N_2 flushed cabinet for subsequent surface characterization by SEM and EDS as well as by XRD.

The tests operated at 50°C-80°C in the glass cell (see Chapter 4) showed that 1 CMC of inhibitor was not enough to mitigate corrosion. This finding was assumed to also be valid at higher temperatures. Therefore, to ensure a sufficient amount of inhibitor, at least 440ppm (14 times of CMC) corrosion inhibitor was injected in the autoclave setups at each testing temperature.

As mentioned earlier, corrosion inhibition testing at high temperatures holds many challenges. The experiments performed in the single autoclave system, while yielding very interesting findings, also generated some experimental artifacts mostly associated to heating up and cooling down periods. During the heating up period, the specimens were immersed in the non-inhibited solution which generated issues with pre-corrosion and formation of surface layers (corrosion product). Similarly, too lengthy cooling down periods could also alter the results and lead to misinterpretations. Once these issues were identified, an updated version of the system was developed and included a 'two-autoclave' system.

5.2.2 Two-Autoclave System

The second autoclave system is shown in Figure 21 (b). The major difference between the single autoclave system and the 2-autoclave system is that the solutions and the specimens are heated to the desired temperature in two separate autoclaves. Otherwise, the main autoclave components are similar: three electrodes as well as a HTHP pH probe were mounted through the autoclave lid. The temperature was monitored and controlled using the same digital controller. The solution was mixed with an impeller set at 200rpm.

The procedure in the two-autoclave system is only slightly different from the single-autoclave system. The main differences are in the heating up and cooling down periods. First, the solution was pre-heated at 80°C in autoclave 1 and sparged with CO_2 continuously to remove oxygen, with the stainless steel lid on. Autoclave 2, which contains only the specimens, was also sparged with CO_2 and heated to 80°C. After 2-3 hours of purging, gas inlet and outlet valves of both autoclaves were closed and the autoclaves are heated to the desired temperature. Later, the solution was transferred from autoclave 1 to autoclave 2 with pressurized inert N_2 gas by opening valves between the two autoclaves. After the solution was completely transferred, electrochemical measurements were started in autoclave 2. Two LPR measurements were taken as the baseline and then the inhibitor solution was injected into the system through the injection vessel (30 minutes pre-corrosion). Similarly, the corrosion rate was monitored using LPR for the remaining 23 hours. Bulk solution pH was also measured at the third hour and the end of the experiments and solution samples were taken for Fe^{2+} concentration analysis.

After electrochemical measurements ended, autoclave 2 was pressurized again with N_2 and the valve between the two autoclaves was opened to drive the solution from autoclave 2 back into autoclave 1. Therefore, the cooling-down of solution and specimens were also done separately in two autoclaves. Autoclave 2 was then cooled to around 80°C in the inert N_2 environment, depressurized (after usually 2-3 hours), the lid detached, and the hanging specimens removed with the same procedure as in the single-autoclave system. The retrieved specimens were characterized by SEM, EDS and XRD.

The new 'two-autoclave' system yielded the following improvements compared to the traditional 'single-autoclave':

- This significantly limited any potential ingress of oxygen. Oxygen ingress is always a major concern in inhibition tests. By purging the solution with stainless steel lid on, the ingression of oxygen is mostly avoided. For example, the measured oxygen level at the end of purging was below 3ppb.

- The effect of pre-corrosion was significantly reduced. By heating the solution and the specimens in two separate autoclaves, the heating period decreased from 3-4 hours to less than 20 minutes. Therefore, the specimens were essentially uncorroded before the measurement started and hence the formation of corrosion product was delayed.

- The effect of 'post-corrosion' during the cooling down period was also restricted. The solutions and the specimens were cooled down separately as well in the 2-autoclave system and the cooling-down period was reduced from 5-8 hours to 2-3 hours. In the single autoclave system, the corrosion specimens were still in the solution phase, corrosion went on and corrosion product kept developing during the cooling-down

period. In the 2-autoclave system, by keeping the specimens in inert conditions (N_2 environment) at the end of experiments in the two autoclave system, the nature of the corrosion products was not altered during the cooling period.

The tested conditions, which are the same in both autoclave systems, are given in Table 12. Each experiment was performed at least twice to confirm the repeatability.

Table 12. Test matrix of the imidazoline-type inhibitor at 120°C and 150°C

Description	Parameters	
Temperature/°C	120	150
Electrolyte	1 wt.% NaCl solution saturated with 2bar CO_2	
Inhibitor	Talloil fatty acid diethyltriamine imidazoline	
Inhibitor concentration/ppm	0,440 and 800* (*only at 150°C)	
Material	API 5L X65	
pH	Initial pH=4.3 at 80°C after purging with CO_2	
Impeller speed/rpm	200	
Techniques applied	Linear polarization resistance(LPR), open circuit potential(OCP)	

5.3   Results and Discussion

5.3.1 Corrosion Behavior of Carbon Steel at 120°C with and without Inhibitor in the Single Autoclave System

The trend of LPR corrosion rates with time for tests conducted with 0ppm and 440ppm imidazoline-type inhibitor are shown in Figure 22. In the absence of inhibitor, the corrosion rates initially increased to around 10 mm·y^{-1} and remained at this value for

about 8hours. After that point, the corrosion rates gradually dropped to 1 mm·y^{-1} over the next 16hours. This is because, as corrosion progressed, water chemistry changed quickly in the closed autoclave system (increases in pH and [Fe^{2+}] are expected) and resulted in the development of local environments favoring the growth of iron carbonate on the working electrode surface. This led to the formation of an increasingly protective corrosion product layer and a decrease in the corrosion rate for the rest 16 hours.

The test performed with 440ppm corrosion inhibitor shows a different behavior. After the inhibitor was injected into the system, the corrosion rate immediately dropped from an initial value of 10mm·y^{-1} and stabilized at around 3mm·y^{-1} over a period of 3 hours. This behavior is similar to what was previously observed at temperatures of 25°C to 80°C, as shown in Figure 12, Figure 13 and Figure 14. This proves that the inhibitor can still reduce the corrosion rates significantly at 120°C. However, the corrosion rate at the end of the experiment was still high. It is noteworthy that, at the end period of each test, the uninhibited and inhibited corrosion rates were very close (1.5±0.5mm·y^{-1} for the un-inhibited *vs.* 3±1 mm·y^{-1} for the inhibited test). This result by itself is surprising as it suggests that the presence of inhibitor actually led to an increase of the final corroison rate. However, the reasons behind this behavior are more complex and can be explained by considering the formation of corrosion products, which decreased the uniform corrosion rate in the uninhibited test, and the interaction between corrosion products and the inhibitor, which prevented the formation of corrosion products. This is discussed in more detail in the section below dedicated to surface analysis.
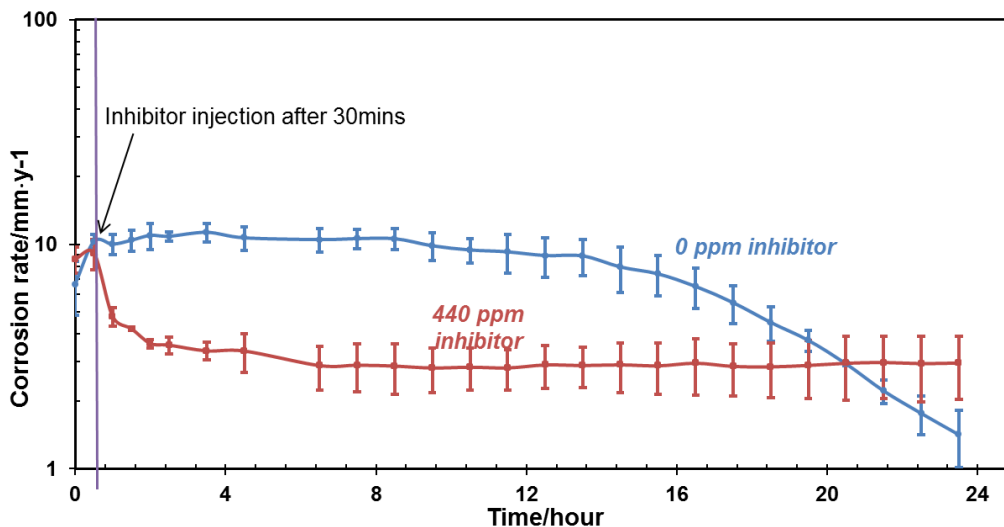
Figure 22. Corrosion rate with/without the imidazoline-type inhibitor at 120°C in the single autoclave system (1wt. % NaCl, 200rpm, pCO$_2$=2 bar)

The XRD patterns of the specimens exposed to the corrosive environments at 120°C are shown in Figure 23. The main corrosion product was identified, as expected, as iron carbonate for the tests without corrosion inhibitor (Figure 23 (a)). However, for the inhibited test, only the iron peaks (44.75°, 65.15°), representing the substrate metal, could be detected (Figure 23 (b)). This means that in the inhibited conditions, no corrosion product was developed. This infers that the decrease in corrosion rate was solely due to the presence of inhibitor and that, as opposed to the blank test, corrosion products played no role.
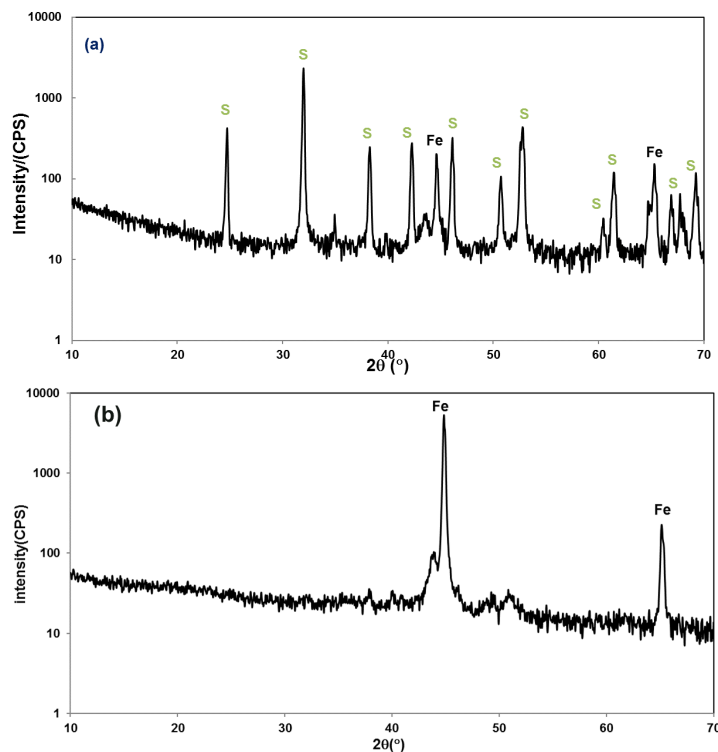
Figure 23.XRD patterns of the specimens retrieved after experiments in the single autoclave system at 120°C. (a) with 0ppm imidazoline-type inhibitor; (b) with 440ppm imidazoline-type inhibitor (S stands for iron carbonate, and Fe stands for iron).

In order to confirm that the development of an iron carbonate layer was the reason behind the decrease in corrosion rate in the uninhibited test, the specimen surfaces were characterized using SEM, as shown in Figure 24 (a) and (b) for the uninhibited and inhibited tests, respectively. Although all the surfaces show extensive signs of corrosion, distinctive features were observed. The surfaces of specimens retrieved in the absence of corrosion inhibitor showed different morphological features as well. The surface with 0ppm inhibitor (Figure 24 (a)) exhibits signs of formation of crystalized structures, which are likely iron carbonate crystals. In comparison, there were only some porous structures on the surface of the specimens immersed with the presence of 440ppm inhibitor (Figure

24 (b)). Clearly, there was no obvious formation of corrosion products on top of the surfaces with the presence of 440ppm inhibitor.
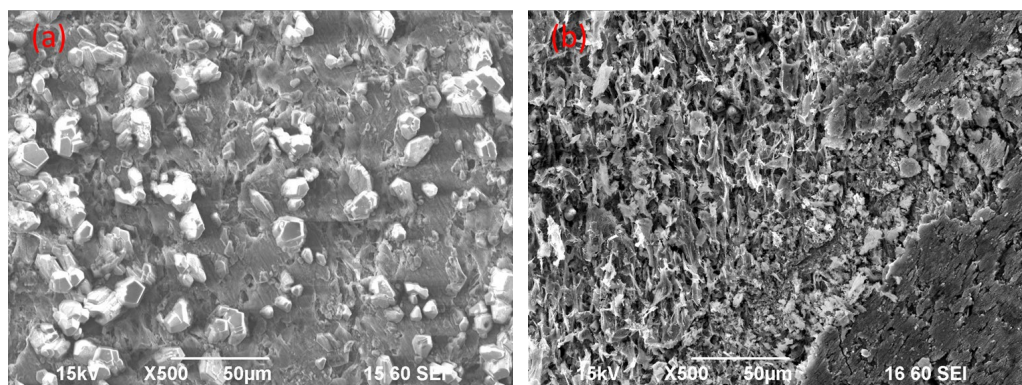
Figure 24. SEM images of the steel surfaces after 120°C test. (a) With 0 ppm imidazoline-type inhibitor; (b) with 440 ppm imidazoline-type inhibitor(1 wt.% NaCl, 200rpm, p_{CO_2}=2 bar)

Cross-section images of the specimens with and without the presence of imidazoline-type inhibitor at 120°C are shown in Figure 25. The SEM images show that there was a corrosion product layer (zone 1) on the steel surface in experiments conducted in the absence of corrosion inhibitor. Combined with the XRD results shown in Figure 23, it can be concluded that the layer is made of iron carbonate and is 40μm thick. In contrast, the corrosion product on the surface of the inhibited specimen did not display any coherent structure comparable to what was observed in the uninhibited test. The absence of any iron carbonate peaks in the XRD patterns (Figure 23 (b)) suggests that its formation was suppressed by the presence of corrosion inhibitor. Instead, the layer visible on top of the steel surface in Figure 25 (b) is postulated to be iron carbide, which

is porous and not protective. This agrees well with what was observed with the surface

morphology (Figure 24).
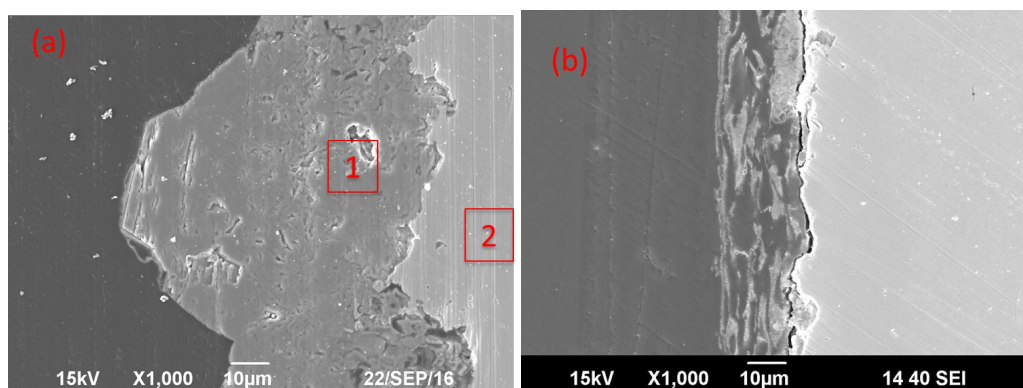
Figure 25. SEM images of steel cross-sections of specimens retrieved from tests conducted at 120°C. (a) with 0ppm imidazoline-type inhibitor; (b) with 440 ppm imidazoline-type inhibitor. (From left to right: epoxy→corrosion product layer→steel matrix).

Consequently, the true effect of chemical inhibition could have been masked in

this test as a consequence of using a single 'closed system' autoclave. To determine the

performance of corrosion inhibitor, it is necessary to know where the uninhibited

corrosion rate is, as indicated in Equation (23). However, in the single autoclave system,

it is not straightforward to define the uninhibited corrosion rate because the corrosion rate

is not stable as a result of the formation of $FeCO_3$ layer. In addition, the inhibited

corrosion rate is not well defined either. The likelihood of corrosion product formation at

120°C makes it difficult to differentiate what contributes the low corrosion rate in the

presence of corrosion inhibitor. Without a thorough understanding of the uninhibited and

the inhibited corrosion rates, the inhibition properties of the imidazoline-type inhibitor

are not clear. Therefore, efforts were made to develop a more appropriate system: the 2-autoclave system. The advantages of the 2-autoclave system can be found in the 5.2.2.

5.3.2 Corrosion Behavior of Mild Steel at 150℃ with and without Corrosion Inhibitor in the Single Autoclave System

Corrosion rates of API 5L X65 specimens exposed to different concentrations of corrosion inhibitor at 150°C are shown in Figure 26. With 0ppm corrosion inhibitor, the corrosion rate initially increased then dropped and stabilized at around $1mm \cdot y^{-1}$; as for the previous test performed at 120°C, this is likely due to the formation of a corrosion product layer. With 440ppm corrosion inhibitor, the corrosion rate decreased steadily over the testing period until it reached a value of around $2mm \cdot y^{-1}$ after 24hours. Figure 26 shows that the results with 0 and 440ppm of inhibitor seem very close. It seems that the addition of inhibitor did not change the corrosion rate or that the concentration of inhibitor is not sufficient. To confirm if this was caused by the lack of inhibitor, an additional experiment with 880ppm corrosion inhibitor was carried out. However, the corrosion behavior with 880ppm of inhibitor ended up being very similar to that observed for the other two tests. This is significantly different from what was observed at 120°C, which showed a sharp decrease in inhibited corrosion rate immediately after injection and not a gradual decrease as seen at 150°C. At this point, it is unclear what, if any, effect the presence of corrosion inhibitor had on the corrosion behavior.
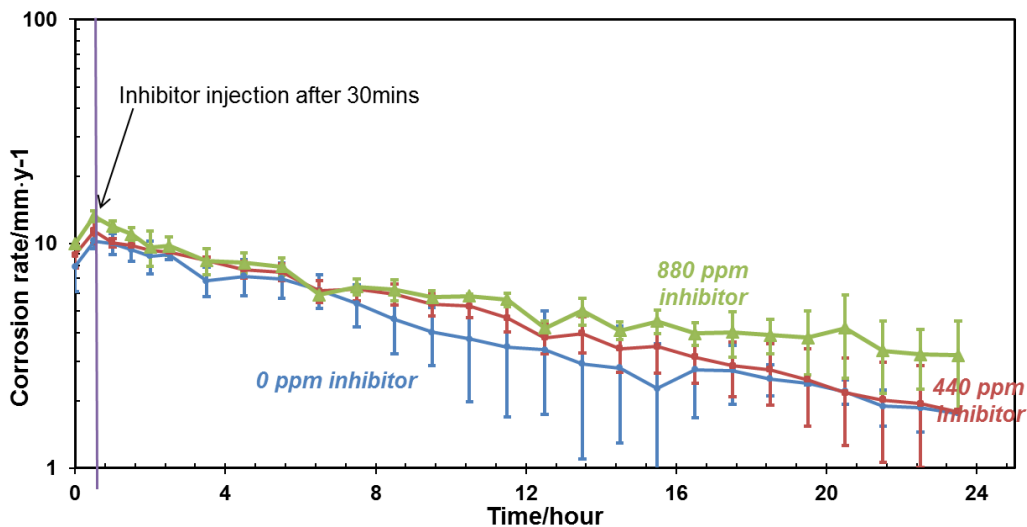
Figure 26. Corrosion rate for different concentrations of imidazoline-type corrosion inhibitor at 150°C. (1 wt.% NaCl, 200rpm, p_{CO2}=2 bar)

The surface of the specimen was characterized by SEM, as shown in Figure 27

(a), (b), and (c). The surface morphologies of the steel specimens with and without

corrosion inhibitor show clear differences. Without corrosion inhibitor, the surface seems

relatively uniform and the presence of a homogeneous corrosion product layer is evident.

However, in the presence of corrosion inhibitor (440 or 880 ppm), a porous,

heterogeneous layer is present on the metal surface which is postulated to be iron carbide.
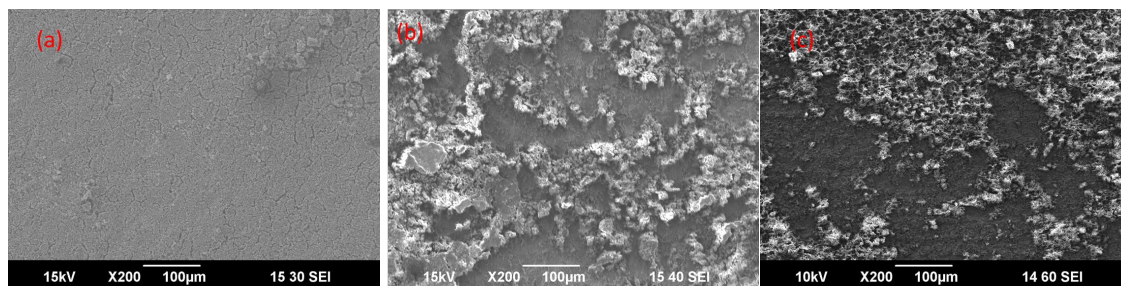
(a) 0ppm inhibitor   (b) 440ppm inhibitor   (c) 880ppm inhibitor

Figure 27. SEM of X65 steel surface with various concentrations of corrosion inhibitor at 150°C. (a) with 0ppm imidazoline-type inhibitor; (b) with 440 ppm imidazoline-type inhibitor; (c) with 880ppm imidazoline-type inhibitor (1 wt.% NaCl, 200rpm, p_{CO_2}=2 bar)

The XRD patterns of the specimens retrieved from the experiments at 150°C are shown in Figure 28. At 150°C, a new type of corrosion product, Fe_3O_4, was observed for the experiments at 150°C, with and without inhibitor. Fe_3O_4 was also observed at high temperature in other researchers' work [21,22]. It is noteworthy that, in the tests with corrosion inhibitor, the XRD patterns feature low-intensity peaks of Fe_3O_4 and high-intensity peaks of iron. Conversely, the XRD pattern associated with the uninhibited specimen shows high intensity peaks for Fe_3O_4, which suggests that the thickness of the Fe_3O_4 layer for the test with corrosion inhibitor was thinner than for the test without corrosion inhibitor.
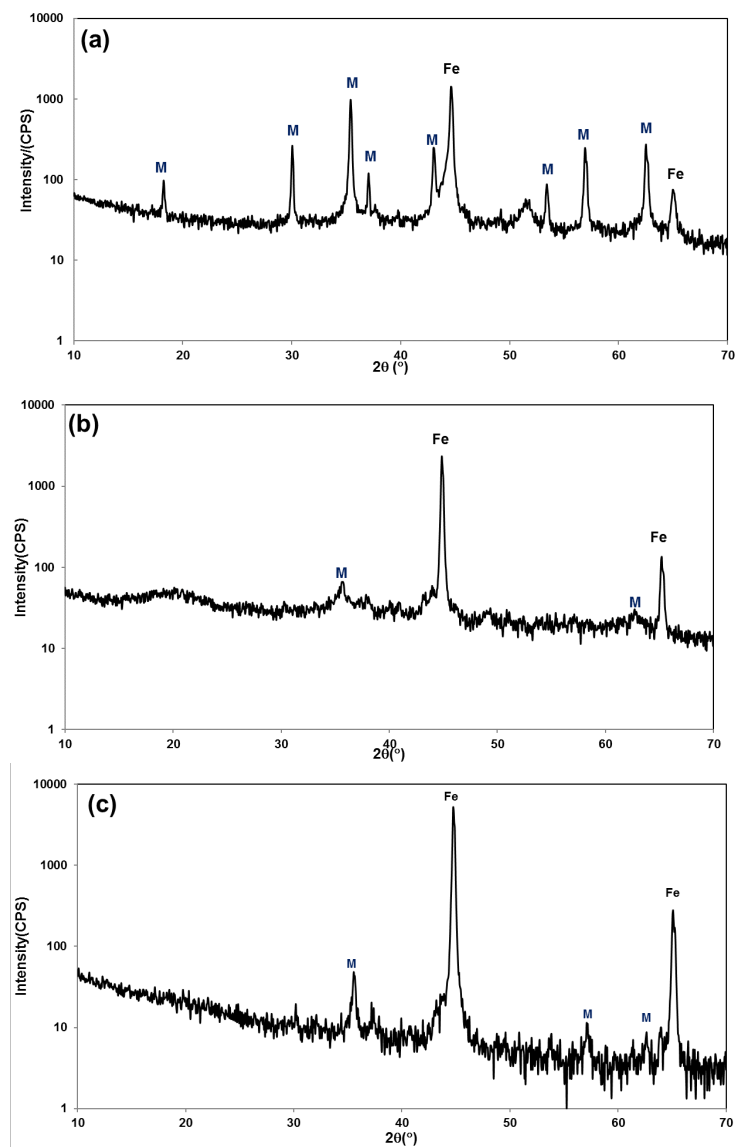
Figure 28. XRD patterns of the specimens retrieved after experiments in the single autoclave system at 150°C. (a) with 0ppm imidazoline-type inhibitor; (b) with 440ppm imidazoline-type inhibitor; (c) with 880ppm imidazoline-type inhibitor(S stands for iron carbonate, M for Fe_3O_4 and Fe for iron).

In addition, the specimen cross-sections were examined by SEM/EDS as shown in Figure 29 (a), (b), and (c). Figure 29 (a) clearly indicates the presence of a thick corrosion product layer (40μm) for the uninhibited conditions. However, no apparent layer was

observed in the inhibited environments, as shown in Figure 29 (b), or (c). This again

confirms that the formation of corrosion product was significantly hindered by the

presence of the imidazoline-type corrosion inhibitor as at 120°C.
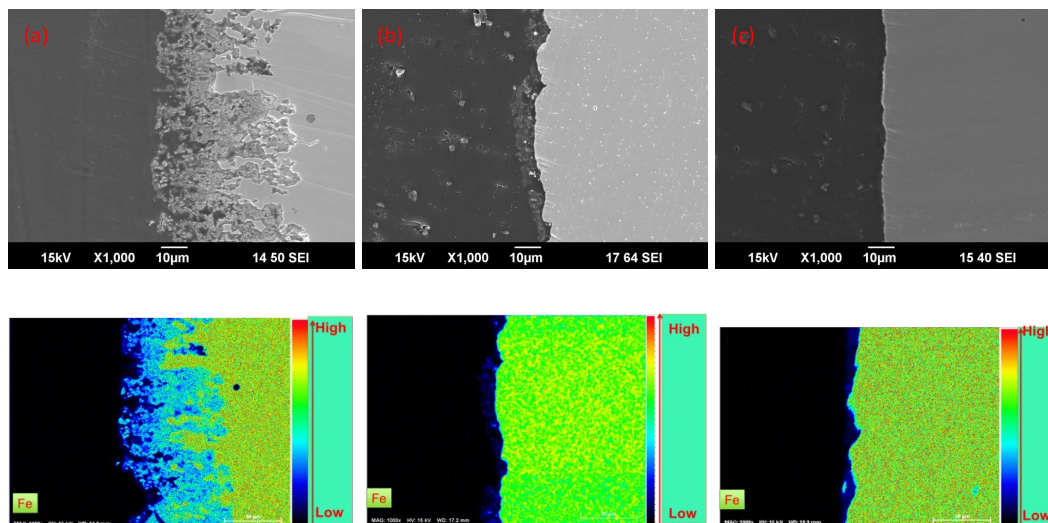
Figure 29 Cross-sections images and EDS Fe element mapping of specimens with various
 concentrations of corrosion inhibitor at 150°C. (a) with 0ppm imidazoline-type inhibitor;
(b) with 440 ppm imidazoline-type inhibitor; (c) with 880ppm imidazoline-type inhibitor.

The use of the single autoclave setup at 120°C and 150°C proved problematic and

significantly complicated the interpretation of the results. Experimental artifacts, linked

to the formation of corrosion products, masked the true effect of the inhibitor. The main

issue with the single autoclave system was the long heating and cooling transition periods

that could have led to the formation of corrosion product even before the inhibitor was

injected. To address this issue, the two-autoclave system was developed so that the

solution and the specimens were heated separately. This would reduce the transition

periods and, hence, the formation of corrosion product thereby isolating the effect of corrosion inhibitor.

5.3.3 Corrosion Behavior of Mild Steel at 120°C with Reduced Transition Period with and without Imidazoline-Type Inhibitor in the Two-Autoclave System

As stated above, the long transition time associated with the heating up period, before any actual measurement could take place, might have altered the results of inhibitor performance. To clarify the role of inhibitor, similar experiments were carried out in the 2-autoclave system, which was designed to limit the pre-corrosion time. In the new system, the pre-corrosion was completely by-passed. The trend of LPR corrosion rates with time, with and without imidazoline-type inhibitor at 120°C, is shown in Figure 30. In the uninhibited system, the corrosion rate was initially around 5mm·y^{-1} and increased gradually to 9mm·y^{-1} during the first hour. After that, corrosion rate remained around 9mm·y^{-1} for the next 22 hours of exposure. The stable corrosion rate suggests that the formation of corrosion product layers was prevented in the 24 hour experiment, indicating that, in the new 2-autoclaves system, the formation of corrosion product was at least significantly delayed. This is likely a result of a decrease in the carbon steel specimen exposure time to the solution, which decreases the pre-corrosion time and minimized the release of Fe^{2+} ions in solution. It is fully expected that, with enough exposure time, significant changes in water chemistry would also occur, as with the single autoclave. However, by minimizing the precipitation of the surface layers in the first 24 hours, the use of the two-autoclave system appears to be a more appropriate setup for the investigation of high temperature corrosion inhibition.

In the presence of 440ppm of imidazoline-type inhibitor, the corrosion rate

dropped quickly from an initial corrosion rate of 7mm·y^{-1} to 3.5mm·y^{-1} after the addition

of corrosion inhibitor. The corrosion rate then remained stable for the rest of the

experiment. This behavior is similar to what was previously observed at 120°C in the

single autoclave system (Figure 22). The similarity in inhibited corrosion rate between

the single and the two-autoclave systems also suggests that the performance of the

inhibitor is accurately captured in both autoclave systems. Only the baseline uninhibited

test is strongly affected by the experimental procedure.
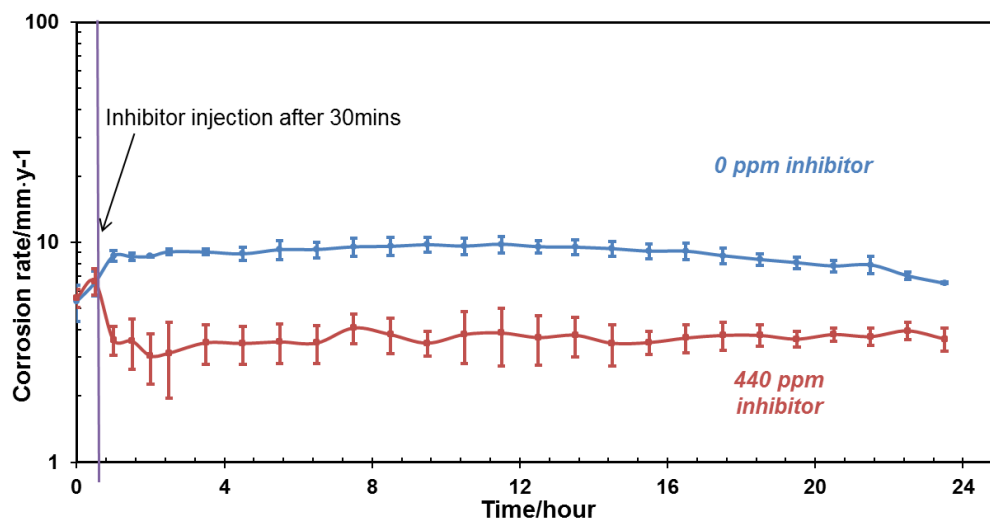
Figure 30. Corrosion rate with/without the imidazoline-type inhibitor at 120°C in the two autoclave system (1 wt.% NaCl, 200rpm, p$_{CO2}$=2 bar)

Since the uninhibited corrosion rate could be determined with confidence in the

two-autoclave system, the inhibition efficiency ($\boldsymbol{\eta}$) of the imidazoline-type inhibitor was

calculated as 61% from Equation (23). In the absence of inhibitor, the fact that the

corrosion rate remained constant during the entire duration of the test suggests that no protective corrosion product layer formed. This is different from what was observed in the single autoclave system, in which a thick layer of corrosion product was formed (Figure 25). The surface was characterized using XRD, SEM and EDS to confirm the absence of an iron carbonate layer.

The XRD patterns of the specimens recovered from the test with and without inhibitor, at 120°C, are shown in Figure 31. The major difference from the single autoclave system is that even without corrosion inhibitor, the $FeCO_3$ peaks are absent. This again proves that the formation of iron carbonate in the new system was completely bypassed in the tested period (2 4hours). Therefore, the limited exposure time of the steel specimen to the electrolyte minimized the effect of pre-corrosion and buildup of Fe^{2+} in solution; this delayed the formation of iron carbonate.
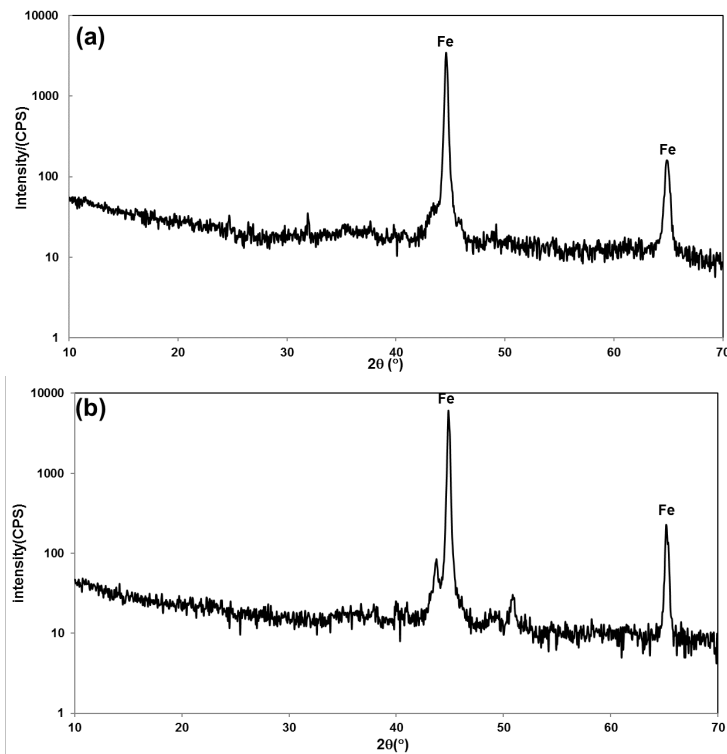
Figure 31 XRD patterns of the specimens retrieved after experiments in the two autoclave system at 120°C. (a) with 0ppm imidazoline-type inhibitor; (b) with 440 ppm imidazoline-type inhibitor (Fe stands for iron).

Figure 32 shows the formation of a very porous corrosion product layer (Fe_3C) without inhibitor while the absence of $FeCO_3$ crystals is also noticeable. In Figure 32 (b), the surface appears relatively flat with sheet-like features, often associated with iron carbide, partly covering the surface. The formation of $FeCO_3$ was significantly delayed at 120°C in the two-autoclave system.
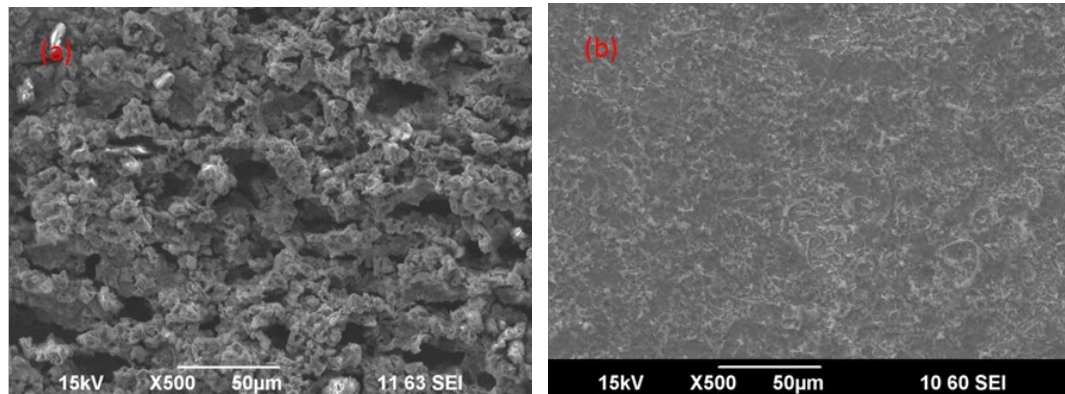
Figure 32. SEM images of specimen surfaces from 120°C experiments. (a) With 0ppm imidazoline-type inhibitor; (b) with 440 ppm imidazoline-type inhibitor

The cross-section images are shown in Figure 33. On the one hand, in the absence of corrosion inhibitor, a loose layer on top of the steel substrate is seen in Figure 33 (a). As the XRD results have shown (Figure 31), this loose layer is likely made of cementite since no $FeCO_3$ could be detected. This layer of cementite is usually porous, hence cannot work as an effective mass transfer barrier and mitigate the corrosion rate. On the other hand, no apparent layer can be noticed on top of the surfaces exposed to the solutions with inhibitor. This behavior is similar to what observed in the single autoclave system. The missing of iron carbides in the tests was probably due to artificial reasons. The specimens needed to be rinsed with isopropanol and water after experiments to remove possible residue salts and other residues. Some porous precipitates was washed away during the rinsing. This precipitate was most likely the iron carbides residues, because corrosion products (iron carbonate or Fe_3O_4) are usually well attached to the matrix.
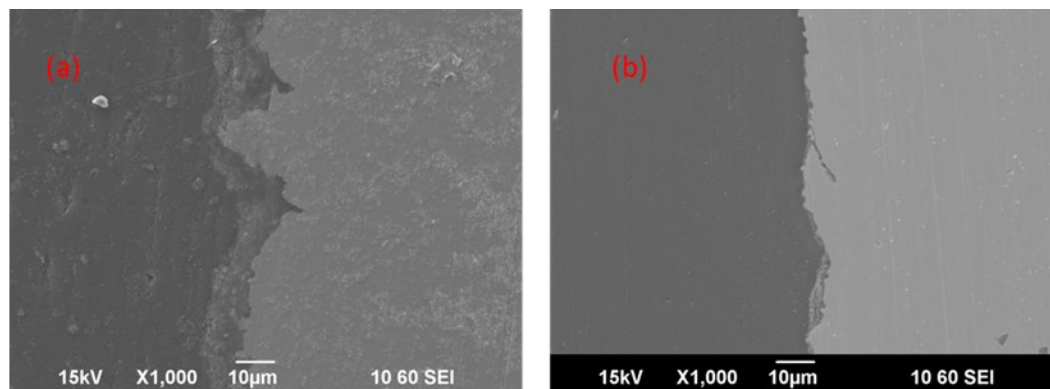
Figure 33. Cross-section images of the specimens retrieved from 120°C experiments. (a) With 0ppm imidazoline-type inhibitor; (b) with 440 ppm imidazoline-type inhibitor (From left to right in each image: epoxy→steel)

5.3.4 Corrosion Behavior of Mild Steel at 150°C with and without Corrosion Inhibitor in the Two-Autoclave System

Corrosion rates of mild steel specimens exposed to different concentrations of the imidazoline-type corrosion inhibitor at 150°C are shown in Figure 34. The results were obtained in the two-autoclave system which minimized transition times (heating-up and cooling-down periods). At 0ppm corrosion inhibitor, the corrosion rate increased slightly at the beginning of the test and then decreased gradually. Once again, the decrease of the corrosion rate was likely due to the formation of corrosion products, even in the 2-autoclave system which was designed mainly to delay the formation of corrosion products. With 440ppm corrosion inhibitor, the corrosion rate trend was repeatedly very similar to what was observed without the imidazoline-type inhibitor. The corrosion rate decreased to around 3mm·y^{-1} after the 24 hour experiment. Similarly, with 880ppm inhibitor added into the system, the corrosion rate also monotonously decreased to around 6mm·y^{-1}. It is noteworthy that in the initial 10 hours, the corrosion rates did not seem to

be affected by the presence of inhibitor in the system. These results also resemble what was obtained in the single autoclave system.

The results suggest that the addition of corrosion inhibitor did not inhibit the corrosion rate at 150°C even with a limited pre-corrosion period. The results also suggest that corrosion products can form relatively rapidly at 150°C and play a significant role in determining the corrosion rate.
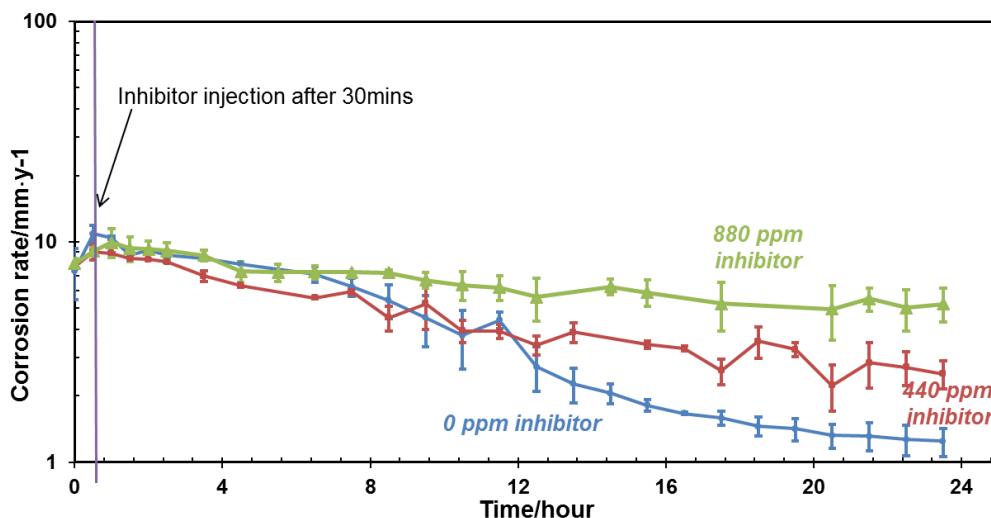
Figure 34. Corrosion rates with various amount of the imidazoline-type inhibitors at 150°C in the two autoclave system. (1wt. NaCl, p_{CO2}=2 bar)

XRD patterns of the specimens' surfaces were obtained to identify the corrosion products, as shown in Figure 35. The patterns are comparable to the XRD data obtained in the single autoclave system at 150°C (Figure 28). In the absence of corrosion inhibitor, the Fe_3O_4 peak intensity is high, which suggests that a thick layer of magnetite formed on the surface of the specimen. In the presence of inhibitor, the same Fe_3O_4 peak was

detected but at a much lower intensity. Therefore, the formation of Fe_3O_4 was neither avoided nor delayed in the 2-autoclave compared to the single autoclave system.
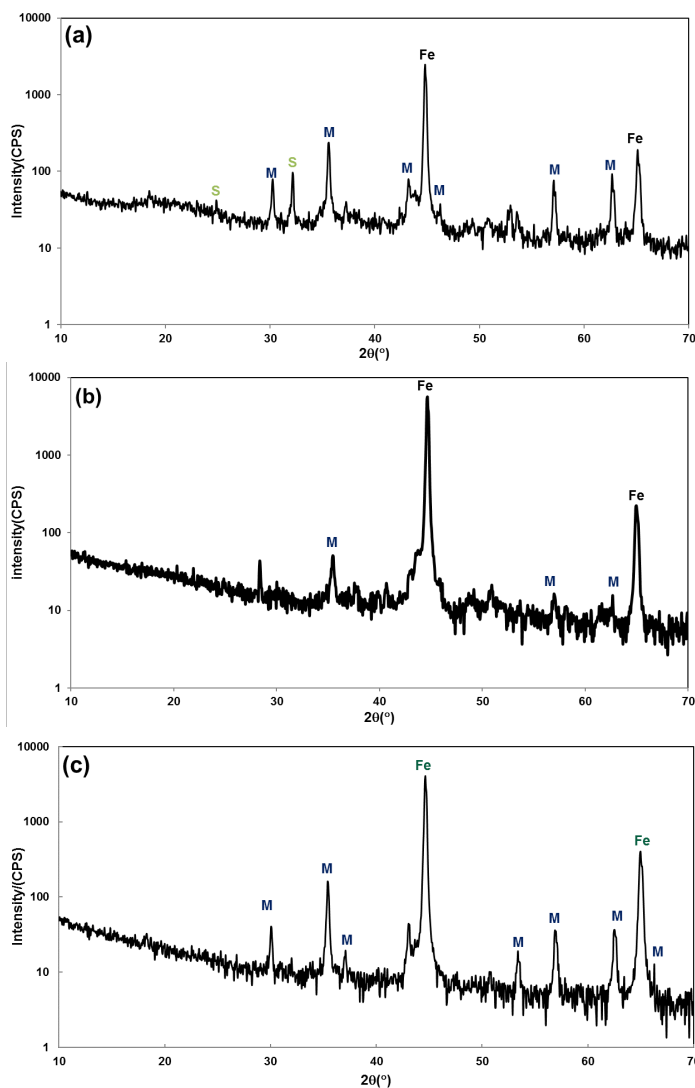
Figure 35. XRD patterns of the specimens retrieved after experiments in the two-autoclave system at 150°C. (a) With 0ppm imidazoline-type inhibitor; (b) with 440 ppm imidazoline-type inhibitor; (c) with 880ppm imidazoline-type inhibitor. (Fe stands for iron, S stands for $FeCO_3$ and M stands for Fe_3O_4)

The surface morphologies of the specimens, considering the tests with and without corrosion inhibitor, are shown in Figure 36 (a), (b), (c). Again, in the uninhibited environments (Figure 36 (a)), the surface of the mild steel specimen featured a uniform surface with crystalline structures on top, similar to what was observed in the single autoclave system (Figure 36 (a)) However, the surface of the specimen collected from the inhibited tests was uneven and partly covered with a very porous layer (Figure 36 (b), (c)), which is likely a residue of cementite.
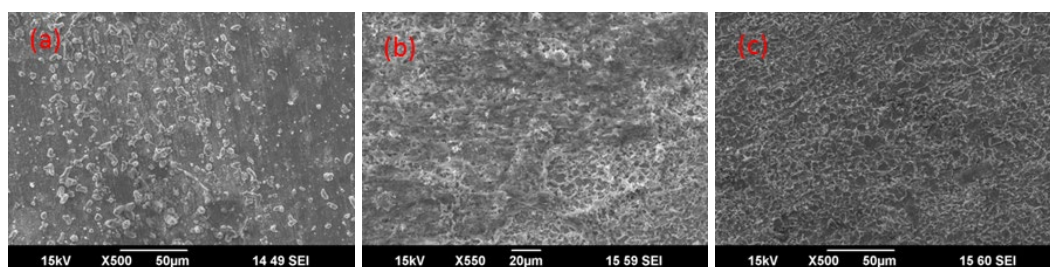
Figure 36. Surface morphology of mild steel for various concentrations of corrosion inhibitor at 150°C. (a) With 0ppm imidazoline-type inhibitor; (b) with 440 ppm imidazoline-type inhibitor; (c) with 880ppm imidazoline-type inhibitor.

The cross-section images of the corrosion product layers obtained from tests with and without corrosion inhibitor are shown in Figure 37 (a), (b), (c). In the uninhibited system (Figure 37(a)), a corrosion product layer was observed with a thickness of 30-40 μm. However, in the inhibited system, no obvious layer was identified. Again, this is analogous to what was observed in the single autoclave system (Figure 37).
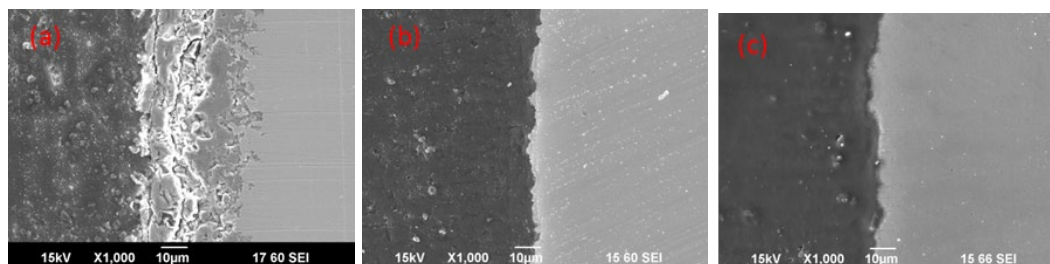
Figure 37. Cross-section images of the mild steel specimens for various concentrations of corrosion inhibitor at 150°C with limited transition period. (a) With 0ppm imidazoline-type inhibitor; (b) with 440 ppm imidazoline-type inhibitor; (c) with 880ppm imidazoline-type inhibitor.

The experimental work above demonstrates that the uninhibited corrosion results are strongly affected by the formation of corrosion product layers (either $FeCO_3$ or Fe_3O_4). However, the inhibition performance *per se* does not seem to be significantly altered by simply shortening the transition periods (heating-up and cooling-down) and avoiding pre-corrosion or corrosion product build-up.

At 120°C, although the formation of $FeCO_3$ was considerably delayed, the inhibited corrosion rates in the single-autoclave and the 2-autoclave system were still fairly similar, which means the efficiency of the inhibitor was not affected by the pre-corrosion time at this temperature. In addition, experimental data showed that the imidazoline-type inhibitor prevented the precipitation of $FeCO_3$, inferring that the decrease in corrosion rate compared to the baseline data was solely due to the presence of inhibitor.

At 150°C, it is difficult to tell whether it is the formation of corrosion product ($FeCO_3$ or Fe_3O_4?) or the adsorption of the imidazoline-type inhibitor which governs the corrosion rate. First, the differences between the inhibited and uninhibited corrosion rates

were not significant, no matter the autoclave system used. Therefore, it is not likely that the presence of the imidazoline-type inhibitor determined the corrosion rate. Second, the presence of inhibitor did prevent the precipitation of $FeCO_3$ but could not stop the formation of Fe_3O_4. In this case, the uninhibited corrosion was likely controlled by the presence of Fe_3O_4 rather than $FeCO_3$. However, more efforts are still needed to investigate the interaction between Fe_3O_4 and the inhibitor adsorption.

In summary, it is clear that Fe_3O_4 is probably the governing factor of corrosion at 150°C. As a result, a new hypothesis was proposed:

- 3rd hypothesis: At 150°C, the formation of Fe_3O_4 is kinetically favored, the protectiveness of Fe_3O_4 is dominant and takes control of the corrosion rate.

To demonstrate the role of Fe_3O_4 on the inhibition performance of the imidazoline-type inhibitor, additional experiments are required to further limit the formation of Fe_3O_4. Firstly, the imidazoline-type inhibitor showed a notable ability to prevent the formation of corrosion products in the earlier work. Secondly, the 2-autoclave system experimental procedure was again modified to further constrain the formation of Fe_3O_4. The previous procedure included a half hour pre-corrosion before the injection of corrosion inhibitor; this short pre-corrosion time period was removed by injecting inhibitor into the heated solution before transferring it to the autoclave with the X65 specimens. Through the modified procedure, the pre-corrosion is limited at a maximum level and thus the role of inhibitor should be further unveiled.

5.3.5 Corrosion Inhibition Behavior without Pre-Corrosion at 120 ℃

In this section, supplementary experiments with a new procedure in the 2-autoclave system were performed to further limit the formation of Fe_3O_4 and to better understand its role in corrosion inhibition.

The updated testing system presents a slight modification from the 2-autoclave system, as shown in Figure 38. The major difference is that the corrosion inhibitor injector was attached to Autoclave 1 instead of Autoclave 2 (see Figure 21 (b)). By doing so, the inhibitor can be injected into the solution prior to contacting the specimens and thereby limiting pre-corrosion time to a minimum. Otherwise, the new autoclave system is identical to the earlier 2-autoclve system (details can be found in Section 5.2.1).
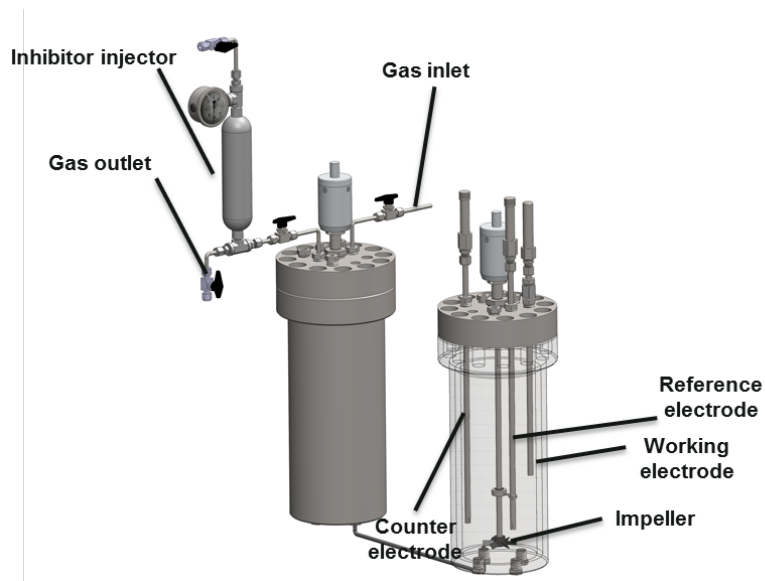
Figure 38. A new design of the 2-autoclave system (courtesy of Cody Shafer)

The experimental procedure was also similar to that described in Section 5.2.2. The major difference was that when both autoclaves reached the desired conditions, the inhibited solution was injected into autoclave 1 by pressurized CO_2 gas. After the inhibited solution was completely injected into autoclave 1, autoclave 1 was pressurized with excess CO_2 to transfer the deoxygenated and inhibited solution to autoclave 2 by opening valves between the two autoclaves. Therefore, the pre-corrosion can be completely bypassed. In the earlier procedure, the injection of corrosion inhibitor occurred after the electrolyte was transferred. The test matrix is the same as earlier work shown in Table 12. Other settings are the same as described in Section 5.2.2.

Figure 39 presents the corrosion rate trends obtained with 0 and 440ppm imidazoline-type inhibitor, and with 0 and 30 minutes pre-corrosion. Only the results obtained without precorrosion are new and the other two lines have been already presented in the previous chapter. However, they are shown here together to ease comprehension and comparison. As it was stated before (see section 5.3.3), the corrosion rate without inhibitor in the system increased from around $5mm \cdot y^{-1}$ to around $9mm \cdot y^{-1}$ in the first couple hours of exposure and stabilized around $9mm \cdot y^{-1}$ afterwards. Due to the stability of this corrosion rate, it was considered as the baseline uninhibited corrosion rate at 120°C. With the injection of corrosion inhibitor and a pre-corrosion time of 30min, the corrosion rate started at $5mm \cdot y^{-1}$ and slightly increased to $7mm \cdot y^{-1}$ during the pre-corrosion time – however, the corrosion rate quickly decreased to $3.8mm \cdot y^{-1}$ after inhibitor injection.

The new test performed without any pre-corrosion showed a stable corrosion rate of 4mm·y^{-1} from the start of the test. The inhibited corrosion rates with or without pre-corrosion are very close (4.0mm·y^{-1} *vs.* 3.8mm·y^{-1}) and the inhibition efficiency can be determined at 60%. In conclusion, at 120°C, the corrosion inhibition performance was not altered by the presence of 30 min of pre-corrosion.
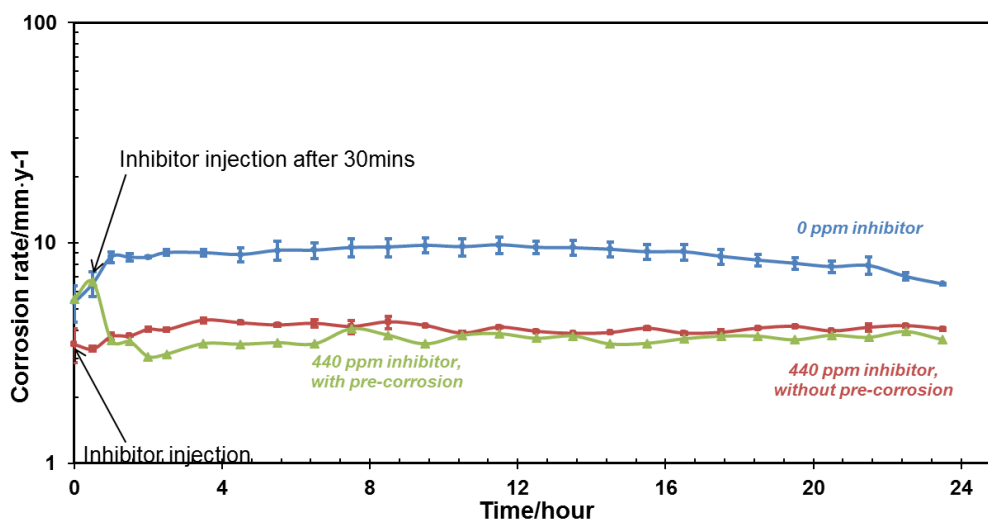
Figure 39. Corrosion rates at 120°C with and without the imidazoline-type inhibitor (1 wt.% NaCl, 200rpm, p_{CO2}=2 bar; B=23mV/decade)

The XRD patterns of the specimens with and without the imidazoline-type inhibitor at 120°C are shown in Figure 39. As mentioned earlier, no other peaks other than the peaks at 44.75° and 65.15° (representing iron) were determined in the XRD patterns of the specimens in the absence of corrosion inhibitor. This suggests that no corrosion product ($FeCO_3$ or Fe_3O_4) was formed in the 24 hour experiments. Similarly, no iron carbonate peak was observed in the XRD patterns with the presence of 440 ppm

imidazoline-type inhibitor. This shows good agreement with the surface morphology in

Figure 40, which exhibited no sign of the formation of corrosion product.
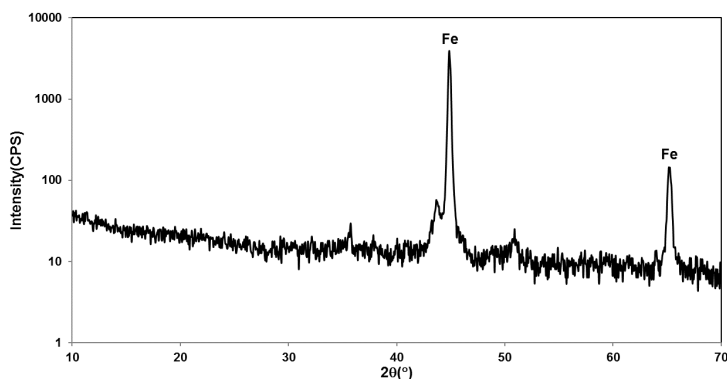
Figure 40. XRD patterns of the specimens obtained from 120°C experiments with
440ppm imidazoline-type inhibitor without pre-corrosion (Fe stands for iron)

The surface morphology and cross-section images with and without inhibitor at

120°C are shown in Figure 41, Figure 42. There was no sign of the formation of

corrosion product in the tested conditions. Therefore, it can be seen that the decrease in

the corrosion rate with the addition of corrosion inhibitor was only a result of the

adsorption of inhibitor. This finding agrees well with what was observed in the earlier

designed 2-autoclave system (see Figure 32 (b) and Figure 33 (b)). Clearly, the new

testing apparatus did not change the performance of the inhibitor at 120°C. However, the

results still conform with the new hypothesis. The focus of the new hypothesis is that the

development of the Fe_3O_4 takes over the role of corrosion inhibitor. As a result, the

corrosion rate was not likely affected by changing the procedure at 120°C because that

Fe_3O_4 is not likely formed at this temperature.
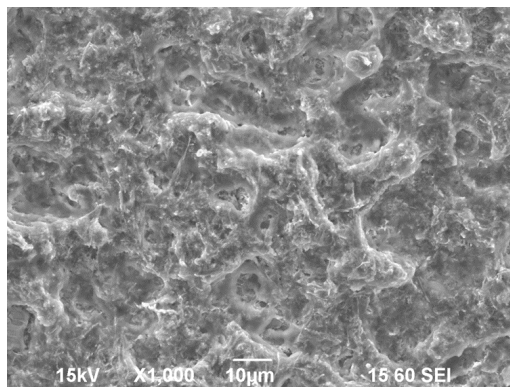
Figure 41. Surface morphology of the specimens retrieved from 120°C experiments without pre-corrosion with the presence of 440ppm imidazoline-type inhibitor.
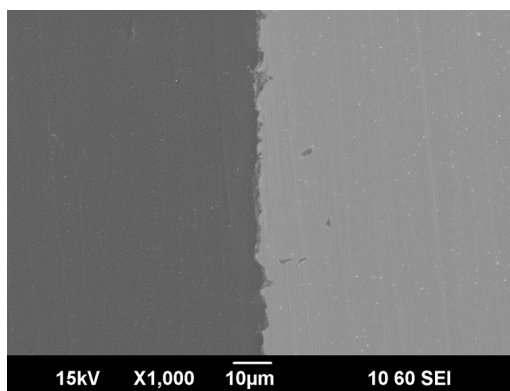
Figure 42. Cross-section images of the specimens retrieved from 120°C experiments without pre-corrosion with the presence of 440ppm imidazoline-type inhibitor.

5.3.6 Corrosion Inhibition Behavior without Pre-Corrosion at 150°C

A similar process was reproduced at 150°C. Figure 43 shows the corrosion trends obtained with and without inhibitor (440ppm) and without pre-corrosion (30 min). The results obtained without inhibitor and with pre-corrosion have already been shown in the section and are repeated here for ease of comparison. The corrosion rate without corrosion inhibitor first increased from 8mm·y^{-1} to 11 mm·y^{-1} after 30 minutes (due to the

formation of carbide), remained relatively unchanged for the next 7hours period and then gradually decreased to 1mm·y^{-1} over the remaining 24hours testing period. This trend is due to the formation of Fe_3O_4.

However, when pre-corrosion is totally avoided, the inhibited corrosion rate behaved differently compared to the results obtained with 30 min pre-corrosion. At first, the corrosion rate also started from around 8mm·y^{-1}, however, instead of increasing slightly in the first hour of exposure, it decreased rapidly to 6mm·y^{-1}, almost remained unchanged during the remaining test duration, only decreasing slightly to 5.5mm·y^{-1}. In contrast, in the case with pre-corrosion (30 min), the corrosion rates kept decreasing over the test duration, likely due to the formation of Fe_3O_4.

Similarly, with 880ppm imidazoline-type inhibitor, the corrosion rate also decreased sharply at the beginning of the test and declined slowly to around 4.5mm·y^{-1}. The corrosion trend without pre-corrosion is completely different from the one obtained with 30 minutes pre-corrosion. With pre-corrosion (30 min), the corrosion rate almost followed the same trend with or without corrosion inhibitor. This means that the presence of inhibitor had little to no effect on the corrosion rate which kept decreasing with time, probably due to the rapid formation of Fe_3O_4. The elimination of pre-corrosion lead to a very different corrosion rate trend and successfully limited the formation of Fe_3O_4. This, in turn, enables identification of the true effect of inhibition at 150°C.
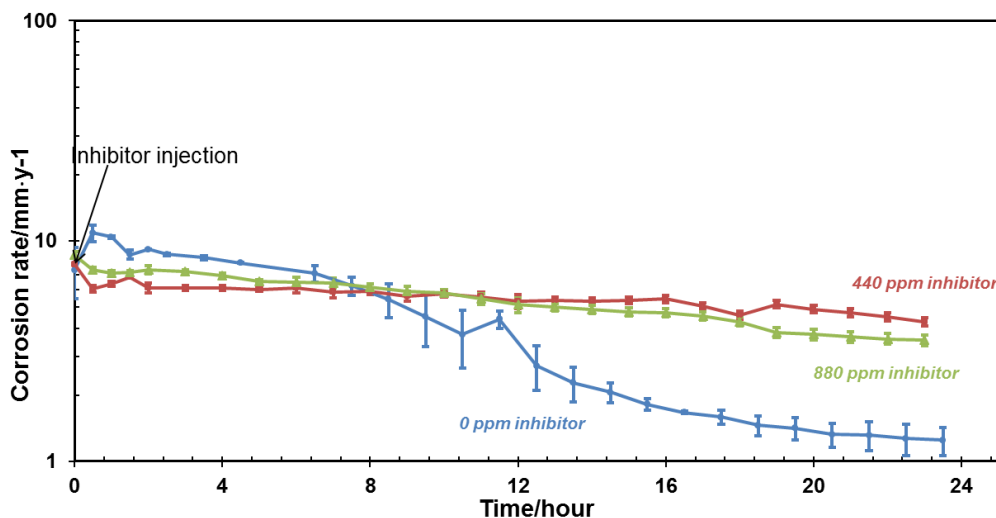
Figure 43. Corrosion rate without pre-corrosion at 150°C with various amount of the imidazoline-type inhibitor. (1 wt.% NaCl, 200rpm, p_{CO2}=2 bar; B=23mV/decade)

The XRD patterns of the specimens retrieved from 150°C experiments were taken and are shown in Figure 44. As indicated in Figure 35 (a), the corrosion product at 150°C experiments without corrosion inhibitor is a mixture of $FeCO_3$ and Fe_3O_4. However, despite the implementation of the new procedure limiting pre-corrosion and the formation of Fe_3O_4, Fe_3O_4 was still found in the XRD patterns with the presence of corrosion inhibitor in Figure 44 (a) and (b). Note that the formation of the Fe_3O_4 is limited as the intensity of the Fe_3O_4 peak with corrosion inhibitor is only 1/6 of the intensity without corrosion inhibitor (Figure 35 (a)); identical data acquisition parameters were used. The finding of Fe_3O_4 in the XRD patterns is not surprising because the formation of Fe_3O_4 is kinetically favored at 150°C. As a result, the development of Fe_3O_4 is almost unavoidable at this temperature. The formation kinetics of Fe_3O_4 are discussed later in Section 5.3.9.
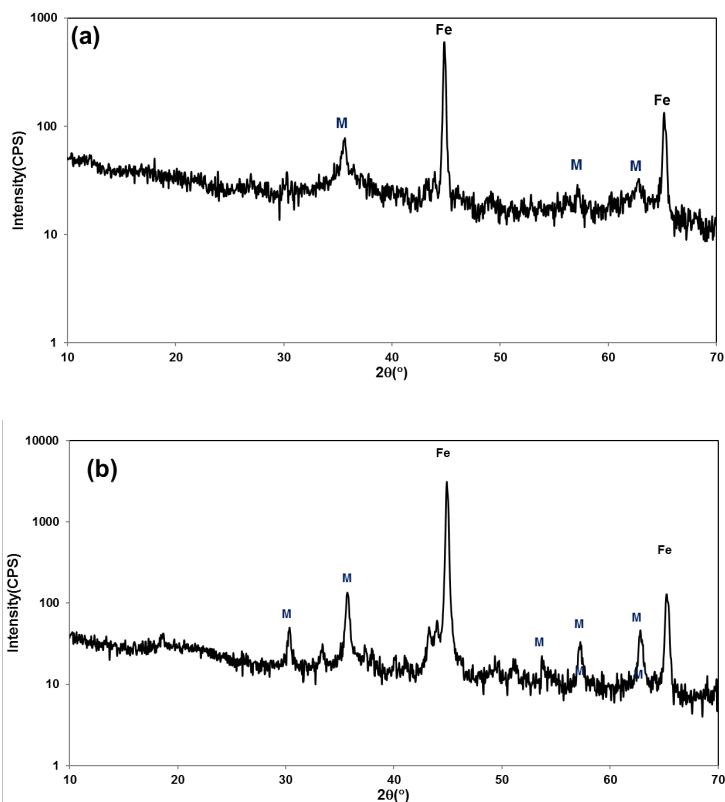
Figure 44. XRD patterns of the specimens from 150°C experiments without pre-corrosion. (a) With 440ppm imidazoline-type inhibitor; (b) with 880ppm imidazoline-type inhibitor (Fe stands for iron, M stands for Fe_3O_4 and S stands for iron carbonate)

Figure 45 shows the surface morphology of the specimens exposed to 150°C experiments and different concentrations of inhibitors (400 and 880ppm) but with eliminating the pre-corrosion period. The results are compared to the data obtained in similar conditions but with a pre-corrosion step (30 min). First, it is important to mention that the specimen surface obtained from the test without corrosion inhibitor features some crystalized corrosion products sitting on top of a flat surface. However, the surface of the specimens exposed to inhibited solution suggests no signs of corrosion product other than some cementite residues. The absence of corrosion product is observed in all the cases

with corrosion inhibitor and with or without pre-corrosion (see Figure 27, Figure 29, Figure 36 and Figure 37). This again strongly indicates that the imidazoline-type inhibitor also inhibits the formation of corrosion product.
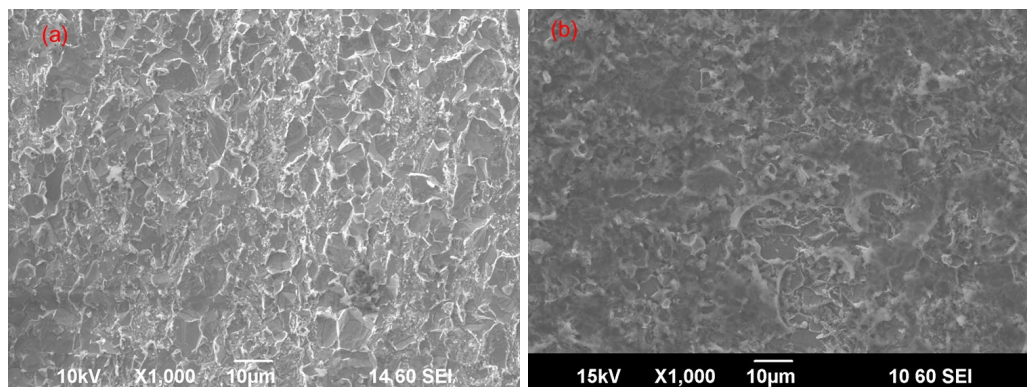
Figure 45. Surface morphology of the specimens exposed to 150°C experiments.(a) With 440ppm imidazoline-type inhibitor; (b) with 880ppm imidazoline-type inhibitor (2-autoclave system with modified procedure)

Figure 46 shows the cross-section images of the specimens retrieved from 150°C experiments in the presence of different amounts of the imidazoline-type corrosion inhibitor and ensuring no pre-corrosion time. A 40μm of corrosion product layer (a mixture of $FeCO_3$ and Fe_3O_4) was found in the absence of corrosion inhibitor (see Figure 37). However, no apparent layer was observed in the cases without pre-corrosion and in the presence of 440 and 880 ppm imidazoline-type inhibitor. Similarly, even with 30 minutes pre-corrosion, no apparent layer was observed after experiments with the presence of the imidazoline-type inhibitor. This finding confirms the absence of corrosion product layers is related to the addition of the imidazoline-type inhibitor.
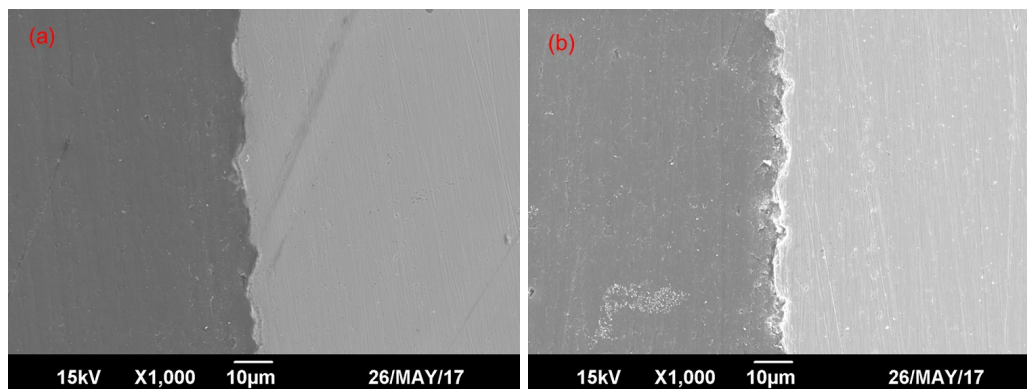
Figure 46. Cross-section images of the specimens exposed to 150°C experiments (a) With 440ppm imidazoline-type inhibitor; (b) with 880ppm imidazoline-type inhibitor. (2-autoclave system with modified procedure)

5.3.7 The Formation of Fe_3O_4 and Its Role on Corrosion Rate

In the experimental part, it was noticed that by solely removing the transient 30 minutes pre-corrosion, the corrosion rate with inhibitor showed some differences; relatively modest at 120°C, more significant at 150°C. This confirms the proposed hypothesis which suggests that the role of Fe_3O_4 is critical to the corrosion process at 150°C. However, it is clear that the presence of inhibitor also had some effect, by limiting the formation of corrosion products. In the absence of pre-corrosion, the effect of inhibitor was more visible. Further discussion is made in this section to better understand the role of magnetite on the corrosion process and to identify the specific role of corrosion inhibitor at 150°C.

In the absence of oxygen, Fe_3O_4 layers are reported to form at elevated temperature in aqueous environment and play an important role in corrosion rate [141,142]. When the Fe_3O_4 layers are formed, solid state diffusion in the Fe_3O_4 layer is the rate-determining step [142]. Generally, when the diffusion of reactants through a

growing oxide scale is the rate determining step, the rate follows a parabolic time law

[142]. Therefore, the measured corrosion rate should also take a parabolic form if the

formation of Fe_3O_4 dominates the corrosion rates, which can be expressed as:

$$(CR - CR_{without\ Fe_3O_4})^2 = kt \tag{42}$$

Where CR is instantaneous corrosion rate, $CR_{without\ Fe3O4}$ is the initial corrosion

rate before the formation of Fe_3O_4, k is related to the diffusion coefficient and

concentration difference of the rate-limiting species and t is time (hour).

Earlier results show that Fe_3O_4 also controls the corrosion rate when a pre-

corrosion step is included whether imidazoline-type inhibitor is present or not. As

indicated earlier, parabolic kinetics usually suggest that the diffusion in the Fe_3O_4 layers

is the rate-determining step. The corrosion kinetics were fitted with a parabolic time law

to investigate if it could match with a typical Fe_3O_4 controlled corrosion process. The

fitted results, shown in Figure 47, indicate that, in the three tested conditions, the

corrosion rates seem to adopt a parabolic time law with relatively similar k values (Table

13). This all suggests that in the tests with pre-corrosion, the rate-determining step has

little to do with the addition of corrosion inhibitor since the corrosion behavior can be

simply explained by the presence of Fe_3O_4.
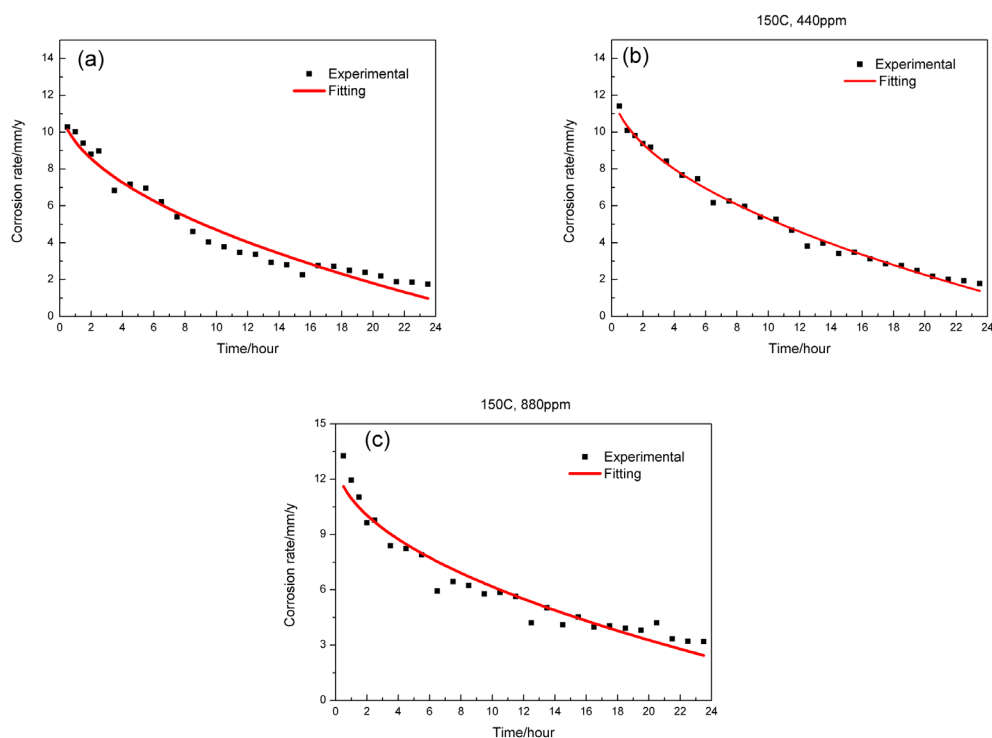
Figure 47. Fitting of corrosion rate with parabolic time law. (a) with 0ppm imidazoline-type inhibitor; (b) with 440ppm imidazoline-type inhibitor; (c) with 880ppm imidazoline-type inhibitor(Black dots are the experimental results and the red lines are the exponentially fitting)

Table 13. Calculated parameters by fitting of corrosion rate at 150°C with parabolic time law

Test conditions	$CR_{without\ Fe3O4}$/mm·y^{-1}	k/mm^2·y^{-1}
150°C, 0ppm imidazoline-type inhibitor	11.69	4.89
150°C, 440ppm imidazoline-type inhibitor	12.64	5.38
150°C, 880ppm imidazoline-type inhibitor	13.18	4.90

5.3.8 The Role of Corrosion Inhibitor at Elevated Temperatures

The experiments performed without pre-corrosion could separate the effect of

corrosion inhibitor from the influence of Fe_3O_4. Actual inhibition efficiency could be

then determined, showing that the temperature effect on the inhibition performance could

be revealed even at 150°C. At lower temperature, it was found that the adsorption of

imidazoline-type inhibitor could usually follow a Langmuir adsorption model. Its

thermodynamic form can be found in Equation (35). The following section investigates if

the same kinetics can be applied at higher temperature.

Additionally, the van't Hoff equation can be used to characterize the effect of

temperature on the adsorption process:

van't Hoff
equation
$$lnK_{eq} = -\frac{\Delta H^0_{ads}}{RT} + Constant \qquad (43)$$

The equilibrium constant K_{eq} is calculated using the procedure highlighted in

Section 4.3.4. Figure 48 presents the results together with data obtained at lower

temperature (Figure 11). If the temperature is the governing factor to the adsorption

behavior, K_{eq} should be linearly related to -1/T over the entire temperature range. The

figure indeed reveals a linear relationship between lnK_{eq} and 1/T. Therefore, it can be

concluded that the adsorption behavior of the imidazoline-type inhibitor holds the same

temperature effect over the entire range of temperature, up to 150°C. This could only be

revealed by minimizing as much as possible the formation of magnetite.
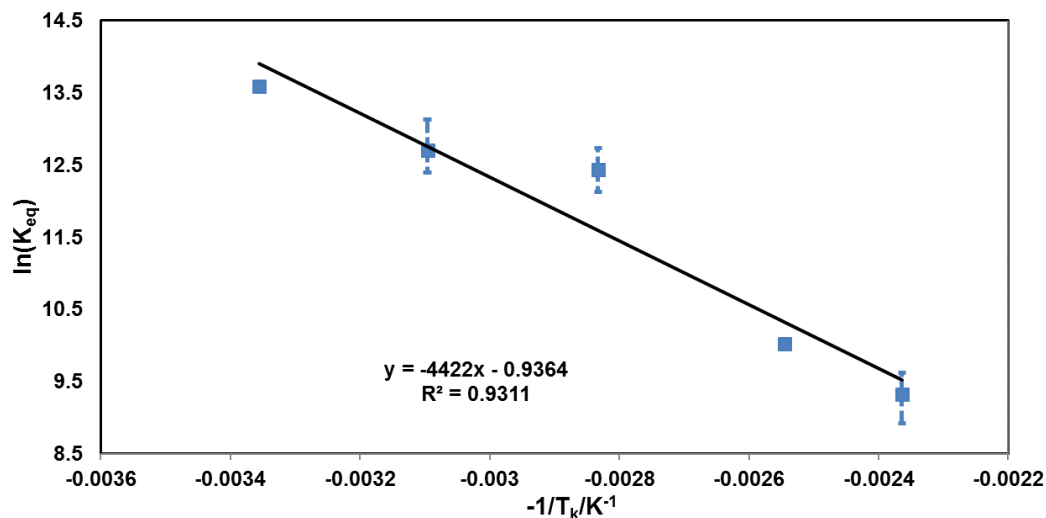
Figure 48. Verification of the effect of temperature on the adsorption behavior of the imidazoline-type inhibitor up to 150°C.

Error bars are taken from values calculated with different concentrations of inhibitor at the same temperatures.

However, it is necessary to point out it was not possible to completely avoid the formation of magnetite elevated temperatures above 120°C, whatever the procedural change implemented. This is because water is the major oxidant for the formation of magnetite and its presence is overwhelming in the tested system. Therefore, it is very important to consider the existence of Fe_3O_4. In addition, it is not practical, in field applications, to avoid any pre-corrosion time before injection of inhibitor. Consequently, the role of Fe_3O_4 needs to be taken into account when making mitigation strategies against corrosion at temperature above 150°C.

5.3.9 Corrosion Production Inhibition Property of the Imidazoline-Type Inhibitor

In the set of work at higher temperatures, it was found that the imidazoline-type inhibitor had a remarkable ability to inhibit corrosion product formation. At elevated temperature, the solubility limit of corrosion product is usually particularly low (see Equation (45) and Equation (45)). Moreover, the iron dissolution rate is also fast and therefore the Fe^{2+} concentration can be high as well. As a result, the formation of corrosion products is significantly favored. For instance, in the conditions tested, the thickness of corrosion product layers is commonly around 30-40μm in the absence of corrosion inhibitor. However, whenever corrosion inhibitor was injected in the system, no apparent corrosion product layer was observed on the surfaces of the retrieved specimens, although the tested conditions were similar. Therefore, it is proposed that the inhibitor showed good inhibition properties against the precipitation of corrosion products.

The water chemistry of the solutions after the high temperature testing is given in Table 14. The high pH and the high ferrous ion concentration all favor the formation of the corrosion product layers. In the absence of inhibitor, a 40μm thick $FeCO_3$ layer formed, accounting for about 2% of the total Fe^{2+} ions released through the corrosion process. In the presence of inhibitor, no corrosion product formed although the bulk ferrous ions concentration was quite similar to the case without inhibitor.

Table 14. Water chemistry of the solution after 150°C experiments without pre-corrosion time in the 2-autoclave system

Test conditions	C(Fe^{2+})/ppm	pH
150°C, 0ppm imidazoline-type inhibitor	140	6.04
150°C, 440ppm imidazoline-type inhibitor	135	6.00
150°C, 880ppm imidazoline-type inhibitor	201	6.11

Here, the ppm is parts per million by mole.

To understand the role of corrosion product inhibition ability of the imidazoline-type inhibitor, the saturation value of the corrosion product at 150°C was evaluated. The formation of iron carbonate goes through Equation (20). The solubility equilibria for Fe$_3$O$_4$ goes through the following reaction:

$$Fe^{2+} + 2Fe^{3+} + 4H_2O \rightleftharpoons Fe_3O_4 + 8H^+ \tag{44}$$
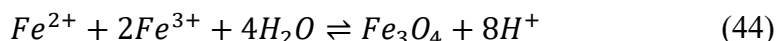
The solubility limit of the FeCO$_3$ and Fe$_3$O$_4$ can be found in the following equations:

$$K_{sp,FeCO_3} = e^{-59.3498 - 0.041377 T_K - \frac{2.1963}{T_K} + 24.5724 log(T_K) + 2.518 I^{0.5} - 0.6571} \tag{45}[143]$$

$$K_{sp,Fe_3O_4} = e^{-\frac{\Delta G_{Fe_3O_4}}{RT_k}} \tag{46}[22]$$

Therefore, the solubility of the iron carbonate (K$_{sp,FeCO3}$) and Fe$_3$O$_4$ (K$_{sp,Fe3O4}$) at different temperatures can be calculated and depicted in Figure 49. Moreover, the saturation values are also calculated at the initial condition (pH=4.3) and the final

condition (pH=6) with the presence of different concentrations of Fe^{2+} and shown in Figure 50. Both $FeCO_3$ and Fe_3O_4 saturation values are much higher than 1 at pH=6.0, which means that the formation of corrosion product is highly favored. Indeed, with corrosion inhibitor, a 30-40μm thick corrosion product layer was formed at higher temperatures (Figure 37 (a)). However, when there was inhibitor present in the system, no apparent corrosion product developed on top of the surface (Figure 37 (b) and (c)). The XRD also confirmed the absence of $FeCO_3$ (Figure 35 (b) and (c)). Although Fe_3O_4 was still observed in the XRD, it is likely very thin (nanometer level) and not detectable by SEM. Therefore, the inhibitor obviously plays a significant role in scaling inhibition.
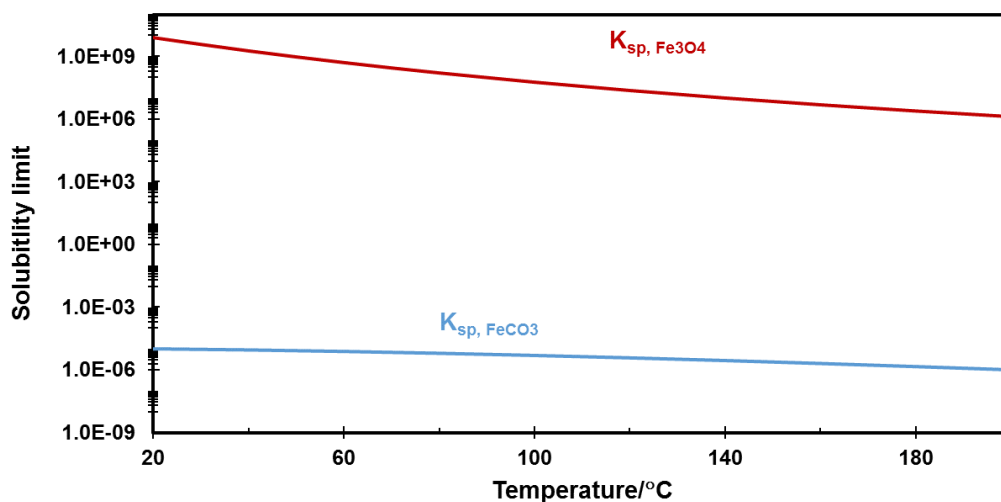
Figure 49. Solubility limit of $FeCO_3$ and Fe_3O_4 at different temperatures.
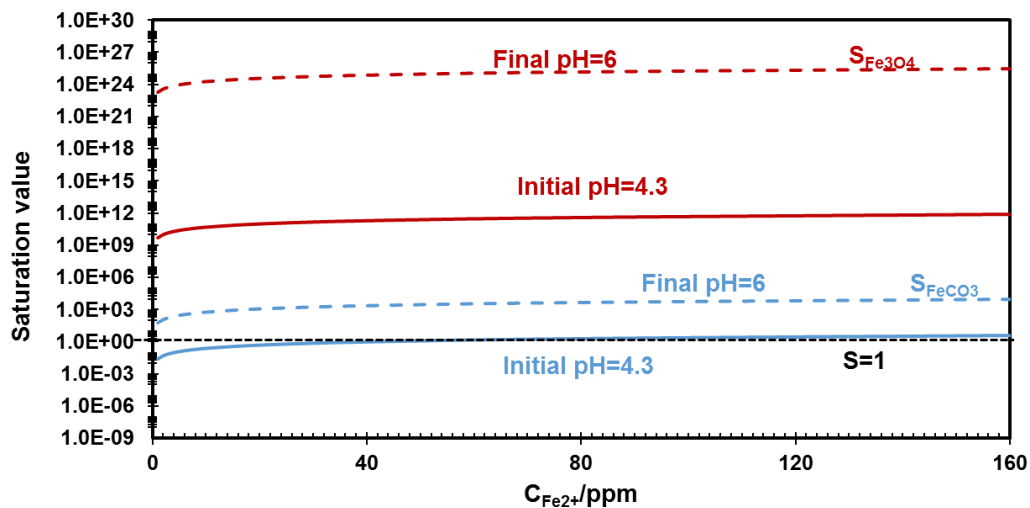
Figure 50. Saturation value of $FeCO_3$ and Fe_3O_4 at 150°C with the presence of different concentration of Fe^{2+}. (p_{CO2}=2bar, Initial pH=4.3, final pH=6, 1wt% NaCl, $Fe^{3+}=10^{-10}mol \cdot L^{-1}$)

The corrosion product/scaling inhibition property is probably due to the imidazoline-type inhibitor absorbing on the growing faces of crystal nuclei and hence preventing the formation of symmetrical crystal. Generally, the process of precipitation requires nucleation sites. Once the concentration of the species (such as Fe^{2+}, CO_3^{2-}) exceeds the saturation level, corrosion products starts to precipitate and form into dense, closed-packed crystals [48]. In the current research, the saturation value was always higher than 1. Therefore, the failure of the formation of dense corrosion product layers is probably because of a lack of nucleation sites. In fact, the inhibitor molecules most likely adsorb on the crystalline faces and hence block additional formation of corrosion products and hence well-structured scales. The scale formed in the presence of scaling inhibitors \has been reported to usually be mushy and soft [77-79]. In the post-processing of the specimens exposed to the imidazoline-type inhibitor, some fragile and loosely

attached residues were also found on the surfaces and could be easily washed away by water and isopropanol. These are likely poorly developed amorphous crystals. As a result, XRD cannot capture the existence of $FeCO_3/Fe_3O_4$ easily.

5.4   Summary

A two autoclave system was developed to shorten the heating up and cooling down time periods of solutions and hence the formation of corrosion products. The two-autoclave system showed many advantages over the more common single autoclave system. The ingress of O_2, the heating up and cooling down period was significantly limited in the new system.

Using the two-autoclave system, the formation of iron carbonate in the uninhibited test was mostly avoided at 120°C. The efficiency of the inhibitor could then be clearly determined at 61%. At 150°C, the rapid formation of Fe_3O_4 could not be prevented and seemed to control the corrosion behavior with or without inhibitor. At this temperature, the presence of inhibitor had no visible effect on the corrosion rate.

In addition, the imidazoline-type inhibitor was also proved to be an effective scaling inhibitor. Whenever there was the presence of the imidazoline-type inhibitor, the formation of corrosion product layers were not observed by SEM, although saturation value was high for the involved water chemistry.

CHAPTER 6: THE ROLE OF THERMAL STABILITY OF THE IMIDAZOLINE-
TYPE INHIBITOR AT ELEVATED TEMPERATURES

6.1   Introduction

In Chapter 4 and Chapter 5, the adsorption behavior and the inhibition

performance of the imidazoline-type inhibitor was examined to verify the first

hypothesis. It was found that the decreased inhibition performance at elevated

temperatures was mostly a result of the desorption being favored, as long as the

formation of Fe_3O_4 was limited. This chapter presents efforts to demonstrate the second

hypothesis, which relates to the role of the inhibitor stability at elevated temperatures.

Methods to evaluate the corrosion inhibitor are required to understand the role of

the thermal stability. Many techniques are applied for the characterization and

determination of the corrosion inhibitor in the field or the laboratory, including visible

spectroscopy, UV-vis spectroscopy, fluorescence, mass spectroscopy, Fourier

transformation infrared (FTIR) spectroscopy, etc. However, these techniques all have

certain limitations in detection capabilities, automation, relative ease of the setup and

operations [144].

Here, UV-vis spectroscopy was used to analyze the inhibitor and determine its

concentration. The spectra of the two inhibitors selected in this study are detectable by

UV-vis spectroscopy [102,145–147]. The absorption peak for the conjugated $N\overset{..}{=}C\overset{..}{=}N$

(characteristic group of the imidazoline ring) is at the wavelength of 232nm [102,147],

and the ammonium group is determined at 203nm [145,146]. In addition, the UV-vis can

be used for the determination of inhibitor concentrations. The relationship between the

analyte concentration and the intensity of the absorption can be found using the Beer-Lambert law [148].

$$Absorbance = \varepsilon c l, \qquad (47)$$

In which, *Absorbance* is the absorbance at a specific wavelength, ε is a constant (with a unit of $(mol \cdot cm)^{-1}$), c is the concentration of materials to analyze (with a unit of $mol \cdot cm^{-3}$), and l is the path length (with a unit of cm). The equation shows that the absorbance of the inhibitor is supposed to be linearly related to the inhibitor concentration if the path length is fixed. Therefore, this relationship is extensively used for determination of analyte concentrations using UV-vis [149–151]. Last but not the least, the measurement of UV-vis is simple and fast. UV-vis measurements usually do not require special treatment for the tested inhibitors before starting. A single measurement usually takes less than 30 seconds. These advantages make the UV-vis method an ideal method to determine the inhibitor concentrations.

In this section, the calibration procedure of the imidazoline-type inhibitor is introduced and its application in determining the role of thermal stability of the imidazoline-type inhibitor at elevated temperature is discussed. The spectra of the imidazoline-type inhibitor at different concentrations in 1 wt.% NaCl solution was measured using UV-vis spectroscopy. The linear relationship between the inhibitor concentration and the absorbance was developed and applied for determining unknown inhibitor concentrations.

6.2 Experimental Procedure

In this set of experiment, an Agilent 8453 UV-visible Spectrometer was used. UV-vis spectroscopy uses a light source range from 200nm (the starting of the UV region) to 1100nm (the end of the visible region). The spectra of the molecule are recorded continuously with changing wavelength. When the wavelength of light corresponds to the amount of energy needed for a molecule to excite, the energy is absorbed and hence yields a peak at this wavelength. The solvents of inhibitors are CO_2 saturated 1 wt.% NaCl. To remove O_2 and simulate the pH saturated with CO_2, the solvent was usually sparged with CO_2 for more than 2 hours before measurements started. After sparging, solutions with different concentrations of inhibitor were prepared by injecting the desired amount of inhibitors into the CO_2 saturated solutions. The inhibitor used here is the imidazoline type inhibitor package (see Table 4).

6.3 Results and Discussion

6.3.1 Determination of the Concentration of the Imidazoline-Type Inhibitor

The spectra of the solutions containing various concentrations of imidazoline-type inhibitor in 1 wt.% NaCl are shown in Figure 51, which show two main peaks. From literature, peak 1 at 203nm is related to the transition of n→σ∗ in the amine group at the side chain of the imidazoline inhibitor molecule [145,146], peak 2 at 232nm is related to the π→π∗ transition in the conjugated N⋯C⋯N group in the imidazoline ring [146,147]. In addition, the shape of the spectra was not changed with higher concentration of inhibitor other than higher absorbance. This suggests that the increase in the concentration does not affect the peak positions.
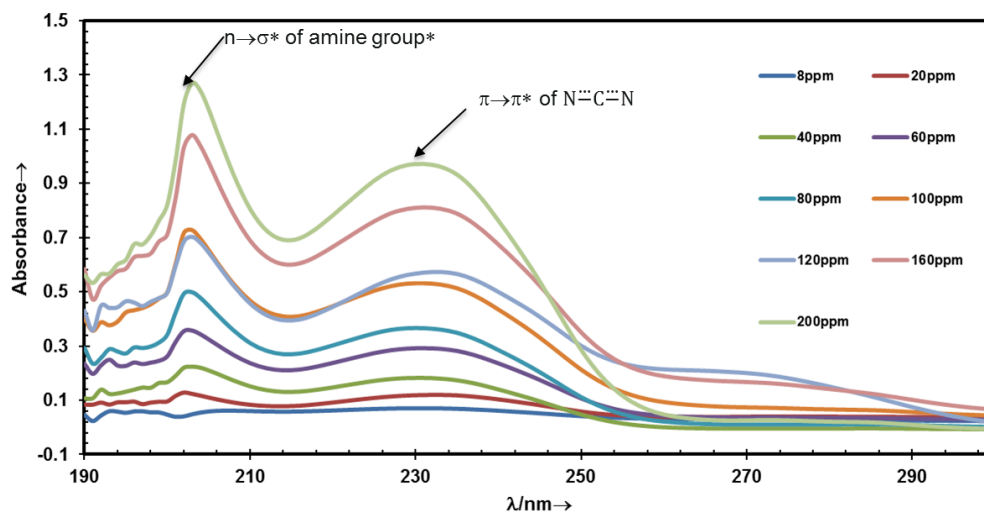
Figure 51. UV-vis spectra of the imidazoline-type inhibitor in 1wt. % NaCl water with various concentration

Furthermore, the linear relationship between the inhibitor concentration and the absorbance was confirmed. Here, the absorption of the peak at 232 nm was selected for the calibration of the inhibitor concentration. The conjugated N⋯C⋯N group is contained in the imidazoline ring and is therefore more representative for the imidazoline-type inhibitor. The absorbance at 232nm *vs.* the inhibitor concentration is shown in Figure 52, which shows that there was a good linearity between the absorbance and the inhibitor concentration ($R^2 > 0.99$). This means that the absorbance of the conjugated group conforms well with the Beer-Lambert law. Therefore, the relationship can be interpreted as:

$$A_{232nm} = 0.0048 \times c + 0.0119 \qquad (48)$$

Here, A_{232nm} is the absorbance at 232nm, and c is the inhibitor concentration with a unit

of ppm. Moreover, the purpose of this work is to develop a way to determine the inhibitor

concentration. Therefore, Equation (48) can be then translated into:

$$c = 208.3 \times A_{232nm} - 2.48 \qquad (49)$$

Therefore, a method that can be used directly for measuring the imidazoline-type

inhibitor is established for the instrumentation that was used. In addition, another two

samples with 48 and 96ppm imidazoline-type inhibitor were prepared to verify whether

this method is valid for specific concentrantions of inhibitor. Their concentrations are

measured through the absorbance of the inhibitor solution determined by UV-vis

spectrocsopy, as shown in Figure 52(see the red points). The measured concentrations

agreed well with the linearity of the calibration line. In conclusion, this method can be

accurate for any concentrations of inhibitors in the calibrated range.
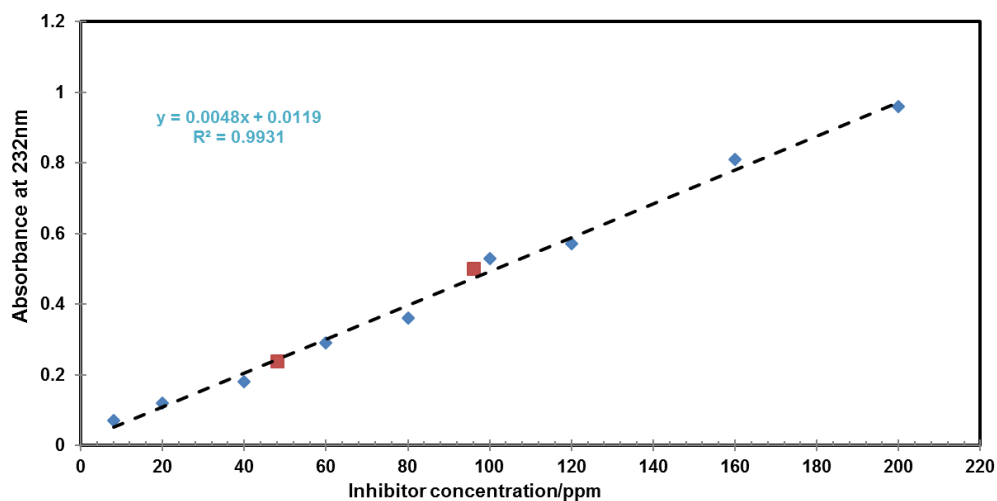
Figure 52. Absorbance at 232nm *vs.* concentration of the imidazoline-type inhibitor
concentration in 1wt. % NaCl solution (Red points are the absorbance of 48ppm and
96ppm inhibitor solutions.)

One more thing that is worthy of discussion is the effectiveness of this method when the concentrations of the inhibitor in the testing solution are out of the calibration range. The Beer-Lambert law usually only describes the absorption behavior of solutions with relatively low amounts of analyte. The validity of Beer-Lambert law has two assumptions: (1) the incident light is monochromatic; (2) the analyte concentration is low enough and the analyte molecules do not interfere each other. When the analyte concentration is high, the molecules start to interact with each other and, therefore, the absorption behavior changes and the Beer-Lambert law no longer applies [152]. Generally, the linearity between the analyte concentration and the absorbance can work when the absorbance is less than 1. Therefore, the calibration was only be verified up to an absorbance lower than 1. However, this does not mean that the higher concentration cannot be measured. The simplest way is to dilute the solution first and then measure the concentration of the diluted solution. In this project, the high concentrations value (concentration is higher than 200ppm) were obtained by diluting solutions.

6.3.2 The Role of Thermal Stability of the Corrosion Inhibitor

The imidazoline-type inhibitor is reported to be unstable at higher temperatures and to hydrolyze into its amide precursor [102,103]. The degradation of corrosion inhibitor might also affect the corrosion inhibition efficiency since the effective inhibitor concentration could be reduced. To evaluate the extent of inhibitor degradation during a test, the concentration of the inhibitor in the 1 wt.% NaCl before and after the experiments were measured and compared. The inhibitor concentration (in M) at the

beginning (C_0) and the end (C_1) of each experiment were measured and recorded as shown in Table 15. Here, a residual inhibitor percentage (δ) was defined as:

$$\delta = \frac{C_1}{C_0} \times 100\% \qquad\qquad (50)$$

Table 15 shows that the residual concentration of the imidazoline-type inhibitor almost did not change over the test at 50°C and 80°C. This suggests that the inhibitor did not degrade at these temperatures. However, at 120°C and 150°C, there was a significant change of the inhibitor concentration before and after experiments. In addition, δ was found to be similar in the two-autoclave system, at around 50-60%. Apparently, there was a change of the active component (imidazoline-type) of the corrosion inhibitor concentration at higher temperatures.

Table 15. Measured imidazoline-type inhibitor concentrations before and after experiments.

Test conditions	Initial concentration(C_0) /ppm	Final concentration(C_1) /ppm	δ/%
50°C, 44ppm	32	31.8	99
80°C, 88ppm	78	77.5	99
120°C, 440ppm	257	127	49
150°C, 440ppm	309	194	63
150°C, 880ppm	614	295	48

In addition, some black oily residue was found on the autoclave wall after the experiments. This residue was insoluble in water, so UV-vis spectroscopy was not readily

able to identify this species. Therefore, Fourier transform infrared (FTIR) spectroscopy

was used to identifying components of the oily residue. The FTIR spectrum is shown in

Figure 53. Two peaks associated with the amide are observed. Peak 1 at around 1645

cm^{-1} and peak 2 at 1556 cm^{-1} stand for the stretch (st) mode of the C=O bond and the

stretch and symmetric (st-sy) mode of N-C=O bond [146], respectively, both of which

only exist in the amide. It is worthy to mention that in the literature [102], for a

imidazoline-type inhibitor, there is a peak at 1610 cm^{-1} which represents the stretch mode

of C=N. However, this peak was not observed in the spectrum. Therefore, it can be

concluded the oily residue likely consisted of amide precursor and no molecules

possessing an imidazoline structural moiety. Combined with the fact that 40-50 %

inhibitor was lost over the tests, these amides were likely hydrolyzed from the

imidazoline-type inhibitor.
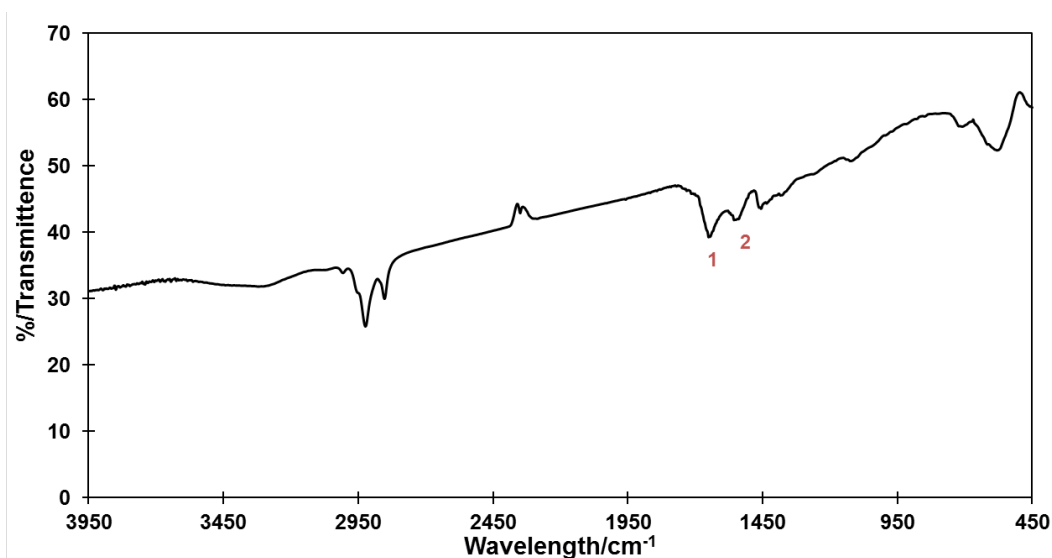
Figure 53. FTIR spectrum of the retrieved oily residual. (Peak 1: stretch mode of the C=O bond; Peak 2: stretch and symmetric mode of N-C=O)

From the above results, it can be concluded that the imidazoline-type inhibitor was partially hydrolyzed into its amide precursor at high temperature. Due to its low solubility in water, the amide accumulated on the wall of the autoclave. About 40-50% of the imidazoline inhibitor was lost due to the thermal degradation. This also means that there was still plenty of 'active' imidazoline inhibitor left in the system. However, at 150°C, the injection of inhibitor still did not change the corrosion rate when there was pre-corrosion. This means that the failure of the inhibition at higher temperatures (150°C) was not entirely due to the degradation and hence the depletion of imidazoline-type inhibitor. Consequently, this finding confirmed again that the ineffectiveness of inhibitor at 150°C with pre-corrosion was highly likely a result of the formation of Fe_3O_4.

6.4   Summary

A methodology was developed for to determine the concentration of the imidazoline-type inhibitor in 1wt. % NaCl solution using UV-vis spectroscopy. Any concentration of inhibitor can be determined using a linear relationship established through calibration.

The imidazoline-type inhibitor did not degrade at lower temperatures (below 80°C), but degraded into its amide precursor at 120°C and 150°C. However, only about 40% to 50% of the inhibitor was lost due to the hydrolysis of imidazoline. Consequently, the failure of inhibition at 150°C was not entirely due to the degradation of imidazoline-type inhibitor.

CHAPTER 7: INHIBITION PROPERTIES OF THE QUAT-TYPE INHIBITOR AT
MEDIUM TEMERATURE RANGE (25°C-80°C)

7.1   Introduction and Objectives

The objectives of this chapter are dedicated to the investigation of the

adsorption/inhibition behavior of a quat-type inhibitor at relatively low temperatures

(25°C-80°C). In this chapter, the same methodology developed to study the inhibition

and adsorption behavior of the imidazoline-type inhibitor was applied to this quat-type

inhibitor. As in Chapter 4, the performance of the quat-type inhibitor is first discussed in

terms of its adsorption behavior and its inhibition performance at relatively low

temperature. In addition, the differences in the inhibition properties of the two types of

inhibitors are introduced.

7.2   Experimental Methodology

7.2.1 Equipment and Procedure

QCM Measurement

The equipment used for studying the quat-type inhibitor is exactly the same as for

the imidazoline-type inhibitor, as shown in Figure 3. The setup and testing parameters

details are also the same and can be found in Chapter 4. The procedure, however, is

slightly different for the quat-type inhibitor. This is due to the magnitude of the frequency

change of the quartz crystals observed with the quat-type inhibitor, which was at least 10

times lower than for the imidazoline-type inhibitor (10-60Hz *vs.* 300-400Hz,

respectively). In the initial procedure, the imidazoline-type inhibitor was injected into the

solution prior to the insertion of the QCM holder in solution. The QCM measurements

were started in the gas phase, just above the liquid phase, and were continued during

immersion of the probe in the bulk liquid phase. Typically, the QCM measures a large change of resonant frequency due to the change in medium (air/liquid). The value of the change is around 700Hz. In the case of the imidazoline-type inhibitor, the subsequent change of frequency due to the adsorption of inhibitors (300-400Hz) could still be clearly measured. However, for the quat-type inhibitor, this was not the case. Consequently, the procedure was modified to eliminate the large change in frequency due to the immersion from air to liquid and to better highlight the response due to the adsorption of quat-type inhibitor. In this case, the QCM holder was inserted into the solution first, before any measurement was taken and the inhibitor was injected later on. The readings only started after the water baseline was stable (no apparent increasing or decreasing trend with, the magnitude of the frequency change not higher than ±2Hz). The inhibitor was then injected into the solution after a few minutes. Following this procedure, the adsorption behavior of the quat-type inhibitor could be better defined.

Corrosion Measurements

The setup and the procedure used for the corrosion measurements in the presence of quat-type is also the same as for the imidazoline-type inhibitor and the details can be found in 4.2.1.

7.2.2 Tested Inhibitor

The tested quat-type inhibitor is an alkylbenzyldimethylammonium chloride. Its structure is given in Figure 54. The inhibitor is also a package (as for the imidazoline-type inhibitor), and its composition is given in Table 16. The composition is relatively simple, at least compared to the imidazoline-type inhibitor. This is because the quat-type

inhibitor is a polar organic salt, which is already relatively soluble in water. Therefore, no additional solvent is required in the package. The concentration of the active component (24 vol. %) is the same for the imidazoline-type inhibitor, making comparison ppm by volume for ppm by volume easier.
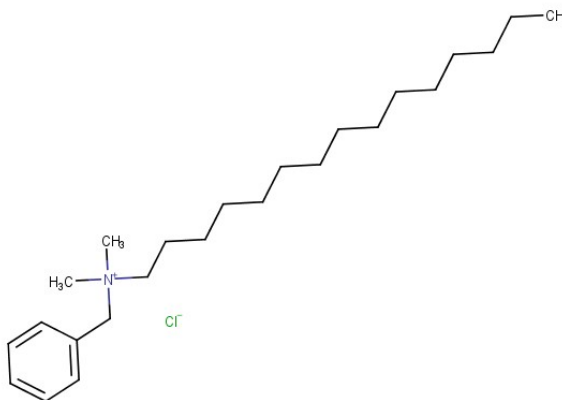
Figure 54. General structure of the alkylbenzyldimethylammonium chloride inhibitor

Table 16. Package information of quat-type inhibitor

	Alkylbenzyldimethylammonium chloride	water
Percentage	24%	76%

7.2.3 Test Matrix

Experiments related to quat-type inhibitor were conducted at several temperatures and concentrations. The test matrices of QCM measurements and corrosion experiments are given in Table 17 and Table 18. The selected inhibitor concentrations were different

at different temperatures, unlike the ones used for the imidazoline-type inhibitor. This is because the concentration of quat-type inhibitor required for delivering adequate performance was much higher at higher temperatures. Therefore, it is necessary to use different concentrations of inhibitor at different temperatures to reveal its inhibition performance.

Table 17. Test matrix for QCM experiments of the quat-type inhibitor

Description	Parameters		
Temperature/°C	25	50	80
Electrolyte	1wt. % NaCl solution saturated with CO_2		
Inhibitor	Quat-type inhibitor		
Inhibitor concentration/ppm	Concentration varies at different temperature (from 60ppm to 720ppm)		
Material	5MHz polished gold-coated crystal		
pH	4		
Stirring bar speed/rpm	200		

Table 18. Test matrix for corrosion measurements of the quat-type inhibitor

Description	Parameters		
Temperature/°C	25	50	80
Electrolyte	1wt. % NaCl solution saturated with CO_2		
Inhibitor	Quat-type inhibitor		
Inhibitor concentration/ppm	Concentration varies at different temperature		
Material	API 5L X65		
pH	4		
Stirring bar speed/rpm	200		
Techniques applied	LPR, OCP		

7.3   Results and Discussion

7.3.1 Adsorption Behavior of the Quat-Type Inhibitor from 25°C to 80°C

The adsorption behavior was studied using the QCM at 25°C, 50°C, 80°C and shown in Figure 55, Figure 56 and Figure 57, respectively. However, a number of issues rendered the analysis of the collected data particularly difficult.

- As mentioned above, the changes in the resonant frequency due to the presence of the quat-type inhibitor were between 0 and 60Hz, with most of the measurements obtained in the range of 15-30Hz. This was much smaller than the data obtained with the imidazoline-type inhibitor (300-400Hz). In addition, the resonant frequency fluctuations in the baseline (before the injection of inhibitor) were in the range of 5-15Hz (see Appendix C), which could also compromise the measurements that caused by the adsorption of quat-type inhibitor.

- Although a relatively clear change of frequency could be measured with the addition of inhibitor, the repeatability of the results was poor in general. Numerous repeats were made using different crystal substrates and by maintaining the potential at a fixed value. None of the attempts could yield satisfactory results in terms of repeatability. The reason behind this issue could be due to several factors:

  o The low range of frequency change which was closed to the fluctuations in the liquid phase. (see Appendix C)

  o The mechanical properties of the adsorbed inhibitor films may not fit the requirements in term of film rigidity. (see Appendix B)

Yet, the adsorption of the quat-type inhibitor could be determined, at least

qualitatively. Observing first the initial response of the QCM measurement (Figure 58), a

relatively sharp increase in resonant frequency (5-10Hz) was always measured after the

injection of inhibitor. This fast process is not likely a result of the adsorption of inhibitor.

A closer examination of this phenomenon shows that it occurred usually within the first

30 seconds of measurements right after the inhibitor injection, with the resonant

frequency increasing linearly with respect to time (see the black dotted line in Figure 58).

This behavior is not a typical adsorption process, which often displays slower kinetics.

Anyhow, the slope of the initial increase seems still to be dependent on the inhibitor

concentration. Consequently, this could be related to the change in fluid properties

(viscosity and density) of the solution. Shifts in the resonant frequency can be induced by

changes in the fluid properties according to Equation (51):

$$\Delta f_{solution} = -f_U^{3/2}(\frac{\rho_L \eta_L}{\pi \rho_q \mu_q})^{1/2} \qquad (51)$$

Where, $\Delta f_{solution}$ is the frequency change induced by the solution itself, f_U is the frequency

of the unloaded crystal (~5MHz), ρ_q and μ_q are the density (2.648g·cm^{-3}) and the shear

modulus (2.947×10^{11} g·cm^{-1}·s^{-2}) of the quartz, ρ_L (with unit of g·L^{-1}) and η_L (unit of m^2·s^{-1}) are the solution density and viscosity of the liquid in contact with the crystal,

respectively. For a gold-coated, 5MHz polished crystal, the frequency shift in DI water is

usually around 715Hz [153]. Since corrosion inhibitors are usually surfactants, they can

certainly affect the density and especially the viscosity of the solution and thereby cause a

shift in the frequency.

Past the first few seconds of measurements, the QCM measurement is more typical of adsorption processes with a relatively slow and non-linear increase followed by stabilization in the measured value. Yet, as mentioned earlier, repeatability of the results was problematic and adsorption trends versus inhibitor concentration were difficult to extract.
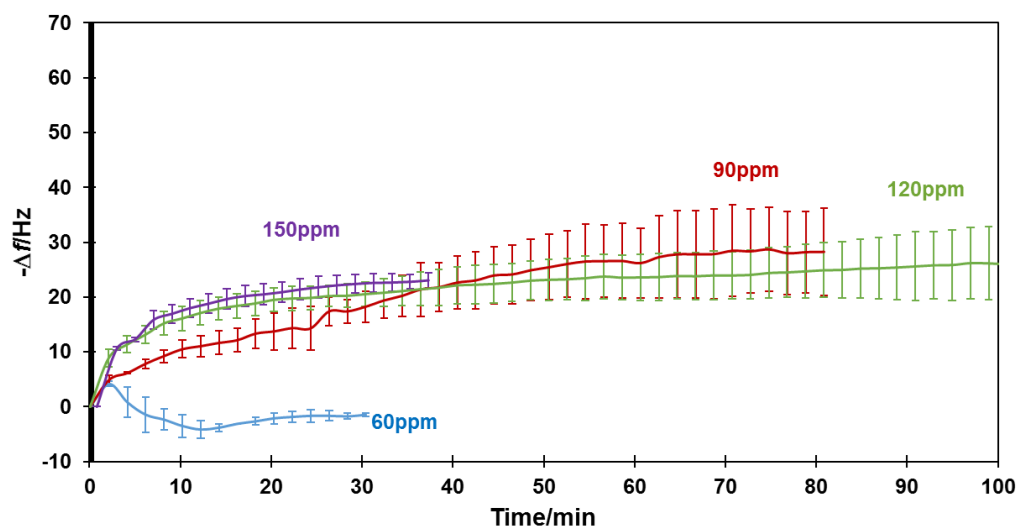
Figure 55. Adsorption of the quat-type inhibitor at 25°C. (1 wt. % NaCl, pH=4.0, p_{CO2}=0.97bar; 200 rpm, 5 MHz polished gold-coated crystal)
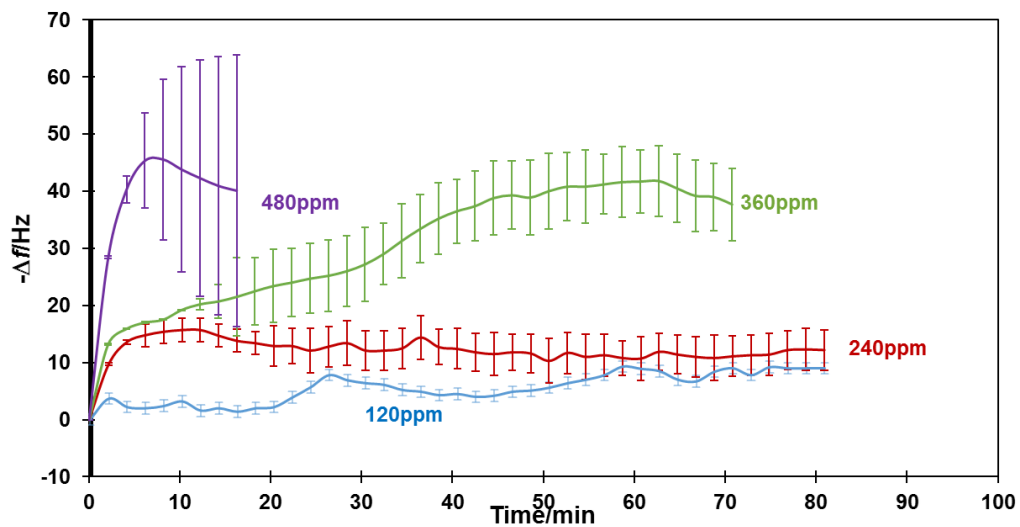
Figure 56 Adsorption of the quat-type inhibitor at 50°C. (1wt. % NaCl, pH=4.0, p_{CO2}=0.80bar; 200 rpm, 5 MHz polished gold-coated crystal)
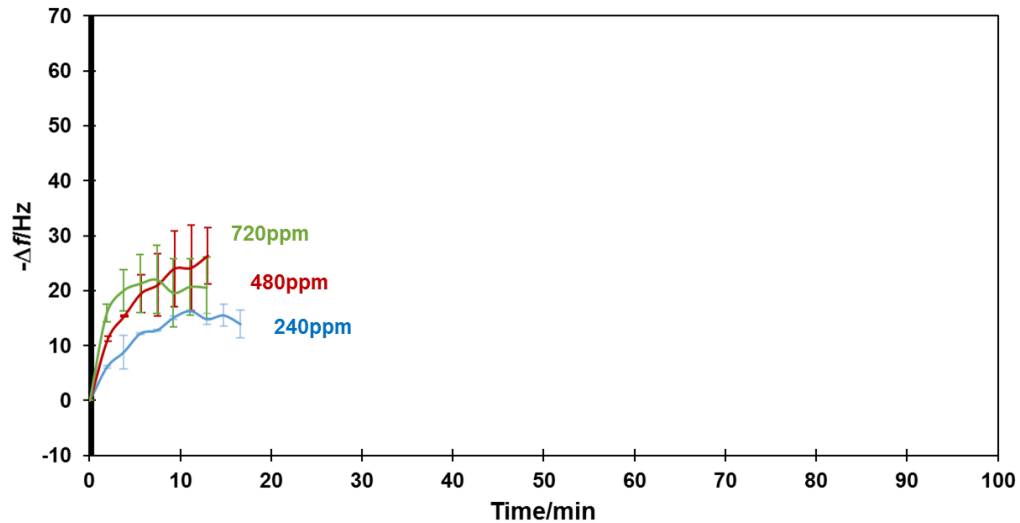
Figure 57. Adsorption of the quat-type inhibitor at 80°C. (1wt. % NaCl, pH=4.0, p_{CO2}=0.5 bar; 200 rpm, 5 MHz polished gold-coated crystal)
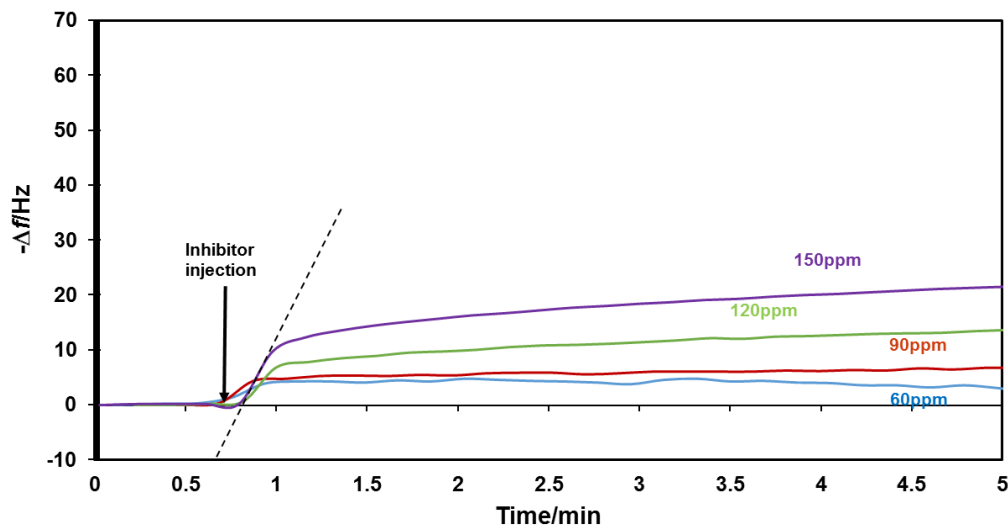
Figure 58. The frequency change at 25°C in the first few minutes. (1wt. % NaCl, pH=4.0, p_{CO2}=0.97 bar; 200 rpm, 5 MHz polished gold-coated crystal)

Nevertheless, an effort was still made to determine the equilibrium frequency change caused by the adsorption of inhibitor following the same methodology as for the imidazoline-type inhibitor. The initial shift in resonant frequency was deducted from the final equilibrium frequency measurement since this was not related to the adsorption. The equilibrium frequency at different temperatures and concentrations are given in Figure 59. Obviously, the large error bars displayed in Figure 55, Figure 56 and Figure 57 made the exercise difficult and led to significant scatter in the results.

While those results were not accurate enough to directly determine the kinetics of adsorption, they can still provide some important information about the adsorption process. Firstly, the frequency change (related to the adsorbed mass) of the quat-type inhibitor is much smaller compared to the imidazoline-type inhibitor. The maximum equilibrium frequency change induced by the adsorption of inhibitor and the molecular

weight of the two inhibitor are summarized in Table 19. The corresponding adsorbed mass, calculated using Sauerbrey equation (Equation (24)), are also displayed although it is understood that this equation may not be applicable as discussed in Chapter 3 and in the Appendix B. Despite the molecular weight of the two molecules being close, the maximum frequency change caused by the adsorption of quat-type inhibitor at equilibrium is an order of magnitude lower than what was measured for the imidazoline-type inhibitor. Secondly, higher dosage of inhibitor was required to achieve the maximum frequency change at elevated temperatures. For example, 20Hz was the maximum frequency change obtained at 25°C and it was achieved at 90ppm of corrosion inhibitor. At 50°C, the maximum frequency change was also 20Hz but it was obtained after injection of 360ppm of quat-type inhibitor. Finally, 720ppm of inhibitor was still not sufficient to generate a 20Hz frequency change at 80°C. This indicates that the desorption of the quat-type inhibitor is favored by higher temperatures. Although this behavior seems to be relatively clear despite the poor repeatability of the QCM measurements, corrosion inhibition experiments are needed to validate this finding.
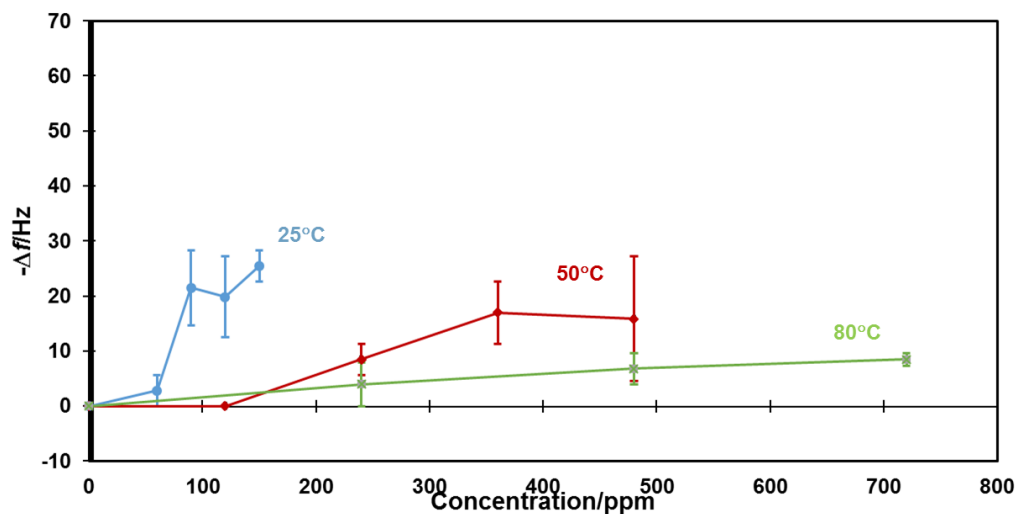
Figure 59. Equilibrium frequency *vs.* the quat-type inhibitor concentrations at different temperatures. (1 wt.% NaCl, pH=4.0, 200 rpm, 5 MHz polished gold-coated crystal)

Table 19. A comparison between the adsorption properties of the imidazoline and quat-type inhibitor

	Imidazoline-type inhibitor	Quat-type inhibitor
Max frequency change/Hz	350	30
Corresponding mass/$\mu g \cdot cm^{-2}$	6.2	0.5
Molecular weight/ $g \cdot mol^{-1}$	359	352.5

7.3.2 Corrosion Inhibition Performance of the Quat-Type Inhibitor from 25 ℃ to 80 ℃

The inhibition performance of the quat-type inhibitor was investigated at 25°C, 50°C and 80°C, and the results are shown in Figure 60, Figure 61 and Figure 62, accordingly. The quat-type inhibitor exhibited excellent inhibition performance at 25°C.

With the injection of 60ppm quat-type inhibitor, corrosion rates quickly reduced to

0.4mm·y^{-1} over the first two hours of exposure and stabilized around 0.15mm·y^{-1} after 10

hours. Similarly, with the injection of 90ppm, 120ppm and 150ppm inhibitor, the

corrosion rates decreased to 0.06, 0.06 and 0.09mm·y^{-1} respectively. This 'quick drop'

followed by 'stabilization' behavior is quite similar to what was observed with the

injection of imidazoline-type inhibitor (Figure 12, Figure 13 and Figure 14).
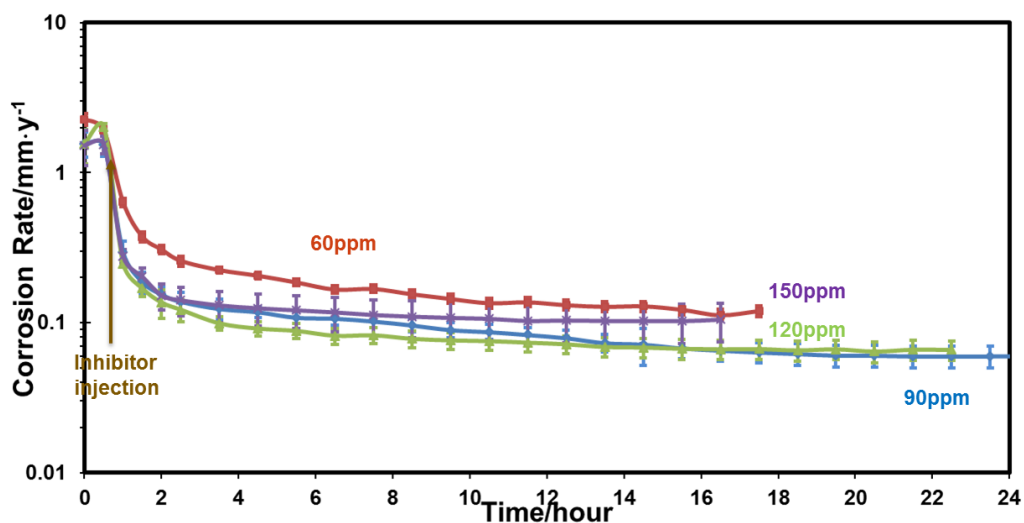
Figure 60. Corrosion rates with the injection of different amount of quat-type inhibitor at 25°C. (1 wt.% NaCl, pH=4.0, X65 mild steel; B=23mV/decade)

However, at 50°C, the inhibition ability of the quat-type inhibitor was

significantly reduced. The injection of 90ppm and 120ppm corrosion inhibitor could not

provide any protection at all, as the corrosion rate basically did not change with the

addition of the inhibitor. To determine whether the inhibitor could work at this

temperature, higher dosages of inhibitor were added. The presence of 240ppm and

360ppm inhibitor did slightly reduce the corrosion rates to 2.8 mm·y^{-1} and 1.1 mm·y^{-1}, respectively. Eventually, 480 ppm of inhibitor were necessary to decrease the corrosion rate to 0.14 mm·y^{-1}. As a comparison, only 60ppm inhibitor were required to achieve the same results at 25°C. Clearly, the inhibition performance of the quat-type inhibitor was significantly weakened at 50°C.
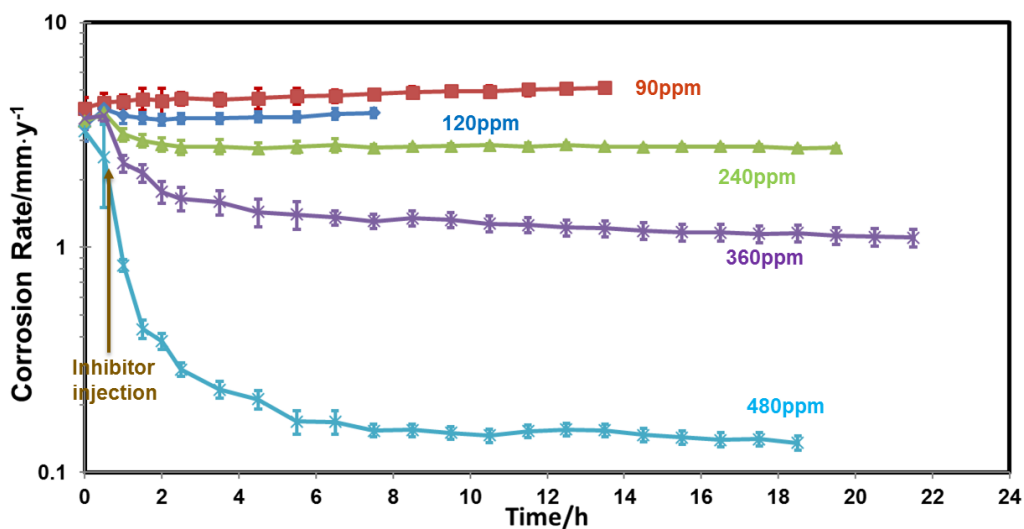
Figure 61. Corrosion rates with the injection of different amount of quat-type inhibitor at 50°C. (1 wt.% NaCl, pH=4.0, X65 mild steel; B=23mV/decade)

The performance of the quat-type inhibitor was even worse at 80°C. There was no significant change of corrosion rate even with the addition of 720ppm of the quat-type inhibitor. Figure 62 shows that the corrosion rate basically did not change over the tested period, no matter what concentrations of inhibitor (120ppm-720ppm) were introduced. This behavior suggests that the inhibitor was completely ineffective at 80°C.
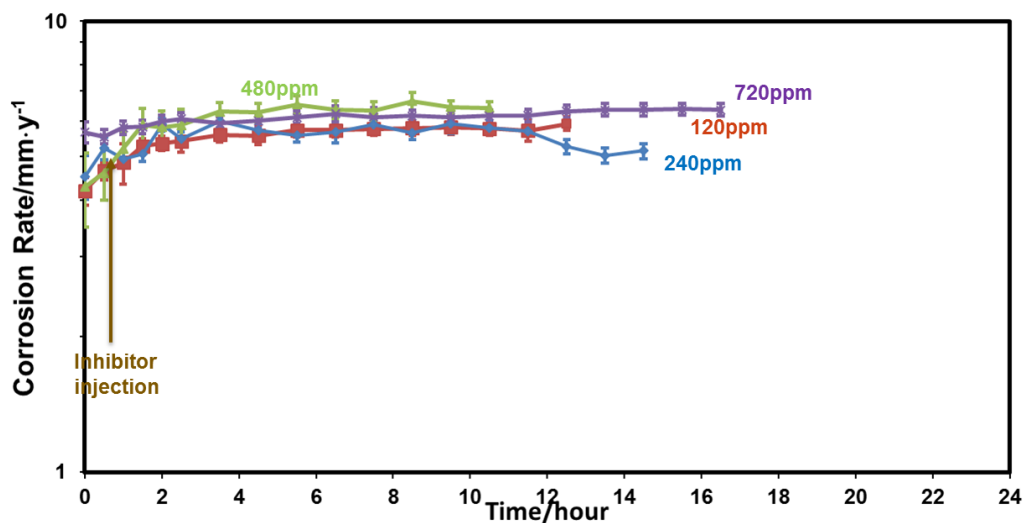
Figure 62. Corrosion rates with the injection of different amount of quat-type inhibitor at 80°C. (1wt. % NaCl, pH=4.0, X65 mild steel; B=23mV/decade)

The inhibition efficiency of the corrosion inhibitor was calculated based on Equation (23) and the values at different temperatures are given in Table 20. The inhibition efficiency usually increased with higher concentration of inhibitor at the same temperature. The performance of inhibitor also decreased with temperature. At 25°C, 120ppm inhibitor could provide 97% protection against corrosion, however, this concentration of inhibitors showed no protection at 50°C or at 80°C. In addition, no inhibition was observed at 80°C even with 720ppm quat-type inhibitor. This behavior suggests that the performance of quat-type inhibitors are critically dependent on temperature.

Table 20. Inhibition test results with the quat-type inhibitor from 25°C to 80°C

Temperature /°C	Inhibitor concentration/ppm	Initial corrosion rate/ mm·y^{-1}	Final corrosion rate/ mm·y^{-1}	Localized corrosion	Inhibition efficiency
25	60	2.1	0.12	No	94%
	90	1.55	0.06	No	96%
	120	1.8	0.06	No	97%
	150	1.53	0.10	No	94%
50	90	4.2	5.0	No	-
	120	3.9	3.9	No	-
	240	3.9	2.8	No	28%
	360	3.9	1.1	No	72%
	480	3.8	0.14	No	96%
80	120	4.8	5.8	No	-
	240	4.9	5.10	No	-
	480	4.7	6.42	No	-
	720	4.2	6.38	No	-

Here, '-' suggests that the inhibition efficiency is not available. The reason could be there was no inhibited corrosion rate.

The observed dependence of temperature also follows the trend observed in the adsorption study using QCM. As an example, a high concentration of inhibitor (240ppm and above) was required to induce a measurable change in resonant frequency at 50°C (Figure 56) However, at 25°C, only 90 ppm inhibitor was necessary to generate measurable QCM response. At 80°C, the frequency change was in general much smaller (only a maximum of 10Hz) in comparison to what was observed at 25°C and 50°C

(30Hz). These observations all indicate that higher temperatures favor the desorption of the quat-type inhibitor and lead to lower performance.

7.3.3 The Role of Temperatures on the CMC of Quat-Type Inhibitor.

The role of CMC of the quat-type inhibitor on the adsorption behavior and inhibition performance is investigated in this part at different temperatures. The change in surface tension with concentrations at 25°C is shown in Figure 63. The surface tension first decreased linearly from 52 to 33 mN·m^{-1} as the concentration increased and then remained constant even as more inhibitor was added (up to 400ppm). According to the definition of CMC (Figure 17), the CMC value of the quat-type inhibitor at 25°C is determined to be 130±5 ppm. This value is in agreement with corrosion inhibition measurement which show that inhibition efficiency did not change past 120ppm of inhibitor. In general, the inhibition performance is expected to increase with inhibitor concentration for values below the CMC. The inhibition efficiency should remain unchanged for inhibitor concentration above the CMC because it was assumed that the surface is optimally covered with inhibitor at this point.
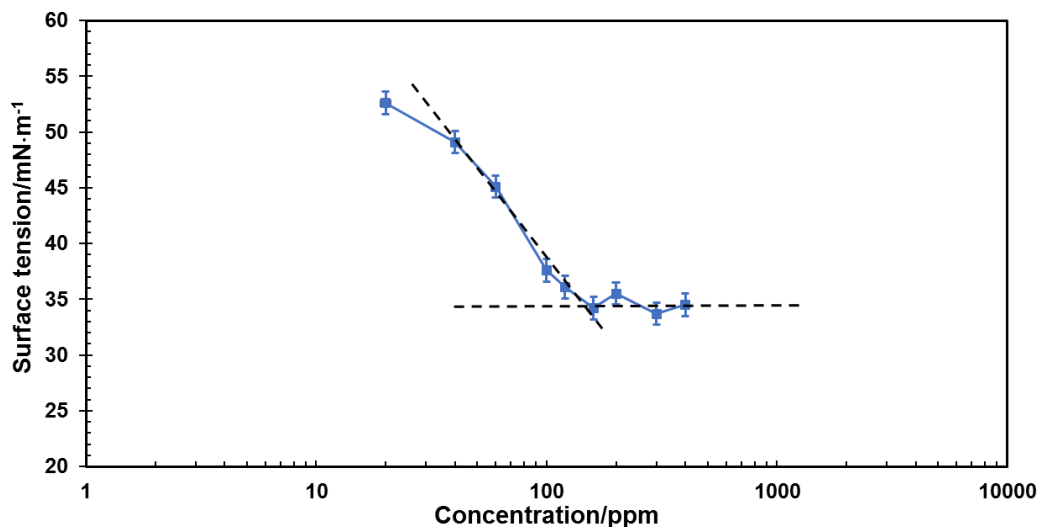
Figure 63. Surface tension *vs.* the quat-type inhibitor concentration at 25°C in 1 wt.% NaCl solution

However, the CMC was also greatly affected at elevated temperatures. The changes of surface tension with inhibitor concentration at 50°C and 80° are shown in Figure 64 and Figure 65, respectively. Results shows that the CMC values of the quat-type inhibitor at 50°C and 80°C are 375±5 and 495±5 ppm, respectively. The CMC value at 50°C agrees with the minimum effective concentration of the inhibitor at 50°C (480ppm) measured during the corrosion inhibition tests (Figure 61). Therefore, a link could be established between the lack of inhibitor performance and increase in the CMC at elevated temperatures, at least up to 50°C. However, this possible correlation between optimum inhibitor concentration and CMC does not seem to hold at 80°C. No protection was observed at 80°C even up to 720ppm. Consequently, further investigations were performed to find the reason of inhibition failure of the quat-type inhibitor at 80°C.
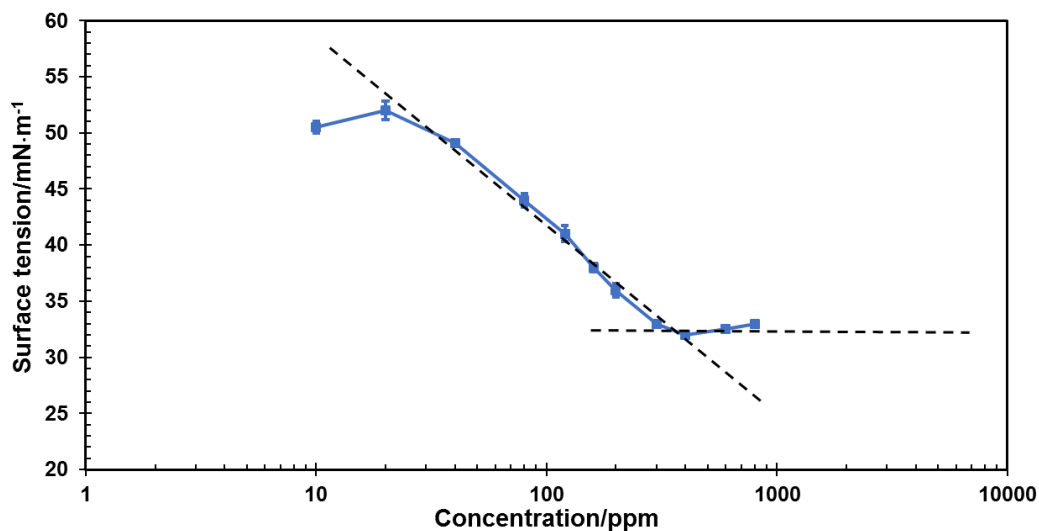
Figure 64. Surface tension *vs.* the quat-type inhibitor concentration at 50°C in 1 wt.% NaCl solution
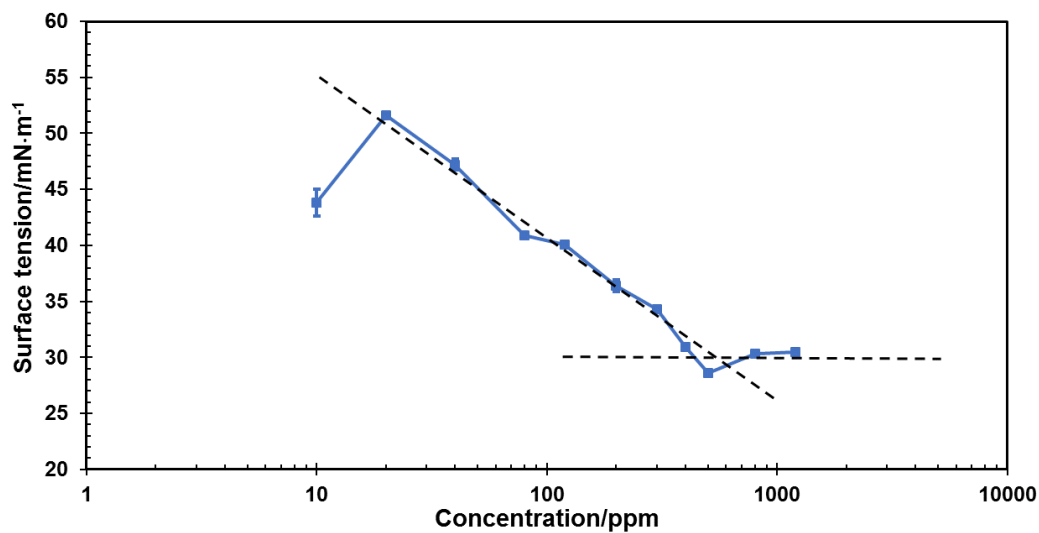
Figure 65. Surface tension *vs.* the quat-type inhibitor concentration at 80°C in 1 wt.% NaCl solution

One possible explanation for the complete loss in inhibition efficiency at 80°C could be related to the change of planar density of the adsorbed molecules. The surface

areas per molecule of the quat-type inhibitor at 25°C, 50°C and 80°C are calculated and

shown in Table 21. The area per molecule is calculated through the following equation:

$$a = \frac{10^{20}}{N_{avog}\Gamma} \qquad (52)\ [154]$$

where a is the surface per molecule with the unit of Å^2·molecule^{-1}. N_{avog} is Avogadro

constant (6.02×10^{23} mol^{-1}), Γ is the surface excess (mol·m^{-2}) that can be calculated

through Equation (41). For ease of comparison, the area per molecule of the imidazoline-

type inhibitor is also listed in Table 21. To validate the calculated values, the surface

areas of the imidazoline-type and quat-type inhibitor are also determined using molecule

footprint method that generated using Avagadro software. The estimated surface areas of

the imidazoline-type inhibitor and the quat-type inhibitor using footprint methods are

28Å^2 and 54Å^2, respectively. These values agree well with the values obtained using

Equation (52). Table 21 shows that the 'a' value of quat-type inhibitor increases from 36

to 107 Å^2·molecule^{-1} as the temperature is increased from 25°C to 80°C. This means that

the surface area per molecule increased three times over the tested range of temperatures.

This significant change might explain why inhibition failed at 80°C. The performance of

inhibitor is critically dependent on the adsorptive behavior of the inhibitor. A low 'a'

value means that the inhibitor molecules are closely packed at interfaces. This is the case

for both imidazoline and quat-type inhibitors at low temperatures. An increase of the 'a'

value of the quat-type inhibitor with temperatures suggests that the quat-type inhibitor

molecules lose their closely packed structures. According to Table 21, the compactness,

or in other words, the intermolecular distance for quat-type inhibitors is much larger at

80°C compared to at 25°C or 50°C. As a result, corrosive species can more easily diffuse to the substrate surfaces at higher temperatures, even though the inhibitor concentration is at or above CMC value.

In comparison, it can be seen that the 'a' value of the imidazoline-type inhibitor only decreased 20% (28 to 22Å^2·molecule^{-1}) over the tested temperatures. Therefore, the distance of the inhibitor molecules did not change significantly and the molecular arrangement remained closely packed. As a result, the inhibitor could still provide significant protection against corrosion at 80°C, because the imidazoline-type inhibitor retained its arrangement on the surfaces at 80°C, as long as enough inhibitor is available.

Table 21. Measured surface per molecule of the quat-type and imidazoline-type inhibitor at 25°C and 80°C

	Imidazoline-type inhibitor	Quat-type inhibitor
Surface area per molecule at 25°C/Å^2·molecule^{-1}	28	36
Surface area per molecule at 50°C/Å^2·molecule^{-1}	29	52
Surface area per molecule at 80°C/Å^2·molecule^{-1}	22	107

7.4   Summary

The adsorption of the quat-type inhibitor on gold-coated crystals was studied using QCM. Although there were difficulties in obtaining repeatable results, the study hinted that desorption of the quat-type inhibitor was favored with increasing temperatures was observed.

The quat-type inhibitor showed excellent corrosion inhibition performance at 25°C. However, the inhibition performance of the quat-type inhibitor was significantly reduced at higher temperature. Higher concentrations of inhibitor were required to achieve ideal inhibition performance at 50°C. No inhibition was observed at 80°C, even at 720ppm of inhibitor.

The ineffectiveness of the quat-type inhibitor at 80°C could probably be related to the predicted increase in intermolecular spacing on the substrate surface at higher temperatures. In comparison, the intermolecular spacing of the imidazoline-type inhibitor molecules was not significantly affected by temperature. The observation was reflected in the corrosion inhibition properties of the imidazoline-type inhibitor which were still retained at 80°C.

CHAPTER 8: STUDY OF INHIBITION MECHANISM OF THE QUAT-TYPE
INHIBITOR AT ELEVATED TEMPERATURES

8.1   Introduction and Objectives

The performance of the quat-type inhibitor at elevated temperature (120°C and 150°C) is investigated in this chapter. At lower temperatures, the quat-type inhibitor displayed corrosion mitigation properties that were very sensitive to temperatures (Chapter 7). Consequently, the performance of this inhibitor is fully expected to be limited at even higher temperatures. However, experiments were performed anyway since the goal of this work is to better understand the mechanisms of corrosion inhibition at higher temperatures (as opposed to identifying an effective inhibitor formulation). Moreover, based on the results obtained with the imidazoline-type inhibitor, this investigation should also provide more evidence on the essential role of magnetite in high temperature corrosion inhibition.

Therefore, in this chapter, the performance of the quat-type inhibitor at elevated temperature is investigated using the same methodology as for the imidazoline-type inhibitor.

8.2   Experimental Methodology

The experimental procedures are the same as for the imidazoline-type inhibitor. Full details can be found in 5.2.2. The test matrix is presented in Table 22.

Table 22. High temperature test matrix with the quat-type inhibitor

Description	Parameters	
Temperature/°C	120	150
Electrolyte	1wt.% NaCl solution	
Inhibitor	alkylbenzyldimethylammonium chloride	
Inhibitor concentration/ppm	0/800 (1600 at 150°C only)	
Material	API 5L X65	
pH	pH=4.3 at 80°C after purging with CO_2	
Impeller speed/rpm	200	
Techniques applied	LPR, OCP	

8.3   Results and Discussion

8.3.1 *Corrosion Behavior of Mild Steel with the Presence of Quat-Type Inhibitor at 120°C*

Figure 66 shows the corrosion rates with and without the quat-type inhibitor for comparison. The baseline corrosion rate, in the absence of inhibitor, was relatively stable, starting at $7mm·y^{-1}$ but rapidly stabilizing at $9mm·y^{-1}$. In the presence of 800ppm of quat-type inhibitor, the corrosion rate in the initial 3 hours after injection was almost the same as the baseline. This observation alone is a strong indication that the inhibitor had little to no effect on the corrosion process. As stated earlier, the inhibition of mild steel by inhibitor occurs by the adsorption of corrosion inhibitor at the metal surface and this process starts immediately after injection. If the quat-type inhibitor had any effect on the corrosion rate, it should have been visible in the first 3 hours of exposure. However, the corrosion rate only started to decrease monotonously after 3hours until the end of each

tests. The decrease in the corrosion rate was not likely because of the inhibitor. Rather, it

is possibly a result of the formation of corrosion products.
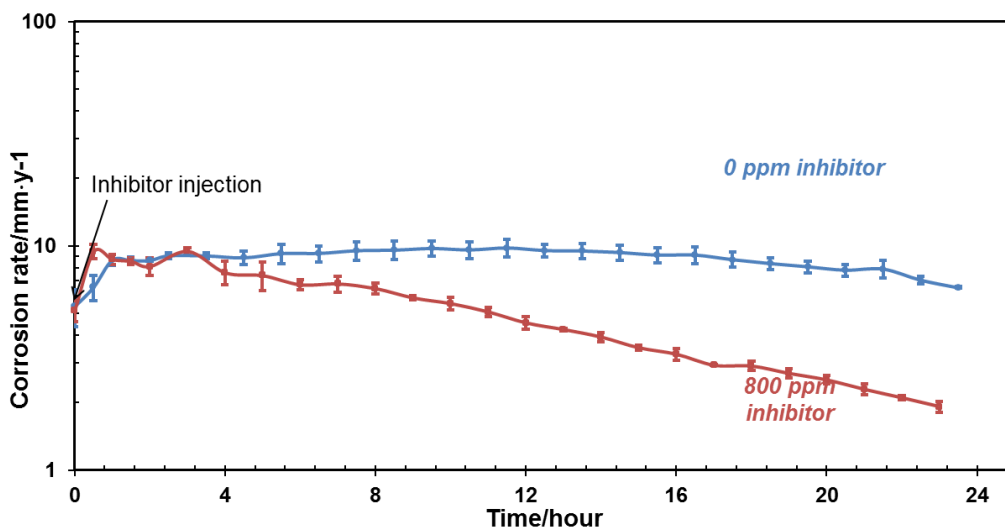
Figure 66. Corrosion rate with and without the quat-type inhibitor at 120°C. (1wt. %
NaCl, 2 bar CO_2, Initial pH at 80°C=4.3; B=23 mV/decade, 2-autoclave design)

The XRD patterns of the specimens exposed to 800ppm quat-type inhibitor are

shown in Figure 67, identifying the corrosion product as iron carbonate. The surface

morphology and cross-section images of the specimens retrieved from experiments are

shown in Figure 68 and Figure 69. They show strong evidences of the development

corrosion product. First, the crystalline structure on the surface of the specimens matches

the typical morphology of $FeCO_3$. The cross-section images shown in Figure 69 reveal a

40μm thick layer of corrosion product on top of the steel surface. In summary, a thick

layer of $FeCO_3$ was formed during the test in the presence of 800ppm quat-type inhibitor

at 120°C, and this layer was responsible for the decrease of the corrosion rate after 3
hours of the test (Figure 66).

However, without inhibitor, it was found that there was no formation of corrosion
product layer formed at 120°C in the same conditions but without inhibitor (see Figure 33
(a)). This discrepancy suggests that the addition of quat-type inhibitor might facilitate the
formation of iron carbonate. Through reviewing the literature, it was found that
quaternary ammonium compounds are used as catalysts for the crystallization of silica
molecular sieves zeolites, such as silicalite and offretite [155,156]. Similarly, it can be
speculated that the quaternary ammonium inhibitor might also promote the formation of
iron carbonate.
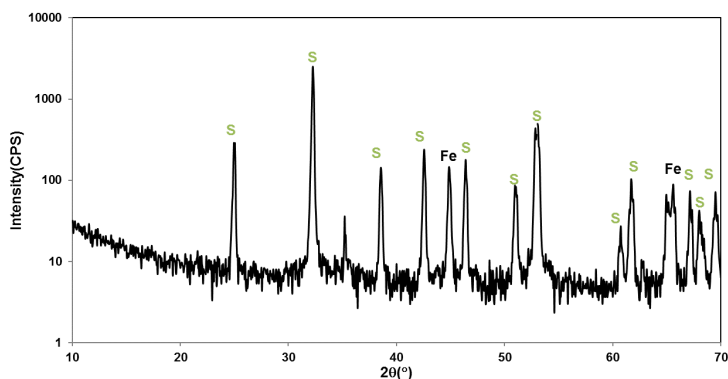
Figure 67. XRD patterns of the specimens exposed to 120°C experiments in the presence
of 800ppm quat-type inhibitor. (Fe stands for iron, S stands for siderite (iron carbonate))
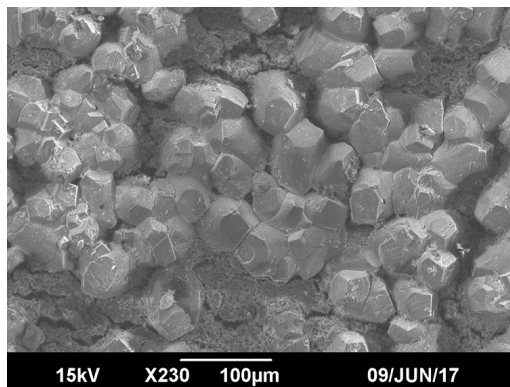
Figure 68. Surface morphology of X65 specimens surface at the end of the experiments in the presence of 800ppm quat-type inhibitor.
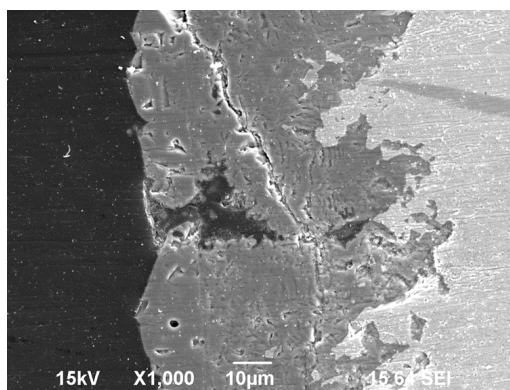
Figure 69. Cross section images of X65 specimens after experiments in the presence of quat-type inhibitor.

8.3.2 Corrosion Behavior of Mild Steel in the Presence of Quat-Type Inhibitor at

150℃

The corrosion rate measured in the presence of quat-type inhibitor at 150°C is

shown in Figure 70. With 800 ppm quat-type inhibitor, the corrosion rate was almost the

same as with 0 ppm corrosion inhibitor. As stated earlier in Chapter 5, the corrosion rate

trend at 150°C, in the absence of inhibitor, was controlled by the formation of Fe_3O_4 and

consequently followed parabolic kinetics. It can be predicted that the formation of Fe_3O_4 also controlled the corrosion rate with 800ppm quat-type inhibitor.

In the presence of 1600ppm quat-type inhibitor, although the corrosion rate trend was similar to the baseline test, the corrosion rate showed a sharper decrease. However, the difference is also not thought to be due to the adsorption of inhibitor. First, there was no significant decrease immediately after the injection of corrosion inhibitor, as it could be expected for adsorption-driven processes. Instead, it took about four hours for the corrosion trends to visibly separate. In comparison, in similar conditions, the presence of a sufficient concentration of the imidazoline-type inhibitor did lead to a rapid, yet slight, decrease in corrosion rate, as shown in Figure 43, as evidence of its adsorption properties. Going back to the quat-type inhibitor, the monotonous decrease of corrosion rate, after the first four hours of testing, is likely a result of corrosion product (Fe_3O_4 and $FeCO_3$) formation. The presence of a thick corrosion product layer (Figure 73) and high intensity peaks of Fe_3O_4 and $FeCO_3$ in Figure 71 all indicates that the formation of corrosion products is responsible for the decreasing trend in corrosion rate.
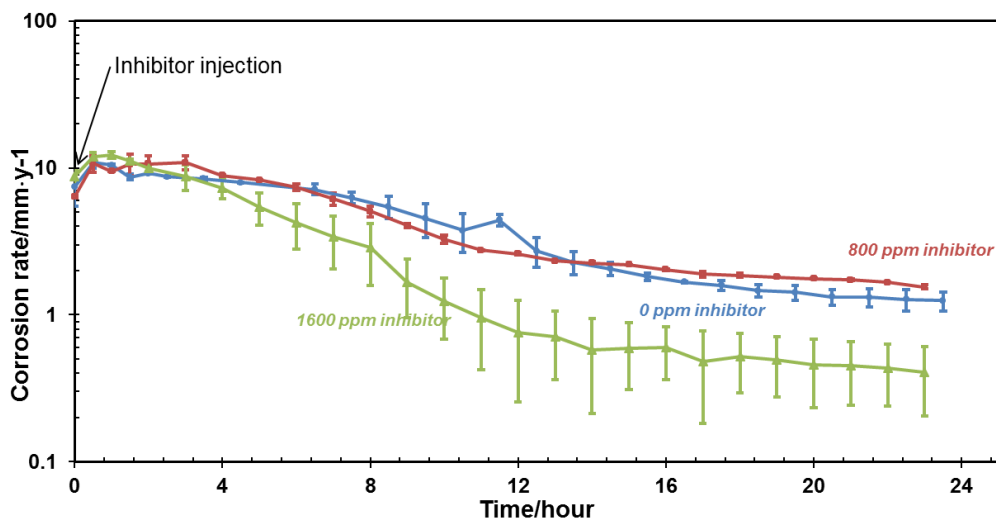
Figure 70. Corrosion rate of X65 steel at 150°C with the presence of quat type inhibitor
(1 wt.% NaCl, 2 bar CO_2, Initial pH at 80°C=4.3; B=23 mV/decade)

The presence of iron carbonate and Fe_3O_4 was confirmed by the XRD patterns as

shown in Figure 71. In addition, Figure 72 and Figure 73 show the surface morphology

and cross-section images of the specimens. In Figure 72, crystallized structures are

observed on the surfaces of the specimens which match the morphology of iron

carbonate. Without corrosion inhibitor, the cross-section images of the specimens show a

continuous layer with a thickness of 40 μm. The corrosion product layers in the cases

with 800ppm and 1600ppm corrosion inhibitor displayed thicknesses ranging from a few

micrometers to 40μm. The XRD patterns (Figure 71) suggest that Fe_3O_4 was also formed.

Therefore, it is likely that the formation of Fe_3O_4 led to the decrease of the corrosion rate

at 150°C. Here, it is important to point out the procedure did not involve any pre-

corrosion step. However, the corrosion product was always a mixture of iron carbonate

and magnetite, with or without quat-type inhibitor. In comparison, only Fe_3O_4 was

observed in Figure 44 with the presence of imidazoline-type inhibitor. Therefore, it can

be suggested that the 'quat-type' inhibitor did not show an ability to impede the

formation of corrosion products, either Fe_3O_4 or $FeCO_3$.
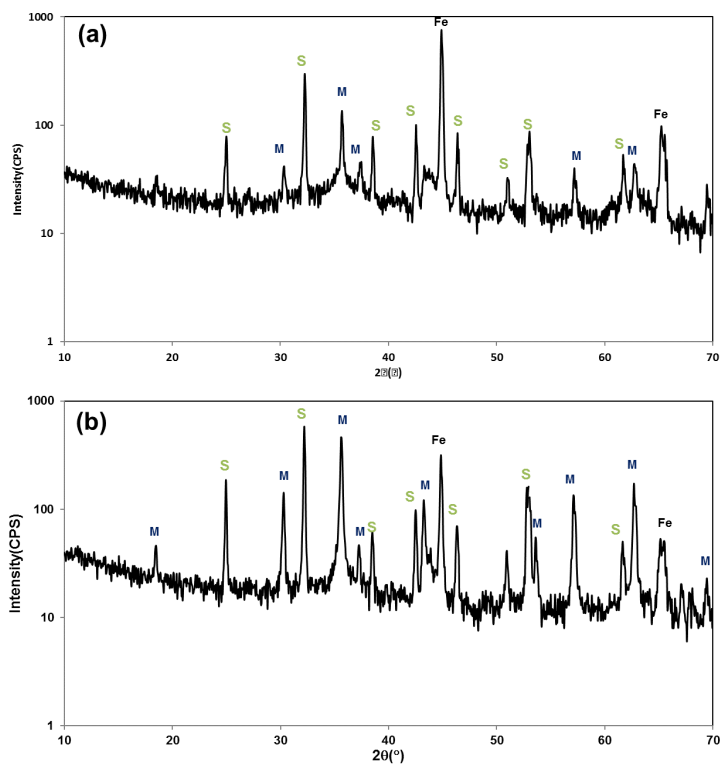
Figure 71. XRD patterns of the specimens from 150°C experiments: (a) with 800ppm
quat-type inhibitor; (b) with 1600ppm quat-type inhibitor
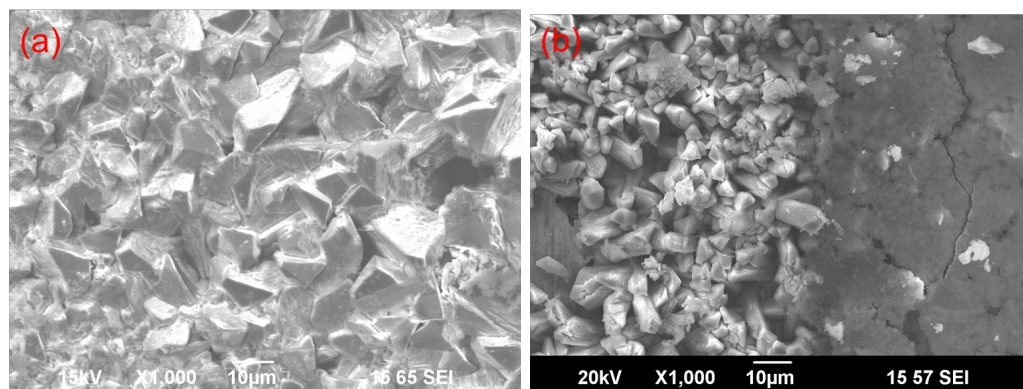
Figure 72. Surface morphology of the specimens from 150°C experiments with different amounts of quat-type inhibitor (a) with 800ppm quat-type inhibitor; (b) with 1600ppm quat-type inhibitor
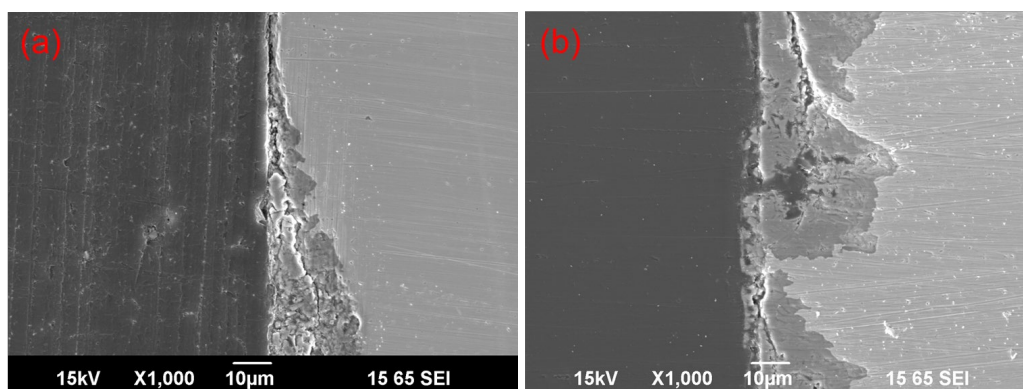
Figure 73. Cross-section images of the specimens from 150°C with the presence of different amounts of quat-type inhibitor in the 2-autoclave system: (a) with 800ppm quat-type inhibitor; (b) with 1600ppm quat-type inhibitor

8.3.3 A Comparison of the Corrosion Inhibition Performance of the Imidazoline-Type and the Quat-Type Inhibitor

In this part, the corrosion inhibition performance of the two types of inhibitors was compared at 120°C and 150°C and shown in Figure 74 and Figure 75. At 120°C (Figure 74), the imidazoline-type inhibitor could still provide corrosion protection, albeit

very poor. However, there was no sign of corrosion inhibition with the presence of the

quat-type inhibitor at the same temperature. Additionally, the gradual decrease in the

corrosion rate after three hours of exposure in the case of the quat-type inhibitor at 120°C

was the result of the formation of iron carbonate.
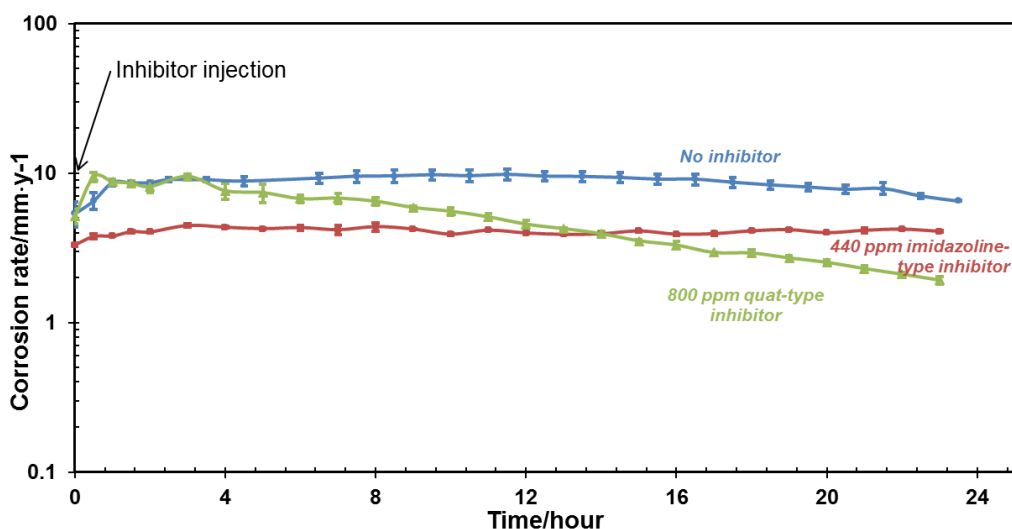
Figure 74. Corrosion rate at 120°C with the imidazoline-type and the quat-type inhibitor. (1wt. % NaCl, 2bar CO_2, Initial pH at 80°C=4.3; B=23 mV/decade; 2-autoclave system)

At 150°C (Figure 75), the performance of the two corrosion inhibitors was also

quite different. The corrosion rate with or without quat-type inhibitor was almost the

same and any decrease in the corrosion rate was the result of the formation of Fe_3O_4.

However, the corrosion rate obtained through the same procedure with the presence of

imidazoline-type inhibitor started at a lower value and was constant throughout the entire

test. This suggests that the imidazoline-type inhibitor could still provide some limited

protection against corrosion at 150°C. Therefore, the two types of corrosion inhibitors

behave quite differently even though both inhibitors are expected to be physisorbed on the metal surface.
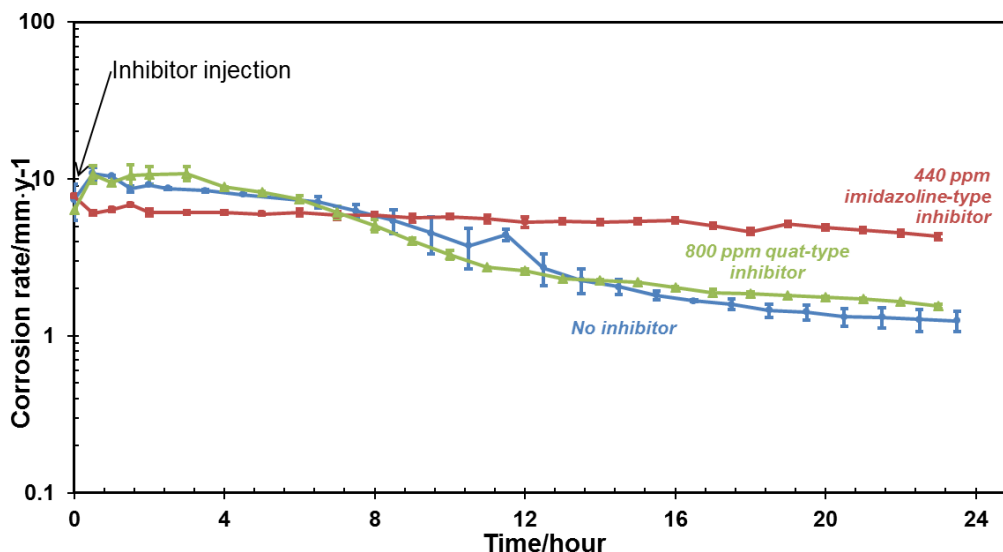
Figure 75. Corrosion rate at 150°C with imidazoline-type and quat-type inhibitor. (1wt. % NaCl, 2 bar CO_2, Initial pH at 80C=4.3; B=23 mV/decade; 2-autoclave system)

In addition, the scaling inhibition properties of the two inhibitors are significantly different. The imidazoline-type inhibitor exhibited substantial ability in inhibiting the formation of corrosion product. However, the quat-type inhibitor did not show any significant sign of scaling inhibition; on the contrary, the formation of corrosion products seemed to be facilitated and to consequently play a much more important role.

8.4   Summary

The quat-type inhibitor showed no inhibition abilities either at 120°C or at 150°C. The corrosion rate was again governed by the development of corrosion product ($FeCO_3$ at 120°C, $FeCO_3$ and Fe_3O_4 at 150°C). Unlike the imidazoline-type inhibitor, the quat-type inhibitor seemed to facilitate the formation of corrosion product.

CHAPTER 9: THE ROLE OF THERMAL STABILITY OF THE QUAT-TYPE
INHIBITOR AT ELEVATED TEMPERATURES

9.1   Introduction and Objectives

As mentioned in the hypotheses, the lack of mitigation properties of an inhibitor

at elevated temperature could also be due to its thermal stability. In the study of

imidazoline-type inhibitor, it was found that the inhibitor could partially be hydrolyzed

into its precursor, although the degradation of imidazoline-type inhibitor did not

significantly affect its performance at elevated temperatures. It is still possible that the

degradation of the quat-type inhibitor occurred at high temperature and caused its lack of

effectiveness. To confirm this hypothesis, the UV-vis spectroscopy method was used to

determine the concentration of the quat-type inhibitor before and after the tests and to

determine the extent of thermal degradation.

9.2   Experimental Procedures

The procedure for measuring the quat-type inhibitor is the same as for the

imidazoline-type inhibitor. They are described in details in Section 6.2.

9.3   Results and Discussion

The spectra obtained at different concentrations of quat-type inhibitors are given

in Figure 76. In the spectra, two functional groups are identified. As indicated earlier, the

peak at 203nm corresponds to the $n{\rightarrow}\sigma*$ transition in the quaternary ammonium group.

Moreover, three additional weaker peaks can be noticed at 254, 262, 270 nm. These

peaks are an indicator of a benzene ring as a structural moiety [146], as in the structure of

the quat-type inhibitor (see Figure 54). Certainly, the UV-vis spectra reflected the

structural information of the quat-type inhibitor.
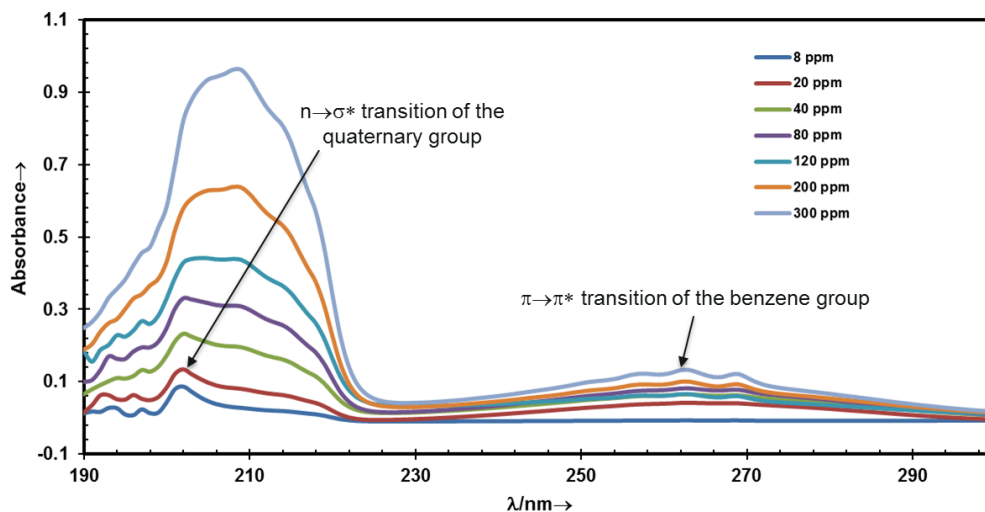
Figure 76. UV-vis spectra of the quat-type inhibitor package in 1 wt.% NaCl water with various concentration

The calibration of the concentration was also performed with known concentrations by using the absorbance at 203 nm representing the quaternary ammonium group. This group is also what defines the quat-type inhibitor. Moreover, the absorbance at 203nm is also strong and well-defined, as opposed to the peaks at 254, 262, and 269 nm. The change of absorbance with the inhibitor concentration in 1 wt.% NaCl solution was shown in Figure 77. From the figure, it can be seen that the linear relationship between the absorbance and the inhibitor concentration is also valid ($R^2 > 0.99$). A linear relationship between the quat-type inhibitor concentrations is presented in Equation (53).

$$c = 322.6 \times A_{203nm} - 13.3 \qquad (53)$$

where, c is inhibitor concentration in ppm, A_{203nm} is the absorbance at 203nm (unitless).
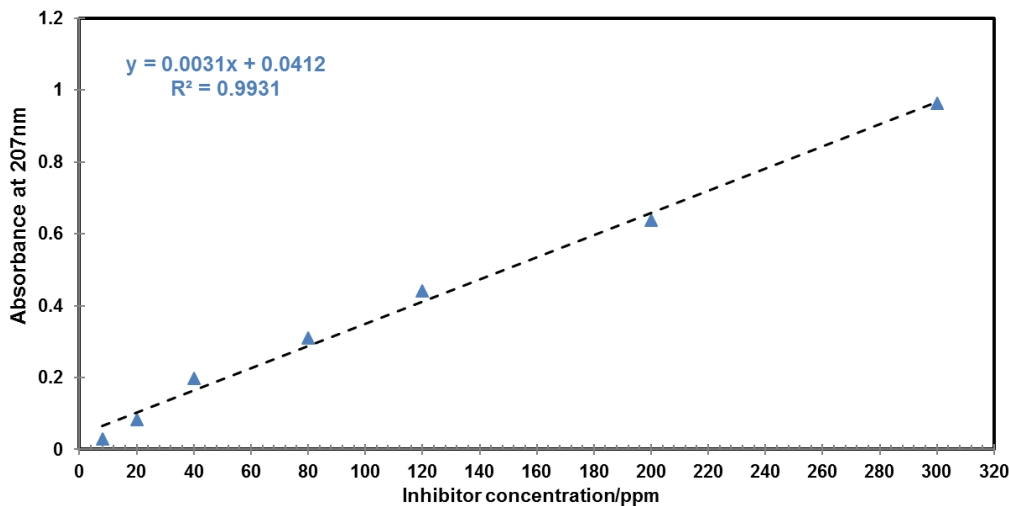
Figure 77. Absorbance at 203nm *vs.* concentration of quat-type inhibitor concentration in 1 wt.% NaCl solution

Moreover, due to the limitation of the UV-vis measurement, the calibration range is only valid up to 300 ppm. To be able to treat higher concentrations of inhibitors, the solution was diluted until the absorbance would fall below 1.

The quat-type inhibitor concentration measured using UV-vis spectroscopy from the experiments performed at 120°C and 150°C are shown in Table 23. Compared to the imidazoline-type inhibitor, which lost about 40-50 percent of its concentration during the tests, the concentration of quat-type inhibitor only decreased by 10% or less during the tests. The low percentage loss suggests that there was no significant degradation. The reason for the stability of quat-type corrosion inhibitor at elevated temperatures could be related to the synthesis reaction of this inhibitor, which does not involve water. The general synthesis reaction for an alkylbenzyldimethyl ammonium chloride can be found in Figure 78. It is hypothesized that the presence of water in some reaction steps could

affect the stability of the molecules at higher temperature, as it is the case for the imidazoline-type inhibitor. In addition, other researchers found that the quat-type inhibitor is usually stable up to 215°C [157–159]. Consequently, it is not anticipated that thermal degradation of the quat-type inhibitor affected the results. The ineffectiveness of the quat-type is most likely the result of the shift of adsorption/desorption equilibrium favoring desorption at elevated temperatures.
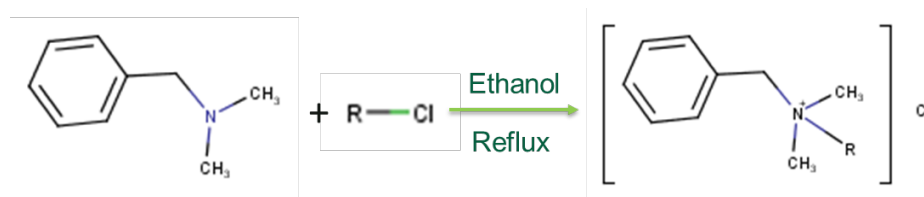
Figure 78. Synthesis reaction for the alkylbenzyldimethylammonium chloride inhibitor

Table 23. Quat-type inhibitor concentration determined by UV-vis spectroscopy at 150°C

Test conditions	Initial concentration(C_0) /ppm	Final concentration(C_1) /ppm	Residual inhibitor percentage (δ)/%
120°C, 800ppm quat-type inhibitor	780	765	98
150°C, 800ppm quat-type inhibitor	808	704	87
150°C, 1600 quat-type inhibitor	1668	1647	99

9.4   Summary

A methodology for measuring the quat-type inhibitor is established using UV-visspectroscopy. This method can be used for determining the loss of inhibitor concentration before and after each test at elevated temperatures.

The low performance of the quat-type inhibitor is not likely due to the instability of the inhibitor at elevated temperatures. The UV-vis spectroscopy results clearly show that the inhibitor did not degrade to any significant extent.

CHAPTER 10: CONCLUSION AND RECOMMENDATION FOR FUTURE WORK

10.1 Conclusions

This research work focused on the investigation of the inhibition mechanisms of mild steel at elevated temperatures in the presence of two commonly used inhibitors: an imidazoline-type and a quaternary ammonium type (quat-type) inhibitor.

Several experimental methods were used to determine the inhibition mechanisms.

- The adsorption kinetics were investigated using a QCM in a standard 2L glass cell for low to medium temperature (25°C, 50°C and 80°C).

- The corrosion inhibition efficiency for low to medium temperature (25°C, 50°C and 80°C) was also determined in standard 2L glass cell equipped with RCE setup.

- The corrosion inhibition efficiency were also determined using a novel high temperature corrosion inhibition 4L autoclave specially designed to enable the injection of inhibitor under pressure, at elevated temperatures of 120°C and 150°C.

- The inhibitor degradation was investigated by determining the inhibitor concentration and composition using UV-vis and FTIR.

The three hypotheses proposed in this research work are discussed below to determine if they are confirmed or refuted.

- **1st hypothesis**: As temperature increases, the desorption of the inhibitor is favored and the inhibitor efficiency is lost as long as the dominant adsorption mechanism is physisorption. In the case of chemisorption, the opposite behavior is expected.

This first hypothesis that focused on the role of temperature on adsorption phenomena was confirmed for the imidazoline-type inhibitor up to 120°C. The QCM measurements suggested that the adsorption of the imidazoline-type inhibitor follows Langmuir adsorption model from 25°C to 80°C and that the desorption of the inhibitor was favored with an increase in temperature. The inhibition efficiency decreased with increasing temperature up to 120°C and was completely masked by the rapid formation of Fe_3O_4 at 150°C.

For the quat-type inhibitor, this first hypothesis was also validated for temperature up to 80°C, with QCM measurements showing that desorption was favored with temperature increases. The inhibition results also showed that higher amount of inhibitor was required to achieve sufficient inhibition performance at higher temperatures. However, no inhibition could be achieved a temperature above 120°C.

- **2nd hypothesis**: Inhibitor structure alterations due to thermal degradation are directly linked to the loss or gain of efficiency.

The second hypothesis that highlighted the role of thermal stability was disproved for both inhibitors. The hydrolysis (*i.e.*, degradation) of the imidazoline-type inhibitor was confirmed using different spectroscopic analyses at 120°C and 150°C but was not significant enough to affect inhibition performance. Consequently, the failure of inhibition at 150°C could not be directly linked to the degradation of the imidazoline-type inhibitor. For the quat-type inhibitor, no significant loss was observed during the tests at higher temperature. Therefore, its thermal stability should not affect the inhibition performance significantly.

- **3rd hypothesis:** At 150°C, the formation of Fe_3O_4 is kinetically favored, the protectiveness of Fe_3O_4 is dominant and takes control of the corrosion rate.

The third hypothesis, focusing on the role of corrosion product at 150°C, was validated for both inhibitors. For the imidazoline-type inhibitor, at 150°C, the formation of Fe_3O_4 in the pre-corrosion period controlled the corrosion phenomena and masked the effect of inhibition. For this reason, the presence of inhibitor had little effect on the corrosion rate at 150°C. For the quat-type inhibitor, the corrosion rate at 150°C was also found to be mostly determined by the formation of corrosion products ($FeCO_3$ and Fe_3O_4).

The results of this research highlighted the importance of considering the formation of corrosion products when developing inhibition strategy at elevated temperatures. The work also enabled the development of appropriate experimental setup and procedure to evaluate accurately inhibitor performances at high temperatures. This brought in a significant improvement in the understanding of corrosion inhibition at elevated temperatures, unveiling some aspects of inhibition performances that had been overlooked, and allowing better corrosion management strategies for high temperature applications.

10.2 Recommendations for Future Work

Continuation of this work could include the following aspects:

- Further study of the properties of the adsorbed inhibitor films using QCM-D. In the current research, the use of a traditional QCM has shown its limitations in determining the accurate adsorption mass, the physical properties of the inhibitor film. With a QCM-D, more advanced information can be evaluated.

- <u>Effect of the uninhibited corrosion rate on the performance of corrosion inhibitor.</u>

  It has been shown that the uninhibited corrosion rates played an essential role in

  the performance of the imidazoline-type and quat-type inhibitors. However, there

  was a lack of systematic research to validate the role of uninhibited corrosion rate.

  Therefore, carefully controlled experiments are needed to propose a more

  accurate inhibition model to include the effect of baseline corrosion rate.

- <u>The development of a high temperature high pressure QCM.</u>

  The QCM measurements of the current research were only performed at

  temperatures up to 80°C. The investigation of the adsorption behavior at higher

  temperature could help validate some of the observations obtained for the

  corrosion inhibition experiments. Efforts would be needed to develop a QCM

  system able to sustain high pressure environments.

REFERENCES

[1] C. De Waard and D.E. Milliams, "Carbonic Acid Corrosion of Steel," *Corrosion* 31, 5 (1975): p. 177-181.

[2] L.G.S. Gray, B.G. Anderson, M.J. Danysh, P.G. Tremaine, "Mechanism of Carbon Steel Corrosion in Brines Containing Dissolved Carbon Dioxide at pH 4," CORROSION 1989, paper no. 464 (New Orleans, LA: NACE 1989).

[3] L.G. Gray, B.G. Anderson, M.J. Danysh, P.R. Tremaine, "Effect of pH and Temperature on the Mechanism of Carbon Steel Corrosion by Aqueous Carbon Dioxide", CORROSION 1990, paper no. 40 (Las Vegas, NV: NACE 1990).

[4] G. Schmitt and B. Rothmann, "Studies on the Corrosion Mechanism of Unalloyed Steel in Oxygen-Free Carbon Dioxide Solutions. Part I. Kinetics of the Liberation of Hydrogen," *Werkstoffe und Korrosion* 28 (1977): p. 816-822.

[5] S. Nesic, B.F.M. Pots, J. Postlethwaite, N. Thevenot, "Superposition of Diffusion and Chemical Reaction Controlled Limiting Currents–Application to CO_2 Corrosion, "*Journal of Corrosion Science and Engineering* 1, 3 (1995).

[6] S. Nesic, J. Postlethwaite, S. Olsen, "An Electrochemical Model for Prediction of Corrosion of Mild Steel in Aqueous Carbon Dioxide Solutions," *Corrosion* 52, 4 (1996): p. 280-294.

[7] M. Nordsveen, S. Nesic, R. Nyborg, A. Stangeland, "A Mechanistic Model for Carbon Dioxide Corrosion of Mild Steel in the Presence of Protective Iron Carbonate Films-Part 1: Theory and Verification," *Corrosion*. 59, 5 (2003): p. 443-456.

[8] S. Nesic, M. Nordsveen, R. Nyborg, A. Stangeland, "A Mechanistic Model for Carbon Dioxide Corrosion of Mild Steel in the Presence of Protective Iron Carbonate Films-Part 2: A Numerical Experiment," *Corrosion* 59, 6 (2003): p. 489-497.

[9] S. Nesic, and K.L. Lee, "A Mechanistic Model for Carbon Dioxide Corrosion of Mild Steel in the presence of Protective Iron Carbonate Films-Part 3: Film Growth Model," *Corrosion* 59, 7 (2003): p. 616-628.

[10] S. Nesic, "Key Issues Related to Modelling of Internal Corrosion of Oil and Gas Pipelines-A Review," *Corrosion Science* 49, 12 (2007): p. 4308-4338.

[11] E. Remita, B. Tribollet, E. Sutter, V. Vivier, F. Ropital, J. Kittel, "Hydrogen Evolution in Aqueous Solutions Containing Dissolved CO_2: Quantitative Contribution of the Buffering Effect," *Corrosion Science* 50, 5 (2008): p. 1433-1440.

[12] A. Kahyarian, B. Brown, S. Nesic, "Electrochemistry of CO_2 Corrosion of Mild Steel: Effect of CO_2 on Iron Dissolution Reaction," *Corrosion Science* 129, (2017): p. 146-151.

[13] A. Kahyarian, B. Brown, S. Nesic, "Technical Note: Electrochemistry of CO_2 Corrosion of Mild Steel: Effect of CO_2 on Cathodic Currents," *Corrosion*. 74, 8 (2018): p. 851-859.

[14] C. De Waard and D.E. Williams, "Prediction of Carbonic Acid Corrosion in Natural Gas Pipelines," *Ind. Finish. Surf. Coatings* 28, 340 (1976): p. 24-26.

[15] A. Shadravan and M. Amani, "HPHT 101-What Petroleum Engineers and Geoscientists Should Know about High Pressure High Temperature Wells Environment," *Energy Science and Technology* 4, 2 (2012): p. 36-60.

[16] R.W. Bentley, "Global Oil & Gas Depletion: an Overview," *Energy Policy* 30, 3 (2002): p. 189-205.

[17] P. Elliott, "Overcome the Challenge of High Temperature Corrosion," CORROSION 2011, paper no. 11147 (Houston, TX: NACE 2011).

[18] Tetrahedron, Inc., "Study of High Pressure High Temperature Mapping of the Gulf of Mexico," Report prepared for the Bureau of Safety and Environmental enforcement, July 2017.

[19] Z.F. Yin, Y.R. Feng, W.Z. Zhao, Z.Q. Bai, G.F. Lin, "Effect of Temperature on CO_2 Corrosion of Carbon Steel," *Surface and Interface Analysis* 41,6 (2009): p. 517-523.

[20] S.D. Zhu, A.Q. Fu, J. Miao, Z.F. Yin, G.S. Zhou, J.F. Wei, "Corrosion of N80 Carbon Steel in Oil Field Formation Water Containing CO_2 in the Absence and Presence of Acetic Acid," *Corrosion Science* 53, 10 (2011): p. 3156-3165.

[21] T. Tanupabrungsun, D. Young, B. Brown, S. Nesic, "Construction and Verification of Pourbaix Diagrams for CO_2 Corrosion of Mild Steel Valid up to 250°C," CORROSION 2012, paper no. 1418 (Salt Lake City, UT: NACE 2012).

[22] T. Tanupabrungsun, B. Brown, S. Nesic, "Effect of pH on CO_2 Corrosion of Mild Steel at Elevated Temperatures," CORROSION 2013, paper no. 2348 (Orlando, FL: NACE 2013).

[23] T. Bellezze, G. Roventi, R. Fratesi, "Electrochemical Characterization of Three Corrosion-Resistant Alloys after Processing for Heating-Element Sheathing," *Electrochimica Acta* 49, 17-18 (2004): p. 3005-3014.

[24] K. Hashimoto, "2002 W.R. Whitney Award Lecture: In Pursuit of New Corrosion-Resistant Alloys," *Corrosion* 58, 9 (2002): p. 715-722.

[25] G.K. Gomma and M.H. Wahdan, "Effect of Temperature on the Acidic Dissolution of Copper in the Presence of Amino Acids," *Materials Chemistry and Physics* 39, 2 (1994): p. 142-148.

[26] B.A. Alink, B. Outlaw, V. Jovancicevic, S. Ramachandran, S. Campbell, "Mechanism of CO_2 Corrosion Inhibition by Phosphate Esters," CORROSION 99, paper no. 99037 (San Antonio, TX: NACE 1999).

[27] W. Villamizar, M. Casales, J.G. Gonzalez-Rodriguez, L. Martinez, "CO_2 Corrosion Inhibition by Hydroxyethyl, Aminoethyl, and Amidoethyl Imidazolines in Water-Oil Mixtures," *Journal of Solid State Electrochemistry* 11, 5 (2007): p. 619-629.

[28] Q.Y. Liu, L.J. Mao, S.W. Zhou, "Effects of Chloride Content on CO_2 Corrosion of Carbon Steel in Simulated Oil and Gas Well Environments," *Corrosion Science* 84, (2014): p. 165-171.

[29] G. Zhang, C. Chen, M. Lu, C. Chai, Y. Wu, "Evaluation of Inhibition Efficiency of an Imidazoline Derivative in CO_2-Containing Aqueous Solution," *Materials Chemistry and Physics* 105, 2-3 (2007): p. 331-340.

[30] A. Popova, "Temperature Effect on Mild Steel Corrosion in Acid Media in Presence of Azoles," *Corrosion Science* 49, 5 (2007): p. 2144-2158.

[31] L. Wei, Z. Chen, X. Guo, "Inhibition Behavior of an Imidazoline Inhibitor for Carbon Steel in a Supercritical CO_2/H_2O System," *Journal of the Electrochemical Society* 164, 9 (2017): p. C602-C609.

[32] X. Zhang, F. Wang, Y. He, Y. Du, "Study of the Inhibition Mechanism of imidazoline Amide on CO_2 Corrosion of Armco Iron," *Corrosion Science* 43, 8 (2001): p. 1417-1431.

[33] P. Ren, D. Zhang, C. Dong, X. Li, "Preparation and Evaluation of Intelligent Corrosion Inhibitor Based on Photo-crosslinked pH-Sensitive Hydrogels," *Materials Letters* 160, (2015): p. 480-483.

[34] G. Schmitt, "Application of Inhibitors for Acid Media: Report Prepared for the European Federation of Corrosion Working Party on Inhibitors," *British Corrosion Journal* 19, 4 (1984): p. 165-176.

[35] H.J. Chen, W.P. Jepson, T. Hong, "High Temperature Corrosion Inhibition Performance of Imidazoline and Amide," CORROSION 2000, paper no. 00035 (Orlando, FL: NACE 2000).

[36] N.U. Obeyesekere, A.R. Naraghi, L. Chen, S. Zhou, S. Wang, "Novel Corrosion Inhibitors for High Temperature Applications," CORROSION 2005, paper no. 05636 (Houston, TX: NACE 2005).

[37] S. Ramachandran, Y.S. Ahn, M. Greaves, V. Jovancicevic, J. Bassett, "Development of High Temperature High Pressure Corrosion Inhibitor," CORROSION 2006, paper no. 06377 (San Diego, CA: NACE 2006).

[38] S. Ramachandran, V. Jovancicevic, J. Long, "Development of a New Water Soluble High Temperature Corrosion Inhibitor," CORROSION 2009, paper no. 09237 (Atlanta. GA: NACE 2009).

[39] A. Palencsár, E. Gulbrandsen, K. Kosorú, "High Temperature Testing of Corrosion Inhibitor Performance," CORROSION 2013, paper no. 2610 (Orlando, FL: NACE 2013).

[40] S. Ramachandran, V. Jovancicevic, G. Boyce, C. Zeadow, C. McAfee, "New Water Soluble High Shear High Temperature Corrosion Inhibitor," CORROSION 2013, paper no. 2277 (Orlando, FL: NACE 2013).

[41] J.E. Oddo and M.B. Tomson, "Simplified Calculation of $CaCO_3$ Saturation at High Temperatures and Pressures in Brine Solutions," *Journal of Petroleum Technology* 34, 07 (1982): p. 1-583.

[42] D.A. Palmer and R. Van Eldik, "The Chemistry of Metal Carbonato and Carbon Dioxide Complexes," *Chemical Reviews* 83, 6 (1983): p. 651-731.

[43] Y.K. Kharaka, W.D. Gunter, P.K. Aggarwal, E.H. Perkins, J.D. DeBraal, "SOLMINEQ. 88: A Computer Program for Geochemical Modeling of Water-rock Interactions," *US Geological Survey Water-Resources Investigation Report* 88 (1988): p. 420.

[44] B.R. Linter and G.T. Burstein, "Reactions of Pipeline Steels in Carbon Dioxide Solutions," *Corrosion Science* 41, 1 (1999): p. 117-139.

[45] T. Tran, B. Brown, and S. Nesic. "Corrosion of Mild Steel in an Aqueous CO_2 Environment—Basic Electrochemical Mechanisms Revisited," CORROSION 2015, paper no. 5671 (Dallas, TX: NACE 2015).

[46] M. Gao, X. Pang, K. Gao, "The Growth Mechanism of CO_2 Corrosion Product Films," *Corrosion Science* 53, 2 (2011): p. 557-568.

[47] E. Hunnick, B.F.M. Pots, E. Hendriksen, "The Formation of Protective $FeCO_3$ Corrosion Product Layers in CO_2 Corrosion," CORROSION 96, paper no. 96006 (Denver, CO: NACE 1996).

[48] E.C. Potter and G.M.W. Mann, "The Fast Linear Growth of Magnetite on Mild Steel in High-Temperature Aqueous Conditions," *British Corrosion Journal*. 1, 1 (1965): p. 26-35.

[49] G.A. Schmitt and M. Mueller, "Critical Wall Shear Stresses in CO_2 Corrosion of Carbon Steel," CORROSION 99, paper no. 99044 (San Antonio, TX: NACE 1999).

[50] V. Ruzic, M. Veidt, S. Nesic, "Protective Iron Carbonate Films—Part 1: Mechanical Removal in Single-Phase Aqueous Flow," *Corrosion* 62, 5 (2006): p. 419-432.

[51] B.F.M. Pots, E.L.J.A. Hendriksen, H. Pit, "Field Study of Corrosion Inhibition at Very High Flow Velocity," CORROSION 2003, paper no. 03321 (San Diego, CA: NACE 2003).

[52] W. Li, B.F.M. Pots, B. Brown, K.E. Kee, S. Nesic, "A Direct Measurement of Wall Shear Stress in Multiphase Flow—Is It an Important Parameter in CO_2 Corrosion of Carbon Steel Pipelines?," *Corrosion Science* 110 (2016): p. 35–45.

[53] R.D. Tems and A.M. Al-Zahrani, "Cost of Corrosion in Gas Sweetening and Fractionation Plants," CORROSION 2006, paper no. 06444 (San Diego, CA: NACE 2006).

[54] S.D. Cramer and B.S. Covino, *ASM Handbook Vol. 13 A Corrosion: Fundamentals, Testing, and Protection*, (Materials Park, OH: ASM International, 2003) p. 1135.

[55] H.H. Uhlig, *Uhlig's Corrosion Handbook*, 3rd ed. (John Wiley & Sons, 2011) p. 1026.

[56] P.A. Schweitzer, *Fundamentals of Corrosion : Mechanisms, Causes, and Preventative Methods*, 1st ed. (Boca Raton, CRC Press, 2009).

[57] M. Finšgar and J. Jackson, "Application of Corrosion Inhibitors for Steels in Acidic Media for the Oil and Gas Industry: A Review," *Corrosion Science* 86, (2014): p. 17-41.

[58] A.J. Son, "Developments in the Laboratory Evaluation of Corrosion Inhibitors: A Review," CORROSION 2007, paper no. 07618 (Nashville, TN: NACE 2007).

[59] J.O.M. Bockris and D.A.J. Swinkels, "Adsorption of n-Decylamine on Solid Metal Electrodes," *Journal of The Electrochemical Society* 111, 6 (1964): p. 736-743.

[60] E. Khamis, F. Bellucci, R.M. Latanision, E.S.H. El-Ashry, "Acid Corrosion Inhibition of Nickel by 2-Triphenosphoranylidene Succinic Anhydride," *Corrosion* 47, 9 (1991): p. 677-686.

[61] L.J. Oblonsky, G.R. Chesnut, T.M. Devine, "Adsorption of Octadecyldimethylbenzylammonium Chloride to Two Carbon Steel Microstructures

as Observed with Surface-Enhanced Raman Spectroscopy," *Corrosion*. 51, 12 (1995): p. 891-900.

[62] P. Kern and D. Landolt, "Adsorption of Organic Corrosion Inhibitors on Iron in the Active and Passive State. A Replacement Reaction between Inhibitor and Water Studied with the Rotating Quartz Crystal Microbalance," *Electrochimica Acta* 47, 4 (2001): p. 589-598.

[63] J.O.M. Bockris and A.K.N. Reddy, *Modern Electrochemistry. Vol. 2*, 1st ed. (Springer, 1970), p. 1013.

[64] N. Pebere, M. Duprat, F. Dabosi, A. Lattes, A.D. Savignac, "Corrosion Inhibition Study of a Carbon Steel in Acidic Media Containing Hydrogen Sulphide and Organic Surfactants," *Journal of applied electrochemistry* 18, 2 (1988): p. 225-231.

[65] J.O.M Bockris, A.K.N. Reddy, M.E Gamboa-Aldeco, *Modern Electrochemistry, 2A: Fundamentals of Electrodics*, 2nd ed. (Springer, 2000).

[66] M.A. Amin, S.S.A. El-Rehim, E.E.F El-Sherbini, R.S. Bayoumi, "The Inhibition of Low Carbon Steel Corrosion in Hydrochloric Acid Solutions by Succinic Acid: Part I. Weight loss, Polarization, EIS, PZC, EDX and SEM Studies." *Electrochimica Acta* 52, 11 (2007): p. 3588-3600.

[67] E.E. Oguzie, Y. Li, F.H. Wang, "Corrosion Inhibition and Adsorption Behavior of Methionine on Mild Steel in Sulfuric Acid and Synergistic Effect of Iodide Ion," *Journal of Colloid and Interface Science* 310, 1 (2007): p. 90-98.

[68] G. Moretti, F. Guidi, G. Grion, "Tryptamine as a Green Iron Corrosion Inhibitor in 0.5M Deaerated Sulphuric Acid," *Corrosion Science* 46, 2 (2004): p. 387-403.

[69] R.J. Tedeschi, "Acetylenic Corrosion Inhibitors," *Corrosion* 31, 4 (1975): p. 130-134.

[70] X. He, Y. Jiang, C. Li, W. Wang, B. Hou, L. Wu, "Inhibition Properties and Adsorption Behavior of Imidazole and 2-phenyl-2-imidazoline on AA5052 in 1.0M HCl Solution," *Corrosion Science* 83, (2014): p. 124-136.

[71] I. Jevremovic, M. Singer, S. Nesic, V. Miskovic-Stankovic, "Inhibition Properties of Self-Assembled Corrosion Inhibitor Talloil Diethylenetriamine Imidazoline for Mild Steel Corrosion in Chloride Solution Saturated with Carbon Dioxide," *Corrosion Science* 77, (2013): p. 265-272.

[72] X. Li, S. Deng, H. Fu, T. Li, "Adsorption and Inhibition Effect of 6-Benzylaminopurine on Cold Rolled Steel in 1.0 M HCl," *Electrochimica Acta* 54, 16 (2009): p. 4089-4098.

[73] F.S. de Souza and A. Spinelli, "Caffeic Acid as a Green Corrosion Inhibitor for Mild Steel," *Corrosion Science* 51, 3 (2009): p. 642-649.

[74] A. Edwards, C. Osborne, S. Webster, D. Klenerman, M. Joseph, P. Ostovar, M. Doyle, "Mechanistic Studies of the Corrosion Inhibitor Oleic Imidazoline," *Corrosion Science* 36, 2 (1994): p. 315-325.

[75] C. Fiaud, A. Harch, D. Mallouh, M. Tzinmann, "The Inhibition of Iron Corrosion by Acetylenic Alcohols in Acid Solutions at High Temperature," *Corrosion Science* 35, 5-8 (1993): p. 1437-1444.

[76] N.I. Podobaev and Y.G. Avdeev, "A Review of Acetylene Compounds as Inhibitors of Acid Corrosion of Iron," *Protection of Metals* 40, 1 (2004): p. 7-13.

[77] R. Ketrane, B. Saidani, O. Gil, L. Leleyter, F. Baraud, "Efficiency of Five Scale Inhibitors on Calcium Carbonate Precipitation from Hard Water: Effect of Temperature and Concentration," *Desalination* 249, 3 (2009): p. 1397-1404.

[78] S. Baraka-Lokmane and K.S. Sorbie, "Effect of pH and Scale Inhibitor Concentration on Phosphonate–Carbonate Interaction," *Journal of Petroleum Science and Engineering* 70, 1-2 (2010): p. 10-27.

[79] M.A. Kelland, "Effect of Various Cations on the Formation of Calcium Carbonate and Barium Sulfate Scale with and without Scale Inhibitors," *Industrial & Engineering Chemistry Research* 50, 9 (2011): p. 5852-5861.

[80] İ. Dehri and M. Özcan, "The Effect of Temperature on the Corrosion of Mild Steel in Acidic Media in the Presence of Some Sulphur-Containing Organic Compounds," *Materials Chemistry and Physics* 98, 2-3 (2006): p. 316-323.

[81] R. Solmaz, G. Kardaş, M. Culha, B. Yazıcı, M. Erbil, "Investigation of Adsorption and Inhibitive Effect of 2-mercaptothiazoline on Corrosion of Mild Steel in Hydrochloric Acid Media," *Electrochimica Acta* 53, 20 (2008): p. 5941-5952.

[82] R. Karthikaiselvi and S. Subhashini, "Study of Adsorption Properties and Inhibition of Mild Steel Corrosion in Hydrochloric Acid Media by Water Soluble Composite Poly (Vinyl Alcohol-o-Methoxy Aniline)," *Journal of the Association of Arab Universities for Basic and Applied Sciences* 16, 1 (2014): p. 74-82.

[83] M.A. Amin, O.A. Hazzazi, F. Kandemirli, M. Saracoglu, "Inhibition Performance and Adsorptive Behavior of Three Amino Acids on Cold-Rolled Steel in 1.0 M

HCl—Chemical, Electrochemical, and Morphological Studies," *Corrosion* 68, 8 (2012): p. 688-698.

[84] P. Lowmunkhong, D. Ungthararak, P Sutthivaiyakit, "Tryptamine as a Corrosion Inhibitor of Mild Steel in Hydrochloric Acid Solution." *Corrosion Science* 52, 1 (2010): p.30-36.

[85] F. Bentiss, M. Lebrini, M. Lagrenée, "Thermodynamic Characterization of Metal Dissolution and Inhibitor Adsorption Processes in Mild Steel/2,5-Bis(*n*-thienyl)-1,3,4-Thiadiazoles/Hydrochloric Acid System," *Corrosion Science* 47, 12 (2005): p. 2915-2931.

[86] X. Li, S. Deng, G. Mu, H. Fu, F. Yang, "Inhibition Effect of Nonionic Surfactant on the Corrosion of Cold Rolled Steel in Hydrochloric Acid," *Corrosion Science* 50, 2 (2008): p. 420-430.

[87] G. Moretti, G. Quartarone, A. Tassan, A. Zingales, "Inhibition of Mild Steel Corrosion in 1N Sulphuric Acid through Indole," *Materials and Corrosion* 45, 12 (1994): p. 641-647.

[88] E.E. Oguzie, "Studies on the Inhibitive Effect of Occimum Viridis Extract on the Acid Corrosion of Mild Steel," *Materials Chemistry and Physics* 99, 2-3 (2006): p. 441-446.

[89] E.E. Oguzie, "Evaluation of the Inhibitive Effect of Some Plant Extracts on the Acid Corrosion of Mild Steel," *Corrosion Science* 50, 11 (2008): p. 2993-2998.

[90] R. Solmaz, G. Kardaş, B. Yazıcı, MErbil, "Adsorption and Corrosion Inhibitive Properties of 2-Amino-5-Mercapto-1, 3, 4-Thiadiazole on Mild Steel in

Hydrochloric Acid Media," *Colloids and Surfaces A: Physicochemical and Engineering Aspects* 312, 1 (2008): p.7-17.

[91] A. Popova, E. Sokolova, S. Raicheva, M. Christov, "AC and DC Study of the Temperature Effect on Mild Steel Corrosion in Acid Media in the Presence of Benzimidazole Derivatives," *Corrosion Science* 45, 1 (2003): p. 33-58.

[92] D. Hasson, S. Hilla, S. Alexander. "State of the Art of Friendly "Green" Scale Control Inhibitors: A Review Article." *Industrial & Engineering Chemistry Research* 50, 12 (2011): p. 7601-7607.

[93] L. Zheng, J. Landon, N.C. Koebcke, P. Chandan, K. Liu, "Suitability and Stability of 2-Mercaptobenzimidazole as a Corrosion Inhibitor in a Post-Combustion CO_2 Capture System," *Corrosion* 71, 6 (2015): p. 692-702.

[94] G.W. Poling, "Infrared Studies of Protective Films Formed by Acetylenic Corrosion Inhibitors," *Journal of The Electrochemical Society* 114, 12 (1967): p. 1209-1214.

[95] P.C. Okafor, X. Liu, Y.G. Zheng, "Corrosion Inhibition of Mild Steel by Ethylamino Imidazoline Derivative in CO_2-Saturated Solution," *Corrosion Science* 51, 4 (2009): p. 761-768.

[96] P.C. Okafor, C.B. Liu, Y.J. Zhu, Y.G. Zheng, "Corrosion and Corrosion Inhibition Behavior of N80 and P110 Carbon Steels in CO_2-Saturated Simulated Formation Water by Rosin Amide Imidazoline," *Industrial & Engineering Chemistry Research* 50, 12 (2011): p. 7273-7281.

[97] F.G. Liu, M. Du, J. Zhang, M. Qiu, "Electrochemical Behavior of Q235 Steel in Saltwater Saturated with Carbon Dioxide Based on New Imidazoline Derivative Inhibitor," *Corrosion Science* 51, 1 (2009): p. 102-109.

[98] K. Zhang, B. Xu, W. Yang, X. Yin, Y. Liu, Y. Chen, "Halogen-Substituted Imidazoline Derivatives as Corrosion Inhibitors for Mild Steel in Hydrochloric Acid Solution," *Corrosion Science* 90, (2015): p. 284-295.

[99] K. Zhang, W. Yang, B. Xu, Y. Liu, X. Yin, Y. Chen, "Corrosion Inhibition of Mild Steel by Bromide-Substituted Imidazoline in Hydrochloric Acid," *Journal of the Taiwan Institute of Chemical Engineers* 57, (2015): p. 167-174.

[100] X. He, Y. Jiang, C. Li, W. Wang, B. Hou, L. Wu, "Inhibition Properties and Adsorption Behavior of Imidazole and 2-Phenyl-2-Imidazoline on AA5052 in 1.0M HCl Solution," *Corrosion Science* 83, (2014): p. 124-136.

[101] M.A. Quraishi, M.Z.A. Rafiquee, S. Khan, N. Saxena, "Corrosion Inhibition of Aluminium in Acid Solutions by Some Imidazoline Derivatives," *Journal of Applied Electrochemistry* 37, 10 (2007): p. 1153-1162.

[102] J.A. Martin and F.W. Valone, "The Existence of Imidazoline Corrosion Inhibitors," *Corrosion* 41, 5 (1985): p. 281-287.

[103] D. Bajpai and V.K. Tyagi, "Fatty Imidazolines: Chemistry, Synthesis, Properties and Their Industrial Applications," *Journal of Oleo Science* 55, 7 (2006): p. 319-329.

[104]   J.L. Riebsomer, "The Synthesis of Imidazolines from 1, 2-Diamines and Carboxylic Acids," *Journal of the American Chemical Society* 70, 4 (1948): p. 1629-1632.

[105]   V. Jovancicevic, S. Ramachandran, P. Prince, "Inhibition of Carbon Dioxide Corrosion of Mild Steel by Imidazolines and Their Precursors," *Corrosion* 55, 5 (1999): p. 449-455.

[106]   J. Cruz, R. Martínez, J. Genesca, E. García-Ochoa, "Experimental and Theoretical Study of 1-(2-Ethylamino)-2-Methylimidazoline as an Inhibitor of Carbon Steel Corrosion in Acid Media," *Journal of Electroanalytical Chemistry* 566, 1 (2004): p. 111-121.

[107]   O. Olivares-Xometl, N.V. Likhanova, M.A. Domínguez-Aguilar, J.M. Hallen, L.S. Zamudio, E. Arce, "Surface Analysis of Inhibitor Films Formed by Imidazolines and Amides on Mild Steel in an Acidic Environment," *Applied Surface Science* 252, 6 (2006): p. 2139-2152.

[108]   T.Y. Soror and M.A. El-Ziady, "Effect of Cetyl Trimethyl Ammonium Bromide on the Corrosion of Carbon Steel in Acids," *Materials Chemistry and Physics* 77, 3 (2003): p. 697-703.

[109]   M.A. Deyab, "Effect of Cationic Surfactant and Inorganic Anions on the Electrochemical Behavior of Carbon Steel in Formation Water," *Corrosion Science* 49, 5 (2007): p. 2315-2328.

[110]   V.J. Drazic and D.M. Drazic, "Influence of the Metal Dissolution Rate on the Anion and Inhibitor Adsorption," in 7th European Symposium on Corrosion Inhibitor, 1990: p. 99-110.

[111]   L.M. Vračar, D.M. Dražić, "Adsorption and Corrosion Inhibitive Properties of Some Organic Molecules on Iron Electrode in Sulfuric Acid," *Corrosion Science* 44, 8 (2002): p. 1669-1680.

[112]   D. Liu, Y.B. Qiu, Y. Tomoe, K. Bando, X.P. Guo, "Interaction of Inhibitors with Corrosion Scale Formed on N80 Steel in CO_2-Saturated NaCl Solution," *Materials and Corrosion* 62, 12 (2011): p. 1153-1158.

[113]   L.D. Paolinelli, T. Pérez, S.N. Simison, "The Incidence of Chromium-Rich Corrosion Products on the Efficiency of an Imidazoline-Based Inhibitor Used for CO_2 Corrosion Prevention," *Materials Chemistry and Physics* 126, 3 (2011): p. 938-947.

[114]   H. Zhang, X. Pang, M. Zhou, C. Liu, L. Wei, K. Gao, "The Behavior of Pre-Corrosion Effect on the Performance of Imidazoline-Based Inhibitor in 3 wt.% NaCl Solution Saturated with CO_2," *Applied Surface Science* 356, (2015): p. 63-72.

[115]   S. Papavinasam, R.W. Revie, M. Attard, A. Demoz, K. Michaelian, "Comparison of Laboratory Methodologies to Evaluate Corrosion Inhibitors for Oil and Gas Pipelines," *Corrosion* 59, 10 (2003): p. 897-912.

[116]   Y. Zhu, M.L. Free, R. Woollam, W. Durnie, "A Review of Surfactants as Corrosion Inhibitors and Associated Modeling," *Progress in Materials Science* 90, (2017): p. 159-223.

[117]   S. Martinez and S. Ivica, "Thermodynamic Characterization of Metal Dissolution and Inhibitor Adsorption Processes in the Low Carbon Steel/Mimosa Tannin/Sulfuric Acid System," *Applied Surface Science* 199, 1-4 (2002): p. 83-89.

[118]   F. Mansfeld, "Electrochemical Impedance Spectroscopy (EIS) as a New Tool for Investigating Methods of Corrosion Protection," *Electrochimica Acta* 35, 10 (1990): p. 1533-1544.

[119]   T. Murakawa, S. Nagaura, N. Hackerman, "Coverage of Iron Surface by Organic Compounds and Anions in Acid Solutions," *Corrosion Science* 7, 2 (1967): p. 79-89.

[120]   T. Murakawa, T. Kato, G. Wakisaka, "Relationship between Inhibition Efficiency and the Degree of Surface Coverage of Corrosion Inhibitors," *Journal of the Metal Finishing Society of Japan* 17, 11 (1966): p. 438-442.

[121]   V. Pandarinathan, K. Lepková, S.I. Bailey, T. Becker, R. Gubner, "Adsorption of Corrosion Inhibitor 1-Dodecylpyridinium Chloride on Carbon Steel Studied by *In situ* AFM and Electrochemical Methods," *Industrial & Engineering Chemistry Research* 53, 14 (2014): p. 5858–5865.

[122]   J.D. Olivo, D. Young, B. Brown, S. Nesic, "Effect of Corrosion Inhibitor Alkyl Tail Length on the Electrochemical Process Underlying CO_2 Corrosion of Mild Steel," CORROSION 2018, paper no. 11537 (Phoenix, AZ: NACE 2018).

[123]   J. Curie, P. Curie, "Development by Pressure of Polar Electricity in Hemihedral Crystals with Inclined Faces," *Bull. Soc. Min. de France* 3, (1880): p. 90.

[124]   G. Sauerbrey, "Verwendung von Schwingquarzen zur Wägung dünner Schichten und zur Mikrowägung," *Zeitschrift für physik* 155, 2 (1959): p. 206-222.

[125]   M. Knag, J. Sjöblom, E. Gulbrandsen, "The Effect of Straight Chain Alcohols and Ethylene Glycol on the Adsorption of CTAB on Gold," *Journal of Dispersion Science and Technology* 26, 2 (2005): p. 207-215.

[126]   C. Gutig, B.P. Grady, A. Striolo, "Experimental Studies on the Adsorption of Two Surfactants on Solid−Aqueous Interfaces: Adsorption Isotherms and Kinetics," *Langmuir* 24, (2008): p. 4806-4816.

[127]   F. Höök, B. Kasemo, T. Nylander, C. Fant, K. Sott, H. Elwing, "Variations in Coupled Water, Viscoelastic Properties, and Film Thickness of a Mefp-1 Protein Film during Adsorption and Cross-Linking: A Quartz Crystal Microbalance with Dissipation Monitoring, Ellipsometry, and Surface Plasmon Resonance Study," *Analytical chemistry* 73, 24 (2001): p. 5796-5804.

[128]   L. Macakova, E. Blomberg, P.M. Claesson, "Effect of Adsorbed Layer Surface Roughness on the QCM-D Response: Focus on Trapped Water," *Langmuir* 23, 24 (2007): p. 12436-12444.

[129]   R. Atkin, V.S.J. Craig, E.J. Wanless, S. Biggs, "Mechanism of Cationic Surfactant Adsorption at the Solid–Aqueous Interface," *Advances in Colloid and Interface Science* 103, 3 (2003): p. 219–304.

[130]   P.M. Karlsson, M.W. Anderson, A.E.C. Palmqvist, "Adsorption of Sodium Dodecyl Sulfate and Sodium Dodecyl Phosphate at the Surface of Aluminum Oxide Studied with AFM," *Corrosion Science* 52, 4 (2010): p. 1103-1105.

[131]   Y. Xiong, B. Brown, B. Kinsella, S. Nesic, A. Pailleret, "AFM Studies of the Adhesion Properties of Surfactant Corrosion Inhibitor Films," CORROSION 2013, paper no. 2521 (Orlando, FL: NACE 2013).

[132]   M.A. Gough and G.J. Langley, "Analysis of Oilfield Chemicals by Electrospray-Mass Spectrometry," *Rapid Communications in Mass Spectrometry* 13, 4 (1999): p. 227-236.

[133]   M. Hepel, "Electrode–Solution Interface Studied with Electrochemical Quartz Crystal Nanobalance," in *Interfacial Electrochemistry* 2nd ed. (Springer Science & Business Media, 2010), p. 599.

[134]   R. Bechmann, "Frequency-Temperature-Angle Characteristics of AT-Type Resonators Made of Natural and Synthetic Quartz," *Proceedings of the IRE* 44, 11 (1956): p. 1600-1607.

[135]   Y. Xiong, B. Brown, B. Kinsella, S. Nesic, A. Pailleret, "Atomic Force Microscopy Study of the Adsorption of Surfactant Corrosion Inhibitor Films," *Corrosion* 70, 3 (2013): p. 247-260.

[136]   D.S. Karpovich and G.J. Blanchard, "Direct Measurement of the Adsorption Kinetics of Alkanethiolate Self-Assembled Monolayers on a Microcrystalline Gold Surface," *Langmuir* 10, 9 (1994): p. 3315-3322.

[137]   A.H. Mustafa, B. Ari-Wahjoedi, M.C. Ismail, "Inhibition of CO_2 Corrosion of X52 Steel by Imidazoline-Based Inhibitor in High Pressure CO_2-Water Environment," *Journal of materials engineering and performance* 22, 6 (2012): p. 1748-1755.

[138]   M.J. Rosen and J.T. Kunjappu, *Surfactants and Interfacial Phenomena*, 4th ed. (John Wiley & Sons, 2012), p.125.

[139]   M.L. Free, "Understanding the Effect of Surfactant Aggregation on Corrosion Inhibition of Mild Steel in Acidic Medium," *Corrosion Science* 44, 12 (2002): p. 2865-2870.

[140]   J.W. Gibbs, *The Collected Works of J. Willard Gibbs-Volume 1: Thermodynamics*, (Yale University Press, 1945), p. 244-245.

[141]   J.E. Castle, H.G. Masterson, "The Role of Diffusion in the Oxidation of Mild Steel in High Temperature Aqueous Solutions," *Corrosion Science* 6, 3-4 (1966): p. 93-104.

[142]   J. Robertson, "The Mechanism of High Temperature Aqueous Corrosion of Steel," *Corrosion Science* 29, 11-12 (1989): p. 1275-1291.

[143]   F.H. Sweeton, R.E. Mesmer, C.F. Baes, "Acidity Measurements at Elevated Temperatures. VII. Dissociation of Water," *Journal of Solution Chemistry* 3, 3 (1974): p. 191–214.

[144]   H.H. Perkampus, *UV-VIS Spectroscopy and Its Applications*, 1st ed. (Springer Science & Business Media, 2013), p. 25-27.

[145]   E.B. Nielsen and J.A. Schellman, "The Absorption Spectra of Simple Amides and Peptides," *The Journal of physical chemistry* 71, 7 (1967): p. 2297-2304.

[146]   E. Pretsch, P. Bühlmann, C. Affolter, E. Pretsch, P. Bhuhlmann, C. Affolter, *Structure determination of organic compounds*, (Springer, 2009).

[147]   Z. Chen, X. Guo, Y. Qiu, X. Guo, "Detection of Residual Concentration of Imidazoline Inhibitors in Oilfield Production Water Based on Fluorescence Spectroscopy," *Optics and Spectroscopy* 113, 3 (2012): p. 284-287.

[148]   Beer, "Bestimmung der Absorption des Rothen Lichts in Farbigen Flüssigkeiten, *Annalen der Physik* 162, 5 (1852): p. 78-88.

[149]   A. Horowitz, R. Meller, G.K. Moortgat, "The UV-VIS Absorption Cross Sections of the α-Dicarbonyl Compounds: Pyruvic Acid, Biacetyl and Glyoxal," *Journal of Photochemistry and Photobiology A: Chemistry* 146, 1-2 (2001): p. 19-27.

[150]   H.K. Lichtenthaler and C. Buschmann, "Chlorophylls and carotenoids: Measurement and characterization by UV-VIS spectroscopy," in *Current Protocols in Food Analytical Chemistry* (New York, John Wiley & Sons, 2001), p. F4.3.1-F4.3.8.

[151]   K.J. Scott, "Detection and measurement of carotenoids by UV/VIS spectrophotometry," in *Current Protocols in Food Analytical Chemistry* (New York, John Wiley & Sons, 2001), p. F2.2.1-F2.2.10.

[152]   D.F. Swinehart, "The Beer-Lambert Law," *Journal of Chemical Education* 39, 7 (1962): p. 333.

[153]   J.Y. Yoon, "Piezoelectric Sensors." *Introduction to Biosensors: From Electric Circuits to Immunosensors*, 1st ed. (New York, NY. Springer, 2013), p. 181-198.

[154]   P.C. Hiemenz, R. Rajagopalan, *Principles of Colloid and Surface Chemistry*, 3rd ed. (New York, NY. Marcel Dekker, 1997), p.8.

[155]   K.R. Franklin and B.M. Lowe, "Crystallization of Silica Molecular Sieves from Piperazine—Quaternary Ammonium Bromide—Silica—Water Systems," *Zeolites* 8, 6 (1988): p. 501-507.

[156]   M.L. Occelli, R.A. Innes, S.S. Pollack, J.V. Sanders, "Quaternary Ammonium Cation Effects on the Crystallization of Offretite—Erionite Type Zeolites: Part 1. Synthesis and Catalytic Properties," *Zeolites* 7, 3 (1987): p. 265-271.

[157]   W. Xie, Z. Gao, W.P. Pan, D. Hunter, A. Singh, R. Vaia. "Thermal Degradation Chemistry of Alkyl Quaternary Ammonium Montmorillonite," *Chemistry of Materials* 13, 9 (2001): p. 2979-2990.

[158]   O.E. Zhuravlev, V.M. Nikol'skii, L.I. Voronchikhina, "Thermal Stability of Quaternary Ammonium Hexafluorophosphates and Halides," *Russian Journal of Applied Chemistry* 86, 6 (2013): p. 824-830.

[159]   Y.N. Ahn, S.H. Lee, G.S. Lee, H. Kim, "Effect of Alkyl Branches on the Thermal Stability of Quaternary Ammonium Cations in Organic Electrolytes for Electrochemical Double Layer Capacitors," *Physical Chemistry Chemical Physics* 19, 30 (2017): p. 19959-19966.

[160]   F. Bentiss, M. Lagrenee, M. Traisnel, J.C. Hornez, "The Corrosion Inhibition of Mild Steel in Acidic Media by a New Triazole Derivative," *Corrosion Science* 41, 4 (1999): p. 789-803.

[161]   K.C. Emregül, O. Atakol, "Corrosion Inhibition of Mild Steel with Schiff Base Compounds in 1 M HCl," *Materials Chemistry and Physics* 82, 1 (2003): p. 188-193.

[162]   R. Fuchs-Godec, "The Adsorption, CMC Determination and Corrosion Inhibition of Some N-Alkyl Quaternary Ammonium Salts on Carbon Steel Surface in 2 M H_2SO_4," *Colloids and Surfaces A: Physicochemical and Engineering Aspects* 280, 1-3 (2006) p. 130-139.

[163]   J. Zhang, X.L. Gong, H.H. Yu, M. Du, "The Inhibition Mechanism of Imidazoline Phosphate Inhibitor for Q235 Steel in Hydrochloric Acid Medium," *Corrosion Science* 53, 10 (2011): p. 3324-3330.

[164]   X. Zheng, S. Zhang, W. Li, L. Yin, J. He, J. Wu, "Investigation of 1-Butyl-3-Methyl-1H-Benzimidazolium Iodide as Inhibitor for Mild Steel in Sulfuric Acid Solution," *Corrosion Science* 80, (2014): p. 383-392.

[165]   D.M. Dražić, L. Vračar, V.J. Dražić, "The Kinetics of Inhibitor Adsorption on Iron," *Electrochimica Acta* 39, 8-9 (1994): p. 1165-1170.

[166]   M. Knag, J. Sjöblom, G. Øye, E. Gulbrandsen, "A Quartz Crystal Microbalance Study of the Adsorption of Quaternary Ammonium Derivates on Iron and Cementite," *Colloids and Surfaces A: Physicochemical and Engineering Aspects* 250, 1-3 (2004) p. 269-278.

[167]   H.J. Pracht, J.P. Nirschl, "Process for Making Imidazolinium Salts, Fabric Conditioning Compositions and Methods," U.S. Patent 4127489A, 1978.

[168]   K.J. Crowley, R.T. Forbes, P. York, D.C. Apperley, H. Nyqvist, O. Camber, "Characterization of Oleic Acid and Propranolol Oleate Mesomorphism Using 13C Solid-State Nuclear Magnetic Resonance Spectroscopy (SSNMR)," *Journal of Pharmaceutical Sciences* 89, 10 (2000): p. 1286-1295.

APPENDIX A: FITTING OF ADSORPTION BEHAVIOR BY DIFFERENT
ADSORPTION ISOTHERMS

Introduction

In Chapter 4, the adsorption behavior of the imidazoline-type inhibitor was

simulated with Langmuir adsorption model to obtain deeper kinetic information about the

adsorption behavior. However, there are many adsorption models other than the

Langmuir model, as indicated in Table 7. Although the QCM measurements seem to

follow the Langmuir adsorption model kinetics (see Table 8), it is also possible that other

models might fit as well. Therefore, in this section, other adsorption models are

introduced and fitted with the results obtained with QCM to further validate their use.

Fitting Procedure and Discussion

Langmuir Adsorption Model

The Langmuir adsorption model is one of the most extensively used adsorption

model. The adsorption and corrosion inhibition kinetics of many inhibitors agree well

with this model [29,71,160–164]. When an inhibitor's kinetics follows the Langmuir

adsorption model, it requires that the adsorption of those inhibitors also involves only an

elementary reversible reaction. Therefore, important information of the adsorption, such

as ΔG°_{ads}, can be obtained.

The fitting of Langmuir isotherm can be done using kinetics or thermodynamics

data. Kinetically, the relationship between coverage (θ) and time t can be fitted with

Equation (32). One example of the fitting is given in Figure 79. The good agreement

between the experimental results and the theoretical Langmuir kinetic model (R^2=0.99)

suggests that the mechanism of adsorption of the imidazoline-type inhibitor agrees well

with the assumptions made in the Langmuir model. In addition, the fitting validity can be

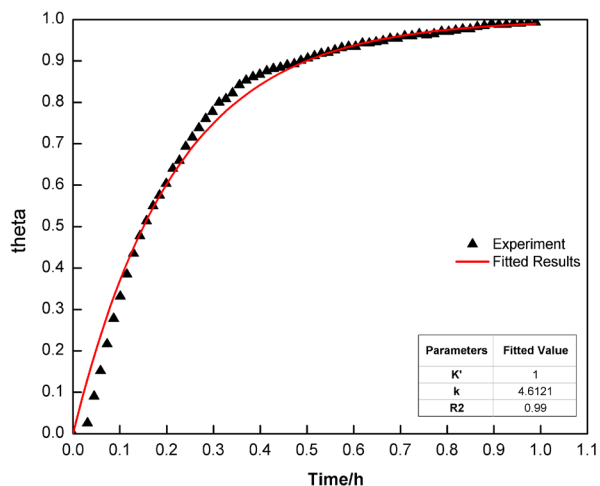represented by the R^2 coefficient, shown in Table 8.

Figure 79. Kinetic fitting of Langmuir isotherm kinetics (25°C, 44ppm imidazoline-type inhibitor.)

In addition, the Langmuir adsorption isotherm can be fitted with thermodynamical

data. The equilibrium form of Langmuir adsorption can be found in Equation (35). The

adsorption of inhibitor should follow the Langmuir adsorption model if the relation

between $\theta/(1-\theta)$ and c (inhibitor concentration) is linear. The relation between the $\theta/(1-\theta)$ and c at 25°C is depicted in Figure 80 for the imidazoline-type inhibitor. The good

linearity, especially at 50°C, again suggests that the adsorption of this inhibitor follows
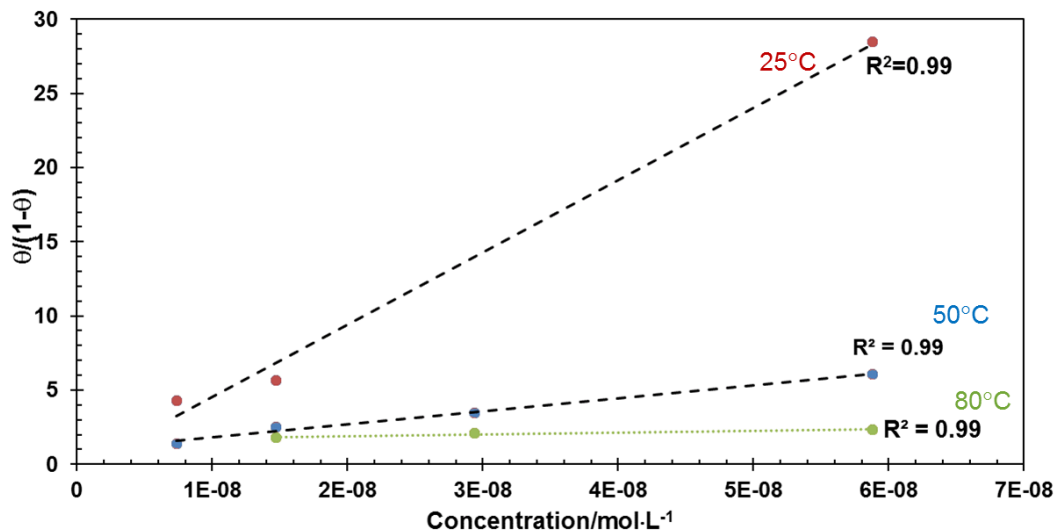
the Langmuir adsorption model.

Figure 80. Thermodynamic fitting of the Langmuir adsorption model.

Temkin Adsorption Model and Its Fitting

The Temkin isotherm and its fitting are discussed in this section. The assumption of the Temkin isotherm is that the surface is heterogeneous and there is no molecular interactions[63]. The kinetic form of the Temkin isotherms can be expressed as:

$$\theta = (1/\beta f)\ln(\beta f k_a c) + (1/\beta f)lnt \qquad (54)$$

Where, f is the heterogeneity factor and β is the transfer coefficient for the adsorption process, which relates to the adsorbent-adsorbate interactions. This equation shows that there should be a linear dependence between θ and $\ln(t)$ if the adsorption mechanism follows the Temkin adsorption model. The θ and $\ln(t)$ data obtained at 25°C in the presence of 44ppm imidazoline-type inhibitor are plotted in Figure 81. The linear dependence between θ and $\ln(t)$ is not as good as for the Langmuir isotherm ($R^2 < 0.96$). In

addition, Equation (54) suggests that the coverage/mass adsorbed should continuously increase with time. However, this is not the case with the inhibitor tested in this study.
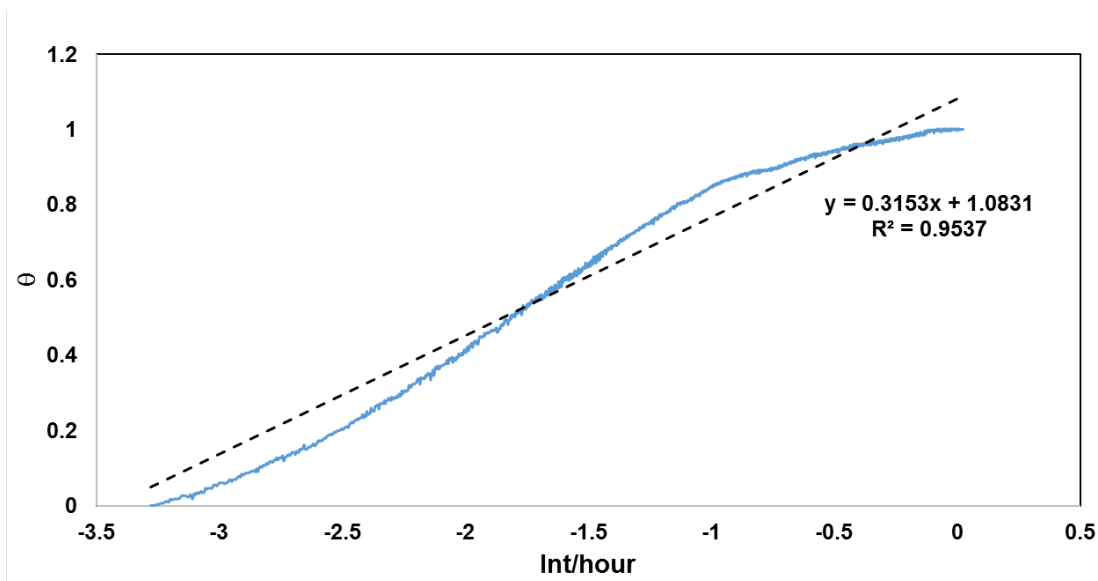

Figure 81. Comparison between ln(t) and θ (25°C, 44ppm imidazoline-type inhibitor)

Thermodynamically, the Temkin isotherm takes the form of the following equation.

$$\theta = A + (1/f)\ln(c) \qquad (55)$$

Where, A is a constant. The relationship between θ and ln(c) is plotted in Figure 82 to verify whether the adsorption of the inhibitor takes the form of Temkin adsorption. The linearity is relatively poor compared to fitting with Langmuir adsorption model. Therefore, it can be concluded that the adsorption of the imidazoline-type inhibitor does not follow the Temkin isotherm.
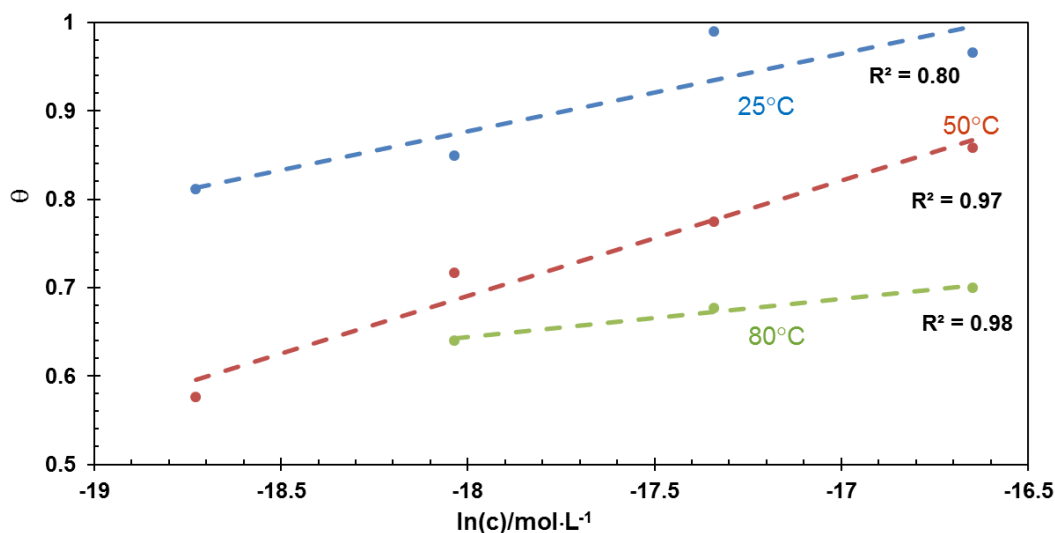
Figure 82. θ vs. ln(c) of the imidazoline-type inhibitor at different temperatures

Frumkin Adsorption Model and Its Fitting

The Frumkin adsorption model is comparatively more complex. In this model, the adsorption of inhibitor is considered via a water molecules displacement process[59,65,165]:

$$inhibitor_{bulk} + n(H_2O)_{ads} \leftrightarrow Inhibitor_{ads} + n(H_2O)_{bulk} \qquad (56)$$

Where, the 'bulk' and 'ads' subscripts represent are the species in bulk and in the adsorbed state, n is the number of water molecules displaced. For example, the Langmuir adsorption is the simplest isotherm with n=1, which means that one inhibitor molecule replaces one water molecule. For other adsorbates, n could take different values. In addition, interactions between the adsorbed inhibitors are also considered. In conclusion, the kinetic Frumkin adsorption isotherm can be represented as:

$$d\theta/dt = k_a n(1 - \theta)^n c \, exp(\lambda\theta) - k_d \theta \, exp(-\lambda\theta) \qquad (57)$$

where, λ is a parameter that relates to the interactions between the adsorbed inhibitors.

There is no analytical solution for this equation and the fitting exercise is not

straightforward. However, the validity of this equation can be relatively easily verified by

using its thermodynamic form, which is derived in Equation (57):

$$K_{eq}c = [\frac{\theta}{n(1-\theta)^n}]\exp(-2\lambda\theta) \qquad (58)$$

This equation can be rearranged in a more convenient way to Equation (58):

$$\theta = -\frac{23}{2\lambda}logK_{eq} + \frac{23}{2\lambda}[\log\left(\frac{\theta}{n(1-\theta)^n}\right) - \log c] \qquad (59)$$

θ should be linearly related to $[\log(\theta/n(1-\theta)^n)-\log c]$ if the adsorption of the imidazoline-

type inhibitor follows a Frumkin isotherm. This relation is shown in Figure 83. Here, it is

necessary to assume the 'n' value first and then determine the validity of the fitting. The

linear relationship is most satisfactory when n=1. In this condition, the fitted line is

parallel to the y-axis, which suggests that the λ value should be close to 0. The 0 value of

λ indicates that the interactions between molecules are negligible. Therefore, the Frumkin

isotherm can be simplified again into Equation (35), which is the Langmuir adsorption

model. In conclusion, the adsorption of the imidazoline-type inhibitor is more likely to

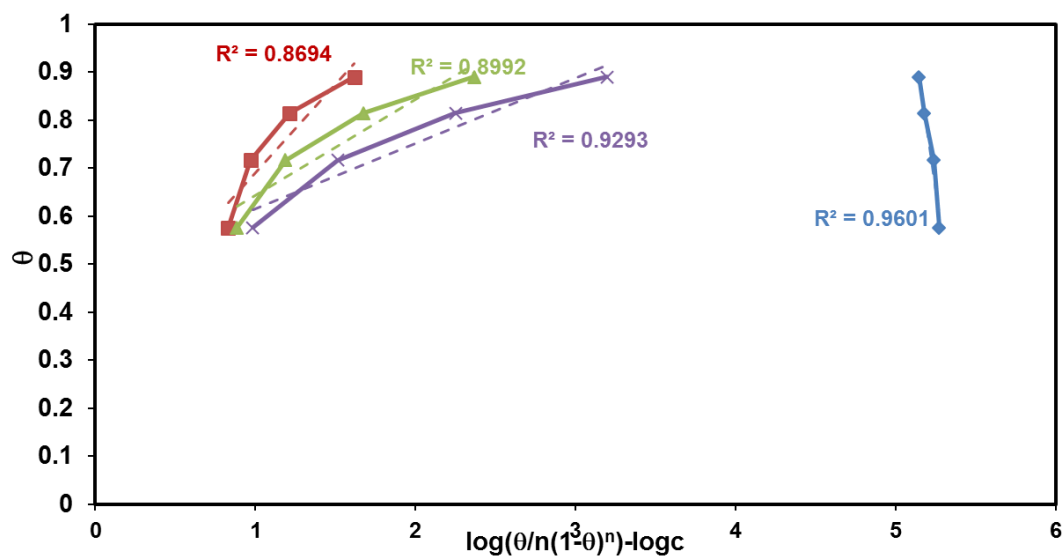follow the Langmuir than the Frumkin adsorption model.

Figure 83. Plots of the thermodynamic form of the Frumkin isotherm with experimentally determined steady state θ for different values of n. (50°C)

APPENDIX B. INVESTIGATION OF THE VALIDITY OF THE SAUERBREY EQUATION FOR ADSORPTION STUDIES

Introduction

The experimental results in this dissertation showed that the adsorption behavior of the imidazoline and the quat-type inhibitors measured with QCM seems to be significantly different. For example, the frequency change caused by the adsorption of imidazoline-type inhibitor was about ten times higher than for the quat-type inhibitor. This means that in terms of mass adsorbed, the adsorption of imidazoline-type inhibitor should be much higher than the quat-type inhibitor. This observation is somehow surprising since the molecular weight of imidazoline-type inhibitor (359 g·mol^{-1}) is close to that of the quat-type inhibitor (352.5 g·mol^{-1}). This discrepancy might have two different reasons. The first one is that the number of imidazoline-type inhibitor layers could be higher than the quat-type inhibitor. However, it was shown that the imidazoline-type inhibitor usually follows Langmuir isotherm, which assumes a monolayer structure. Another possible explanation is that the masses measured by QCM are not genuine 'masses' and that the relationship between change in frequency and mass adsorbed inferred by the Sauerbrey equation does not apply.

The use of the Sauerbrey equation implies two main assumptions:

1. The film must be sufficiently thin. The frequency change caused by the adsorption of molecules should be less than 10% of the resonant frequency of the crystal (f_0). For the inhibitor adsorption, this is no problem because the frequency change measured (10-400Hz) is much smaller than f_0 (5MHz).

2. The adsorbed layer must be rigid. A viscoelastic film might generate additional contribution, other than mass increase, to the changes in the resonant frequency of the crystal. This would lead to the invalid calculation (typically overestimation) of the adsorbed mass.

Therefore, it is necessary to know more information related to the film properties. The conventional QCM technique is not sufficient to determine whether the frequency/mass conversion proposed by Sauerbrey equation is valid. It cannot determine the detailed properties, such as viscosity and elasticity of the inhibitor film. However, the motional resonant resistance (R_m) in the QCM measurements can still provide some elementary information about the inhibitor film properties. Usually, an increase in R_m is an indicator of the adsorption of a viscous film. This is because the formation of soft films and viscous liquids increases the motional losses (energy loss caused by the vibration of QCM in the film) and hence R_m. The elementary representation of a quartz crystal resonator is shown in Figure 84.
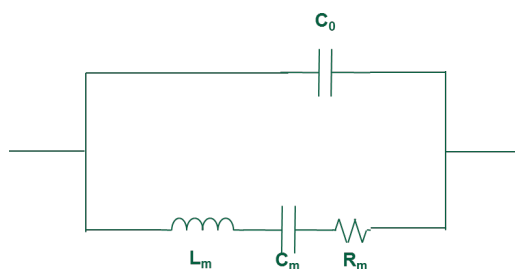

Figure 84. Elementary electrical mode for the quartz crystal resonator. (R_m is the motional resonant resistance; C_m is the capacitor relates to the elasticity of the quartz and the surrounding medium; L_m is the inertial component of the oscillation; C_0 is the parasitic capacitance.)

In this section, the resistance response is analyzed to understand whether the inhibitor film displayed any viscoelasticity properties. In addition, the resistance of the two different inhibitors (imidazoline-type and quat-type) are compared with the frequency change generated by the adsorption of corrosion inhibitor.

Results and Discussion

The change of frequency and the resonant resistance with time at 25°C with the presence of 44ppm imidazoline-type inhibitor is shown in Figure 85. The resistance clearly increased with time, which suggests that the imidazoline-type inhibitor film is indeed a viscoelastic film. This behavior was observed in other conditions as well, establishing that the trends in frequency change and resistance change are related for the imidazoline-type inhibitor. Consequently, Sauerbrey equation should no longer be suitable for calculating the mass change of the imidazoline-type inhibitor adsorption.
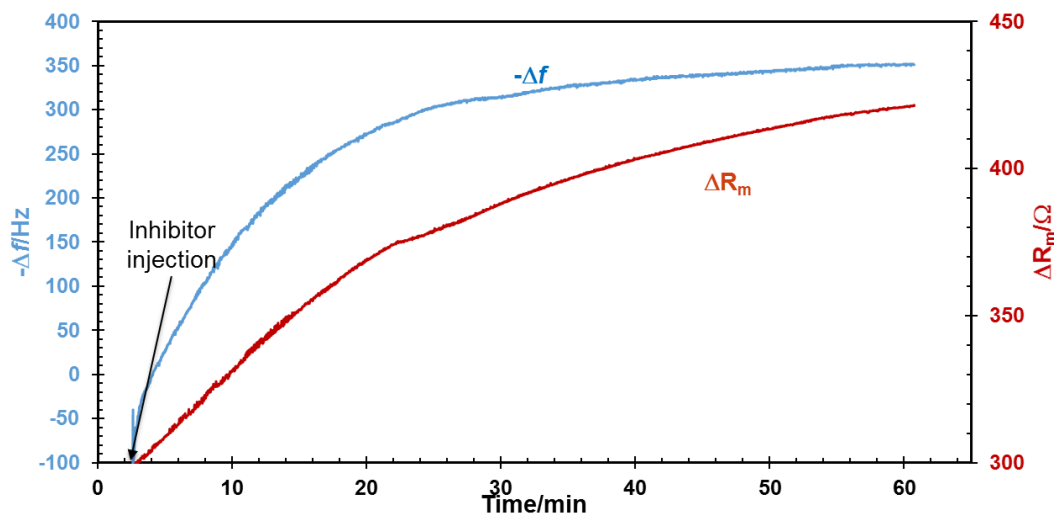
Figure 85. Change of Δf and ΔR_m of 44ppm imidazoline-type inhibitor with time. (25°C, 1 wt.% NaCl)

Considering quat-type inhibitor, ΔR_m did not change significantly. The change of $-\Delta f$ and ΔR_m with the presence of 120ppm quat-type inhibitor at 25°C are shown in Figure 86. The resistance barely changed over the tested period, although Δf decreased by about 25Hz. In other cases (not shown here), only a small variation of ΔR_m were measured, always lower than 0.5Ω. This behavior corresponds to the development of a rigid film, inferring that Sauerbrey equation should still be valid for the quat-type inhibitor. However, it was already noticed that the repeatability of the QCM measurements was poor, suggesting a different set of issues. Clearly, more effort is required for understanding of the quat-type inhibitor adsorption.
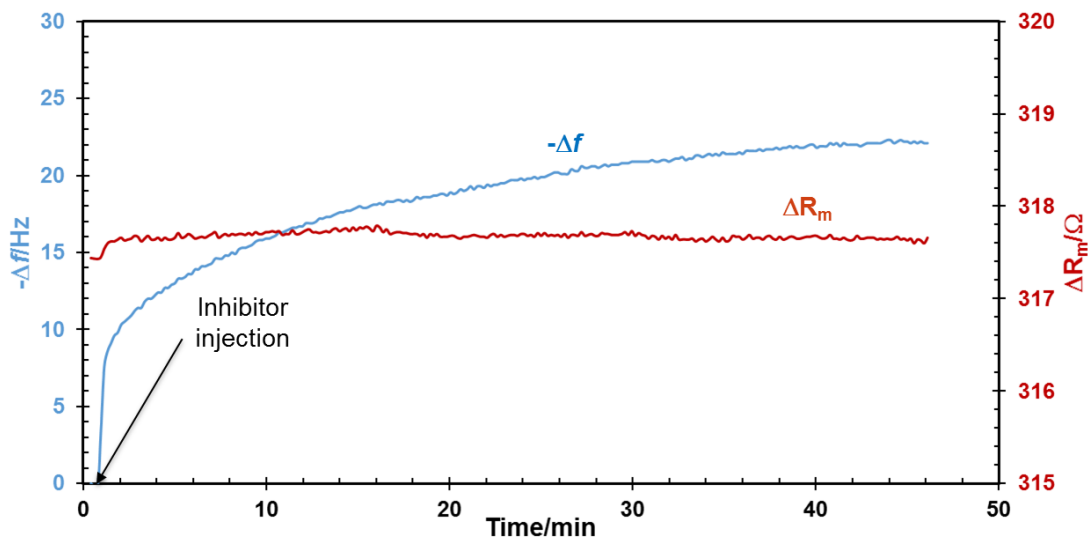
Figure 86. Change of Δf and ΔR_m of the 120 ppm quat-type inhibitor with time. (25°C, 1 wt.% NaCl)

In summary, the imidazoline inhibitor film is likely a viscoelastic film and the Sauerbrey equation cannot be applied in this case. A QCM-D (dissipation), which incorporates with dissipation measurements [127,166], would be required to understand the more in-depth information related to film properties. However, the test setup used in this study does not include the dissipation option and therefore does not appear to be suitable for accurate determination of adsorbed masses.

APPENDIX C. ATTEMPTS TO ATTAIN REPEATABILITY IN THE STUDY OF THE ADSORPTION OF THE QUAT-TYPE INHIBITOR.

Chapter 7 presented the investigation of the adsorption behavior of the quat-type inhibitor using QCM measurements. This study was hindered by inconsistency and lack of repeatability in the measurements. This created a significant obstacle in understanding the adsorptive behavior of the quat-type inhibitor. Many efforts toward achieving repeatable results were made, however unsuccessful. In this section, these efforts are described in more details.

Initial efforts were placed in ensuring that the baseline measurements (without inhibitor) were repeatable. The baseline should not likely change considerably if the chemical and physical properties of the solution do not change. The baseline frequency of the oscillator ($\Delta f_{baseline}$) is governed by the property of the solution, as indicated in Equation (51). The frequency should not easily shift as long as the testing environment is not altered.

Frequency change without any inhibitor was measured for 24 hours to confirm the stability of the baseline. The results are shown in Figure 87, confirming very little change in resonant frequency. Although there were small fluctuations (probably due to the slight temperature change in the environment), they were limited to less than 5Hz in 24 hours. This fluctuation is relatively small compared to the frequency change generated by the adsorption of inhibitor and should not affect the repeatability of the tests. In addition, the OCP of the crystal was also recorded during the test. The OCP change is around

4mV/hour and not as stable as $\Delta f_{baseline}$. Therefore, the fluctuation in the OCP might be responsible for the lack of repeatability.
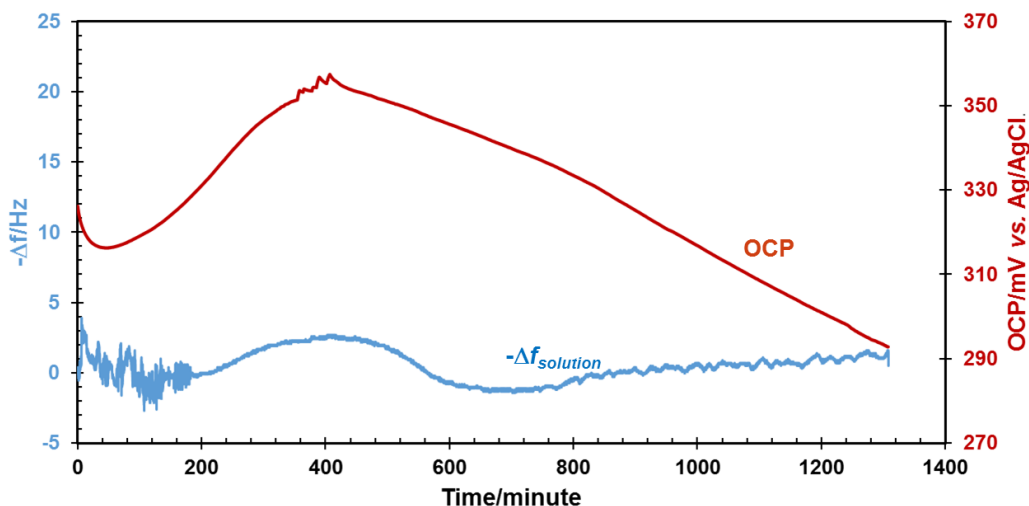

Figure 87. Stability of the solution baseline and the OCP of the quartz crystal; (25°C, 1 wt.% NaCl; Gold-coated crystal, 5MHz.)

Consequently, the adsorption behavior was investigated with a fixed potential at +380mV *vs.* saturated Ag/AgCl electrode to investigate if the fixed potential could improve the repeatability. The results are shown in Figure 88. Although the fixed potential seemed to improve the repeatability with the presence of 130ppm quat-type inhibitor, there was still a large inconsistency in the repeated cases with the presence of 65ppm and 260ppm corrosion inhibitor. Consequently, it was determined that applying a fixed potential did not significantly improve the repeatability. More efforts were made on using different type of crystals (polished *vs.* etched), modifying the crystal cleaning procedure (using strong acid to clean the surface) (not shown here). However, neither of

these efforts seem to improve the repeatability. The main causes for the variability in the measurement remain elusive.
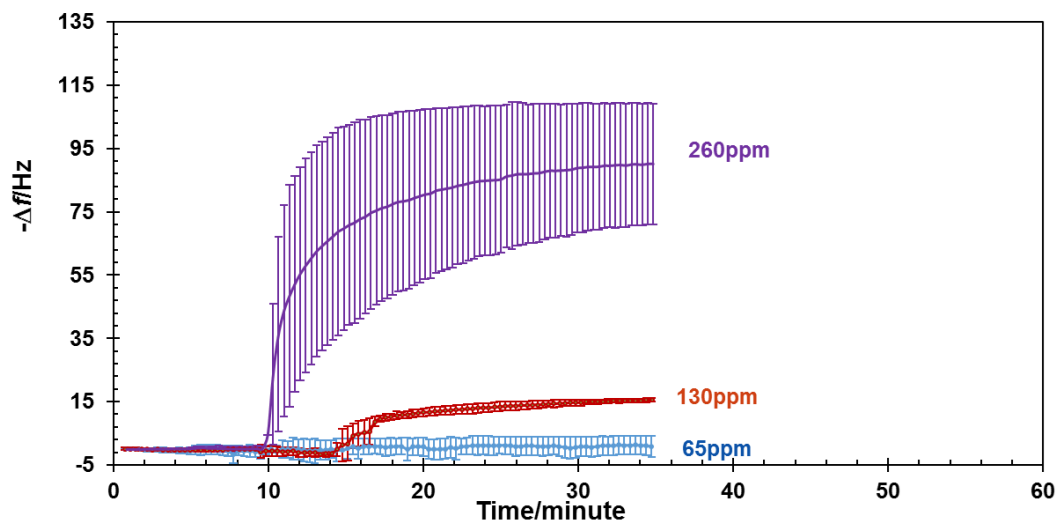

Figure 88. Repeatability of the QCM measurement with fixed applied potential of +380mV vs. Ag/AgCl eletrode. (25°C, 1wt. % NaCl; Gold-coated crystal, 5MHz, with quat-type inhibitor)

APPENDIX D. SPECTROSCOPIC ANALYSIS OF THE IMIDAZOLINE-TYPE
INHIBITOR

Introduction

In the earlier experiments, the imidazoline-type inhibitor was found to be unstable

at elevated temperatures (120°C and 150°C) and to degrade into its amide precursor. The

concentration loss was found to be around 40%-50% and some black oily residues were

observed on the equipment surfaces. Further FTIR analysis showed that the residues were

likely the amide precursor. However, the degradation of the imidazoline inhibitor might

not be the only source of the amide. As the precursor of imidazoline, amide could be

already in the package as a minor product in the synthetic reactions. The general

procedure of imidazoline synthesis reaction can be found in Figure 89 [102]. The

synthesis starts from a first dehydration reaction (see Figure 89 (a)) between fatty acid

(only oleic acid is shown here as a representative). Diethylenetriamine and the amide

precursor is then formed. After this step, the amide can go through another dehydration

reaction by itself (see Figure 89 (b) and can form into imidazoline. As a result of the

limitations in conversion rate and purification, it is almost impossible to remove the

amide completely during the synthesis. Moreover, an additional amide side product might

be contained in the package. In order to ensure a higher conversion rate of imidazoline,

more fatty acid are usually introduced at the beginning. The additional fatty acid can

react with the imidazoline through another dehydration reaction and form into an amide

product (alkoxylized imidazoline) [167] (see Figure 89 (c)). These amides could be

present in the initial inhibitor package. In addition, it is possible that there are still some

unreacted fatty acids and diethylenetriamine left in the package. Therefore, a series of

spectroscopic analyses were used to identify which species were present in the original package.
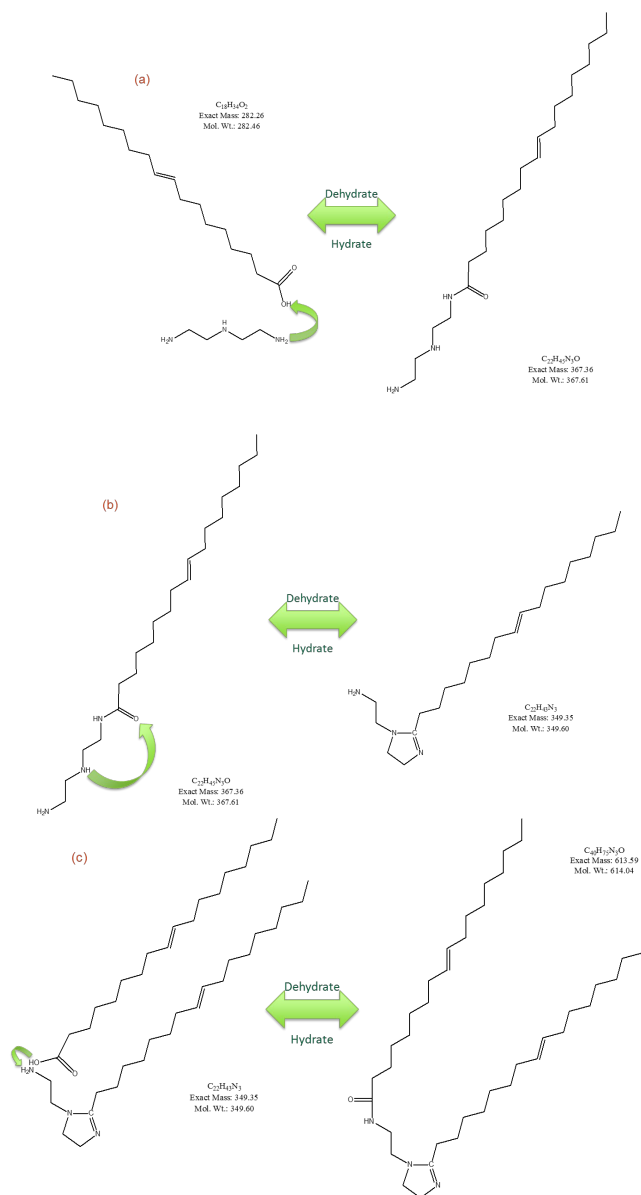

Figure 89. The synthesis reaction of a commercial imidazoline inhibitor.

Results and Discussion

According to the Chapter 6, the imidazoline peaks can be clearly observed in the UV-vis spectra. However, the peaks representing the amide peaks were not found. This does not mean that there was no amide in the inhibitor package because amide is not as readily soluble in water as the imidazoline. As a result, the UV-vis spectroscopy might not be able to capture the presence of the amides in the aqueous phase.

The FTIR spectra of the inhibitor package is shown in Figure 90. It indicates the presence of both amide and imidazoline. The peak 1 and 3 are the st mode of the C=N bond and the st sy mode of the N-C=O bond [146], both only exist in amides. Additionally, peak 2 at $1610cm^{-2}$ stands for the st mode of the C=N bond, which only can be found in imidazoline ring. Clearly, the FTIR analysis again proved the presence of amide and imidazoline in the inhibitor. However, it can still not distinguish what amide it is (precursor amide vs. alkoxylized imidazoline).
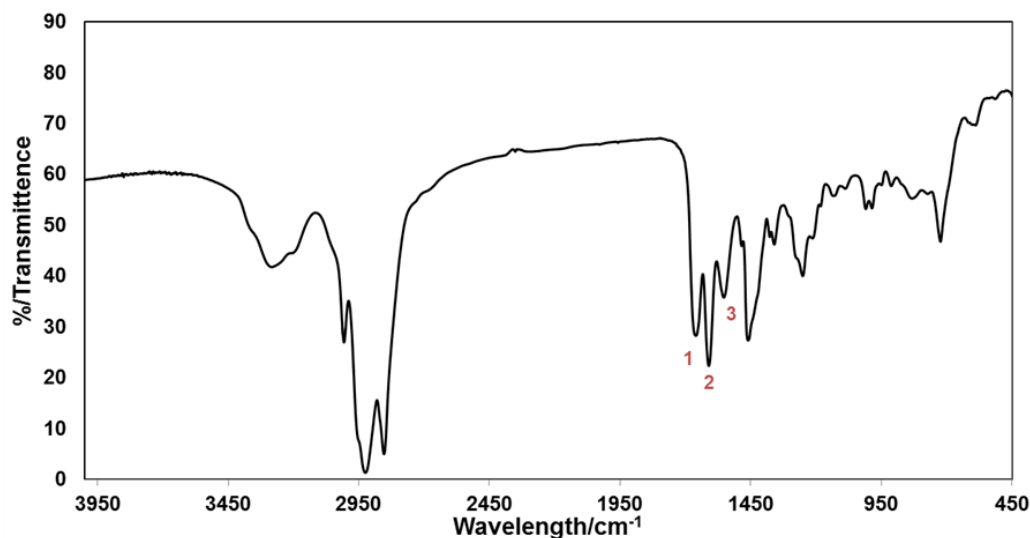
Figure 90. FTIR spectra of the imidazoline-type inhibitor

^{13}C NMR spectroscopy was also performed and the spectra is shown in Figure 91. The peaks in the 160-180ppm and 120-140ppm are representative of amide and imidazoline, respectively [102]. The peaks at around 54ppm and 42ppm agrees well with the standard diethylenetriamine ^{13}C NMR, which means that there are still some diethylenetriamine in the inhibitor. In addition, the peaks in the 20-40ppm range are likely the peaks of different carbons in the fatty acid [168]. However, one important peak is missing in the spectra. The peak of the carbon in the hydroxy acid of the oleic acid is at around 182ppm [168], which is not observed in the spectra. Therefore, it can be seen that there should be some unreacted diethylenetraimine but no unreacted oleic acid left in the inhibitor.
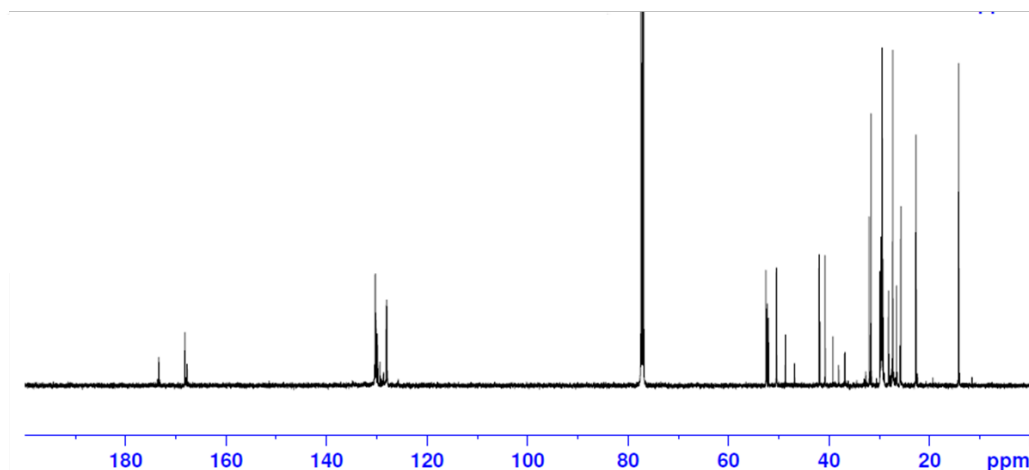
Figure 91. ^{13}C NMR spectra of the imidazoline-type inhibitor

ppm is the unit of chemical shift and independent of the spectrometer frequency.

The mass spectroscopy was also performed and the result is shown in Figure 92. In Figure 92 (a), there are many peaks in the 0-300m/z range. However, by comparing the molecular weight of possible ingredients (diethylenetraimine and fatty acids), no match was found. Therefore, these peaks are likely the by-products that created during the electron bombarding of the inhibitor before mass spectroscopy measurements. To better investigate the molecules of interest, the spectra ranging from 300-650m/z is shown in Figure 92 (b). The spectral analysis suggests that the amide might be mostly the alkoxylized imidazoline. In the spectra, the peaks around 348m/z agrees well with the molecular weight of the imidazoline inhibitor. The peak around 610m/z agrees well with the molecular weight of the alkoxylized imidazoline. However, there is no significant peaks at 367m/z (molecular weight of the amide precursor), which suggests that the amide precursor was probably not a major ingredient in the inhibitor.

In conclusion, the major ingredient of the inhibitor is likely the imidazoline-type inhibitor. Diethylenetraimine, one of the initial reactants, was also found in the spectroscopic analysis. However, no sign of oleic acids, another reactant, was noticed. In addition, there is small amount of amide left in the inhibitor, yet mostly in the form of alkoxylized imidazoline instead of amide precursor.
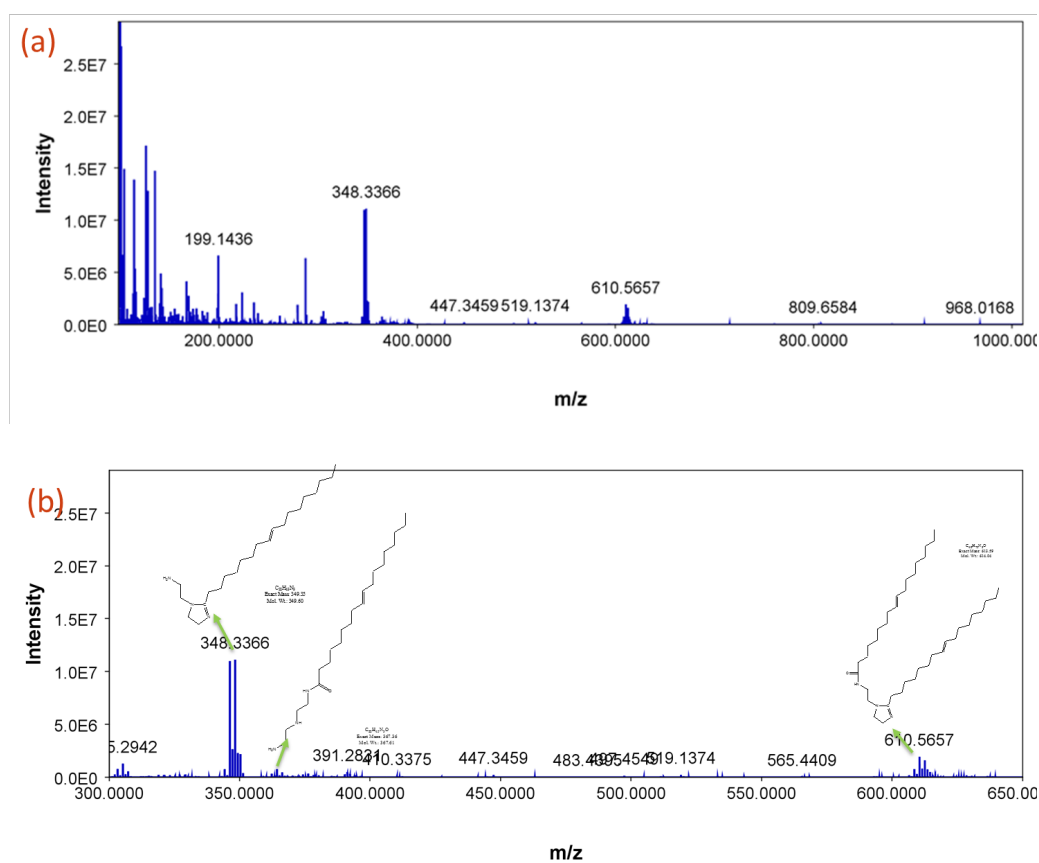

Figure 92. Mass spectra of the imidazoline-type inhibitor. (a) Spectra ranging from 0-1000m/z; (b) spectra ranging from 300-650m/z

Thesis and Dissertation Services